Modeling of Electron Transpiration Cooling for Leading Edges of Hypersonic Vehicles

by

Kyle Matthew Hanquist

A dissertation submitted in partial fulfillment
of the requirements for the degree of
Doctor of Philosophy
(Aerospace Engineering)
in The University of Michigan
2017

Doctoral Committee:

Professor Iain D. Boyd, Chair
Professor Mark J. Kushner
Professor Kenneth G. Powell
Professor Philip L. Roe

Traveling through hyperspace ain't like dusting crops, boy!
Without precise calculations we could fly right through a star,
and that'd end your trip real quick, wouldn't it.

HAN SOLO

Kyle M. Hanquist

hanquist@umich.edu

ORCID iD: 0000-0002-3817-8942

To my parents

ACKNOWLEDGEMENTS

This dissertation represents much more than my own personal efforts over the last several years.

First and foremost, I would like to thank my advisor, Professor Iain Boyd, for all the support and guidance throughout my doctoral study. Your guidance was instrumental to the success of this work and your mentoring was invaluable to my personal and professional growth.

I would also like to thank the rest of my doctoral committee: Professor Mark Kushner, Professor Kenneth Powell, and Professor Philip Roe. I am grateful for all of the useful feedback on my research as well as guidance both in the classroom and professionally. Thank you all for taking time out of your busy schedules to serve on my committee.

To my office and lab mates both present and past, thank you for your help and friendship. A special thank you is due to Hicham Alkandry for his mentorship and laying the groundwork for the project that became the focus of this thesis. The Aerospace Engineering and College of Engineering staff also deserves huge thanks. Denise Phelps has been a constant source of support, guidance, and conversation during my time at Michigan.

I am very appreciative of the opportunity to spend a summer during my doctoral studies at NASA Ames Research Center. There are numerous mentors that made the experience both beneficial to my growth as a researcher, and a memorable adventure including Ioana Cozmuta, Nagi Mansour, Ryan McDaniel, Daniel Rasky, Mark

Newfield, and Kathleen Starmer.

I am grateful for my undergraduate experience at the University of Nebraska. The experience motivated me to continue my education and prepared me for my graduate studies. I would especially like to thank Professors Kevin Cole, George Gogos, and Wieslaw Szydlowski for their teaching and mentorship.

Between the friends that I have made in graduate school and those who have been by my side even longer, I am truly blessed and thankful. To list every name would take many pages, but I am sincerely grateful for each and every one of you.

Finally, I would like to thank my family. It has been a lifelong dream to attend the University of Michigan and that is largely due to my family. From my grandfather and great-grandfather both receiving their doctorates here [1, 2], to my mother and I rooting for the Wolverines in Cornhusker country, this is truly a dream come true. To my father, seeing how hard you worked on the farm taught me what hard work is and that work ethic is what helped me get to this stage. To my mother, you taught me how to dream and always encouraged me to follow them. Thank you both and the rest of my family for all of your love and support.

Funding for this work was provided by Lockheed Martin Corporation and the U.S. Department of Energy Office of Science, Fusion Energy Sciences Program. This research was supported in part through computational resources and services provided by Advanced Research Computing at the University of Michigan.

TABLE OF CONTENTS

LIST OF FIGURES

Figure

LIST OF APPENDICES

Appendix

LIST OF ABBREVIATIONS

AFRL Air Force Research Laboratory

ARV Ascent and Re-Entry Vehicle

CAV Cruise and Acceleration Vehicle

CEA Chemical Equilibrium with Applications

CFD Computational Fluid Dynamics

DARPA Defense Advanced Research Projects Agency

DK Direct Kinetic

DSMC Direct Simulation Monte Carlo

ETC Electron Transpiration Cooling

HTV Hypersonic Technology Vehicle

NASA National Aeronautics and Space Administration

RV-NW Non-Winged Re-Entry Vehicle

RV-W Winged Re-Entry Vehicle

SSTO Single Stage to Orbit

TCS Thermal Control System

TPS Thermal Protection System

UHTC Ultra High Temperature Composite

VDF Velocity Distribution Function

LIST OF SYMBOLS

a	Acceleration
A	Variable used for sheath relations
A_R	Richardson constant, 1.20×10^6 A/m^2/K^2
$\mathbf{B}$	Magnetic field
c	Charge number
C	Acoustic speed
C_p	Constant pressure specific heat
$\mathbf{D}$	Drag
D_s	Diffusion coefficient of species s
e	Elementary charge, 1.60×10^{-19} C
$\tilde{e}$	Internal specific energy of the material
e_{ve}	Vibrational-electron-electronic energy per unit mass
E	Energy per unit volume
$\mathbf{E}$	Electric field
f	Velocity distribution function
F	Variable used for sheath relations
$\mathbf{F}$	Flux
g_j	Degeneracy factor of electronic energy level j
G	Variable used for sheath relations
h	Enthalpy
H	Variable used for sheath relations

$\hbar$	Planck constant, 6.63×10^{-34} m^2 kg/s
$\bar{\bar{I}}$	Identity matrix
I_{ioniz}	Ionization potential
$\vec{j}$	Electric current density
J_e	Emission current density
J_f	Flowfield charged species current density
$\mathbf{J}$	Diffusion flux
k_B	Boltzmann constant, 1.38×10^{-23} J/K
k_b	Backward reaction rate coefficient
k_f	Forward reaction rate coefficient
K_e	Equilibrium constant
K_s	Mobility of species s
Kn	Knudsen number
L	Characteristic length
m	Mass
M	Mach number
M_s	Molar mass of species s
n	Number density
$\hat{n}_i$	Normal vector
N_{Av}	Avogadro constant, 6.02×10^{23} mol^{-1}
p	Pressure
P_s	Polarizability of species s
q	Heat transfer rate
Q	Collision cross section of gas
$\mathbf{Q}$	Conserved variables
Q_{int}	Internal energy partition function
R_n	Leading edge radius

R_u	Universal gas constant, 8.31 J/K/mol
Re	Reynold's number
S	Source term
t	Time
T	Temperature
u	Velocity
V_{th}	Theshold velocity
$\dot{w}_s$	Production rate of species s
$\dot{w}_{ve}$	Transfer of energy to/from the vibrational-electronic-electron mode
W_F	Material work function
Y	Mass fraction
α	Level of ionization
β	Constant used for sheath relations
γ	Ratio of emitted electron temperature to electron temperature at the sheath edge
$\tilde{\gamma}$	Ratio of specific heats
Γ	Ratio of emission to flowfield current densities
δ_c	Kinetic collisional diameter
ϵ	Material emissivity
ϵ_0	Vacuum permittivity, 8.85×10^{-12} F/m
θ_i	Characteristic temperature for ionization
θ_j	Characteristic temperature for electronic energy level j
ι	Ratio of ETC to radiative cooling
κ	Thermal conductivity
λ	Mean free path
λ_D	Debye length
μ	Viscosity
μ_0	Vacuum permeability, $4\pi \times 10^{-7}$ T·m/A

$\mu_{s,j}$ Reduced mass of species s and j

ν_m Momentum transfer collision frequency

ρ Density

σ Electrical conductivity

σ_{sb} Stefan-Boltzmann constant, 5.67×10^{-8} W/m^2/K^4

τ Sheath collisionality

$\bar{\bar{\tau}}$ Viscous stress tensor

ϕ Electric potential

Φ Normalized sheath potential

χ Mach number of ions entering plasma sheath

ω_e Gyro frequency of electrons

Ω Control volume

Ω_e Hall parameter

Subscript

0 Quasineutral flowfield

c Cooling

cond Conductive

conv Convective

$diff$ Mass diffusion

d Drift

e Electron

ETC Electron transpiration cooling

f Flowfield

h Heavy particle

i Ion

in In-depth surface conduction

n Normal

rad Radiative

s Species s

sat Saturation

sc Space-charge

t Total

tr Translational

vc Virtual cathode

ve Vibrational-electron-electronic

w Wall

∞ Freestream

Superscript

x Designates shape type of leading edge

(two-dimensional body = 0, axisymmetric body = 1)

ABSTRACT

The development of aeronautics has been largely driven by the passion to fly faster. From the flight of the Wright Flyer that flew 48 km/hr to the recent advances in hypersonic flight, most notably NASA's X-43A that flew at over 3 km/s, the velocity of flight has steadily increased. However, as these hypersonic speeds are reached and increased, contradicting aerothermodynamic design requirements present themselves. For example, a hypersonic cruise vehicle requires sharp leading edges to decrease the drag in order to maximize the range. However, the aerodynamic performance gains obtained by having a sharp leading edge come at the cost of very high, localized heating rates. There is currently no ideal way to manage these heating loads for sustained hypersonic flight, especially as flight velocities continue to increase.

An approach that has been recently proposed involves using thermo-electric materials on these sharp leading edges to manage the heating loads. When exposed to high convective heating rates, these materials emit a current of electrons that leads to a cooling effect of the surface of the vehicle called electron transpiration cooling (ETC). This dissertation focuses on developing a modeling approach to investigate this phenomenon. The research includes developing and implementing an approach for ETC into a computational fluid dynamics code for simulation of hypersonic flow that accounts for electron emission from the surface. Models for space-charge-limited emission are also developed and implemented in order to accurately determine the level of emission from the surface. This work involves developing analytic models and

assessing them using a direct-kinetic plasma sheath solver. Electric field effects are also implemented in the modeling approach, which accounts for forced diffusion and Joule heating. Finally, the modeling approach is coupled to a material response code in order to model the heat transfer into the material surface.

Using this modeling approach, ETC is investigated as a viable technology for a wide range of hypersonic operating conditions. This includes altitudes between 30 and 60 km, freestream velocities between 4 and 8 km/s, and leading edge radii between 1 mm and 10 cm. The results presented in this study show that ETC can reduce the leading edge temperature significantly for certain conditions, most notably from 3120 to 1660 K for Mach 26 flight for a sharp leading edge (1 cm). However, at lower velocities, the cooling effect can be diminished by space-charge limits in the plasma sheath. ETC is shown to be most effective at cooling hotter surfaces (e.g. high freestream velocities and sharp leading edges) and the level of ionization in the flowfield can help the emission overcome space-charge limits. The modeling approach is assessed using experiments from the 1960s where thermionic emission was investigated as a mode of power generation for reentry vehicles. The computational results produce a wide range of emitted current due to the uncertainty in the freestream conditions and material properties, but they still agree well with the experiments. Overall, this work indicates that ETC is a viable method of managing the immense heat loads on sharp leading edges during hypersonic flight for certain conditions and motivates future work in the area both computationally and experimentally.

CHAPTER I

Introduction

1.1 Motivation

1.1.1 High-speed flight

Throughout human history, advances in technologies have been largely driven by the passion for speed. From faster communication (e.g. printing press, telegraph, internet) to faster transportation (e.g. wheel, engine, flight) technologies have been progressed to meet the aspiration to accomplish something faster. The development of aeronautics has been no different, which has been motivated by the passion to fly faster.[1] Figure 1.1 presents some historic flights that impacted the speed of flight. With the first flight of the Wright Flyer reaching a top speed of 48 km/hr in 1903 to Chuck Yeager breaking the sonic barrier in the Bell XS-1 in 1947 to the recent advances in hypersonic flight, most notably NASA's X-43A, which flew Mach 9.68 in 2004, the velocity of flight has steadily increased. This trend is illustrated in Figure 1.2, which shows how flight speeds have increased during the first century of powered flight and how advances in flight technology (i.e. propulsion systems) have been generally associated with increased flight velocities. For the early part of the 20th century, propellers were the primary source of propulsion for flight and a

[1] This passion or aspiration to go faster in aeronautics is often attributed to another goal such as being faster than the opposition.

steady increase of flight velocity can be seen. When the turbine (i.e. jet) engine was introduced to flight four decades after the first flight of the Wright Flyer, the speed of flight continued to increase at a high rate due to this advanced technology. The speed increase of turbine engine powered flight has not continued in recent years, which is not due to inadequacy of technology, but due to other performance objectives (e.g. fuel efficiency, acoustic signature, manufacturing cost) governing design [3]. However, with the introduction of a new propulsion system to flight, the rocket engine, flight speeds have continued to increase surpassing supersonic and reaching hypersonic[2] velocities, although for short durations of time. The pioneer of hypersonic flight was the rocket-powered North American X-15, which flew at 6.7 times the speed of sound (2 km/s)[3] in 1967. Finally, with the development of scramjet technology [4], longer and faster flights have been obtained and sustained hypersonic flight is becoming more of a possibility. This was demonstrated by NASA's X-43A, which flew at Mach 9.68 for 10.5 seconds of powered flight [5], and AFRL's X-51A, which flew near Mach 5 for over 200 seconds [6].

This persistant increase in the *need for speed* is expected to continue into the future, especially with the growth of national and global interest in hypersonic flight (e.g. scramjet propulsion, thermal protection) as an area of focus in their 2015 *NASA Technology Roadmaps* [7]. The United States Air Force also identified hypersonic technologies as being a focus of future development in their 2010 *Technology Horizons* [8] as well as affirmed the importance of hypersonic technology to national security [9]. Other countries are also developing hypersonic flight (e.g. transport) vehicles including China, Russia, Germany, Australia, and the United Kingdom [10]. There has also been a continued interest in developing a single-stage-to-orbit (SSTO) aerospace plane since the Air Force first investigated the idea in the 1960s, NASA and United States Department of Defense in the 1980s, and the National Aerospace Plane pro-

[2]See Section 1.2.1 for definition of hypersonic flight.

[3]Fastest speed ever recorded by a manned, powered aircraft.

(a) *Wright Flyer I*: first successful heavier-than-air powered aircraft (1908). Figure from Smithsonian Institution.

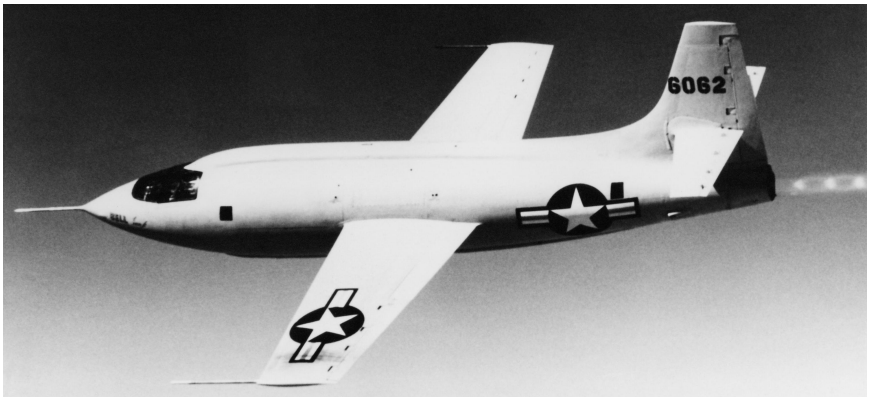

(b) *Bell XS-1*: first manned supersonic flight (1947). Figure from NASA.

(c) *X-43A*: fastest jet-powered unmanned aircraft, which flew at Mach 9.68 (2004). Figure from NASA Illustrations.

Figure 1.1: Select historic flights.

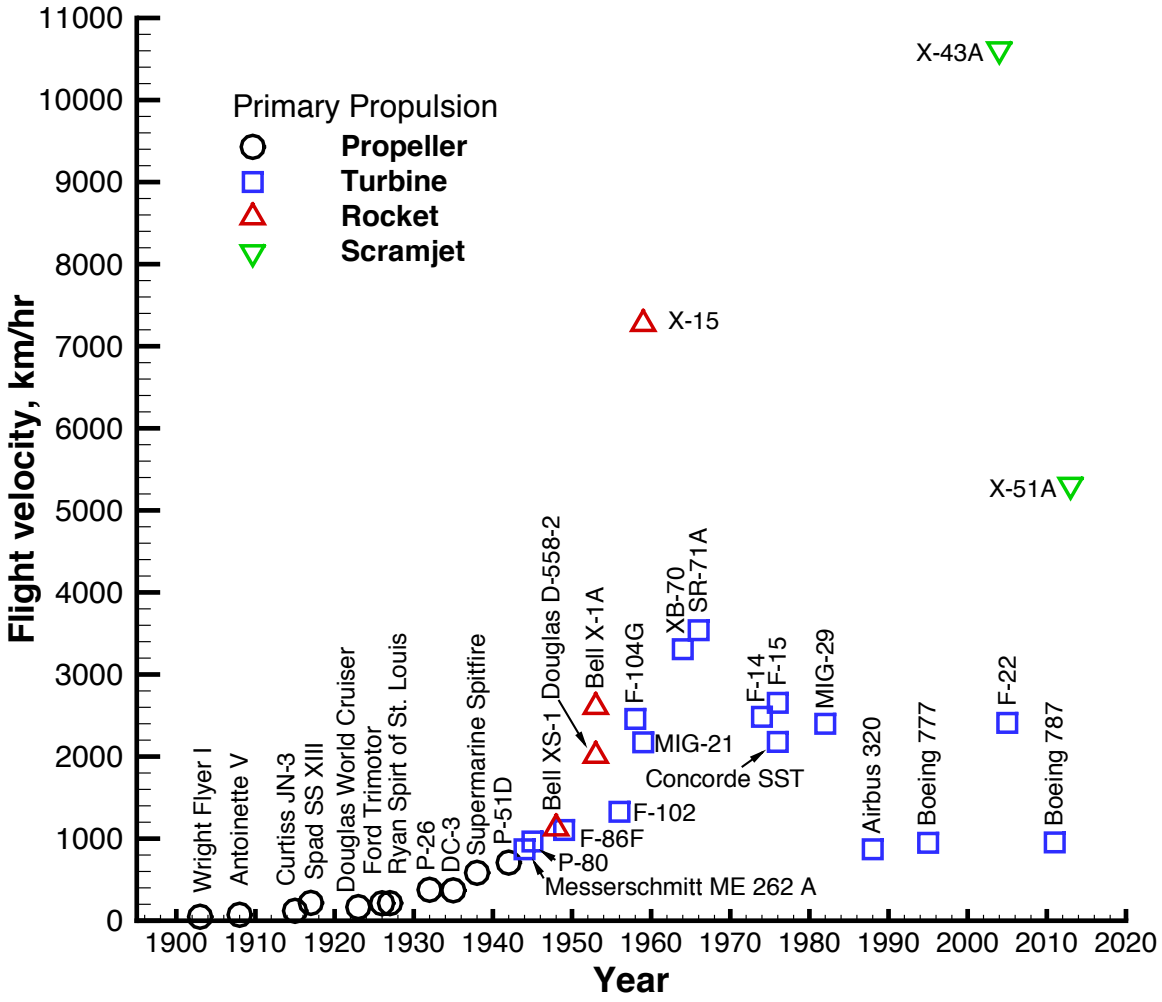

Figure 1.2: Typical flight velocities over the years.

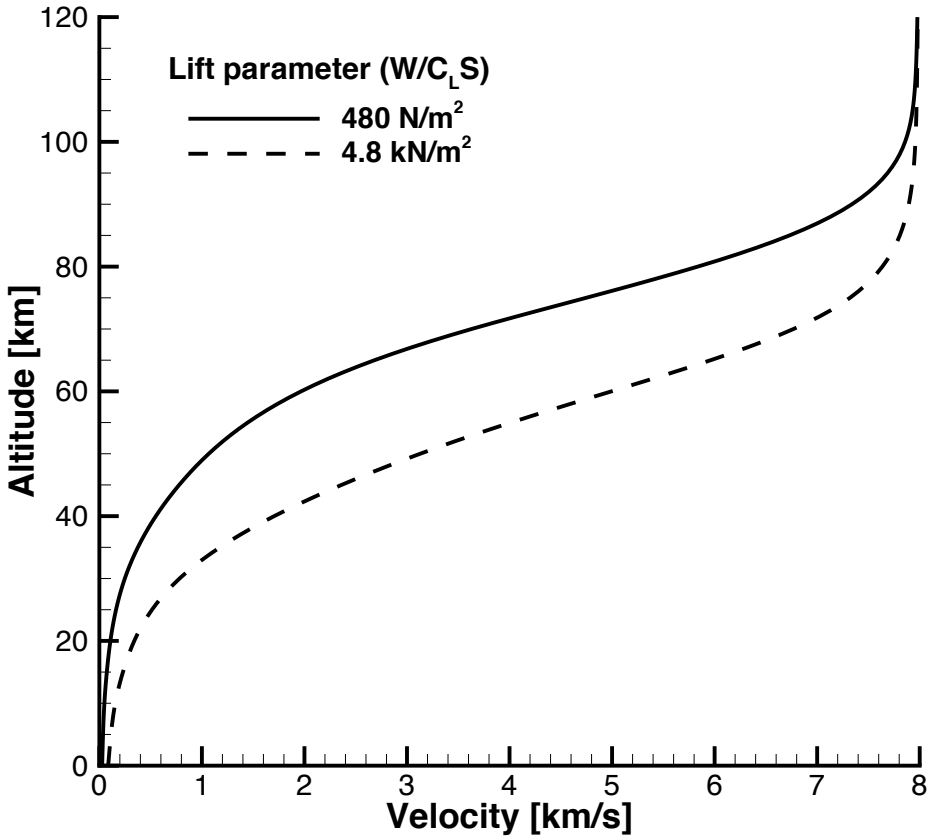

Figure 1.3: Altitude-velocity map to reach orbital velocity for flight-vehicle.

gram in 1990s. The idea behind a SSTO plane is that it would be able to take off, accelerate into Earth's orbit, and even possibly return to Earth all without jettisoning any hardware (e.g. reusable vehicle). More details of this type of vehicle is discussed in Section 1.2.2. Each program was eventually terminated due to the design requirements exceeding the state of the art at the time (e.g. propulsion, aerothermodyanmics) [11]. A complicating factor of SSTO is being able to reach the high orbital velocity needed as illustrated in the altitude-velocity map in Figure 1.3. The altitude-velocity map presents the velocity required by a lifting-entry vehicle to reach orbital velocity, which is approximately 8 km/s.

However, with recent advancements in technologies, the idea of sustained hypersonic flight or even SSTO seems more possible [12, 13]. Flights of the X-43A and the Hypersonic Technology Vehicle 2 (HTV-2), which was a glider developed

by the DARPA Falcon project [14] that reached velocities of near Mach 20, show that the technology needed for sustained hypersonic flight has matured in recent years. However, one of the main challenges remaining to sustained hypersonic flight is aerothermodynamics and managing the high-heat loads inherent to high-speed flight [10, 11, 15, 16]. In order to maximize the range of any flight vehicle, the drag must be minimized, which essentially involves designing a slender body with sharp leading edges for the case of hypersonic flight vehicles. This is shown by a theoretical analysis performed by Lees and Kubota [17], which revealed that drag is proportional to the leading edge radius,

$$\mathbf{D} \propto \rho_\infty u_\infty R_n^{x+1}, \tag{1.1}$$

where x equals zero for a two-dimensional body (i.e. wedge) and x is unity for an axisymmetric body. However, this decrease in radius comes at a cost of increased convective heat transfer as shown by a later theoretical analysis performed by Fay and Riddell [18], which shows that the stagnation point heat transfer is inversely proportional to the square-root of the vehicle leading edge radius,

$$q_{conv} \propto \sqrt{\frac{\rho_\infty}{R_n}} u_\infty^3. \tag{1.2}$$

Given these two contradicting design requirements, the aerothermodynamic design of a slender hypersonic vehicle is complex, especially as the desired speed is increased. Modifications to the leading edge shape (e.g. power-law shapes) can result in some mitigation of the heating loads [19, 20] but high convective heating rates near the leading edge will remain inherent to high-speed flight [21]. There is currently no ideal way to manage these heating loads for sustained hypersonic flight for the slender vehicle shapes required, especially as the velocity approaches orbital, which is discussed further in Section 1.2.2. An alternative approach that has been proposed

recently involves using thermionic materials at the leading edges of hypersonic vehicles [22, 23]. When exposed to high convective heating rates, these materials emit a current of electrons that leads to a transpiration cooling effect of the surface of the vehicle called electron transpiration cooling (ETC). The electrons are emitted through a phenomenon known as thermionic emission that occurs when the thermal energy given to the electrons is greater than the binding potential of the surface material and is discussed further in Section 1.2.3. This thesis focuses on investigating the effect of ETC on leading edges of hypersonic vehicles, specifically from a thermal management standpoint, through extensive modeling development, implementation, and analysis.

1.1.2 Numerical modeling

Since ETC is a recently proposed approach for managing the high convective heating rates inherent to hypersonic flight, there are multiple possible paths to investigating the feasibility of ETC. How ETC will perform during hypersonic flight can be viewed as a "physical truth" (physical phenomenon). In order to obtain this "physical truth," one can use measurements (experiments) or theoretical modeling, in which one approximates a physical system using mathematical description. The process of obtaining the "physical truth" is shown in the schematic in Figure 1.4. In order to truly understand ETC, it must be investigated extensively through experiments, theory, and computer simulation including verification and validation of the approaches used. In terms of hypersonics, it is difficult and resource intensive to recreate the high thermal environments experienced during flight on the ground (e.g. arc-jet and plasmatron testing) and flight tests are costly and time consuming [24]. However, numerical modeling is less expensive, has quick-turnaround, and can provide detailed information and insight [25]. Many of the recent advancements in hypersonic technology have been due to an increased ability to model the aerothermodynamic environments of interest using physical models, numerical algorithms, and

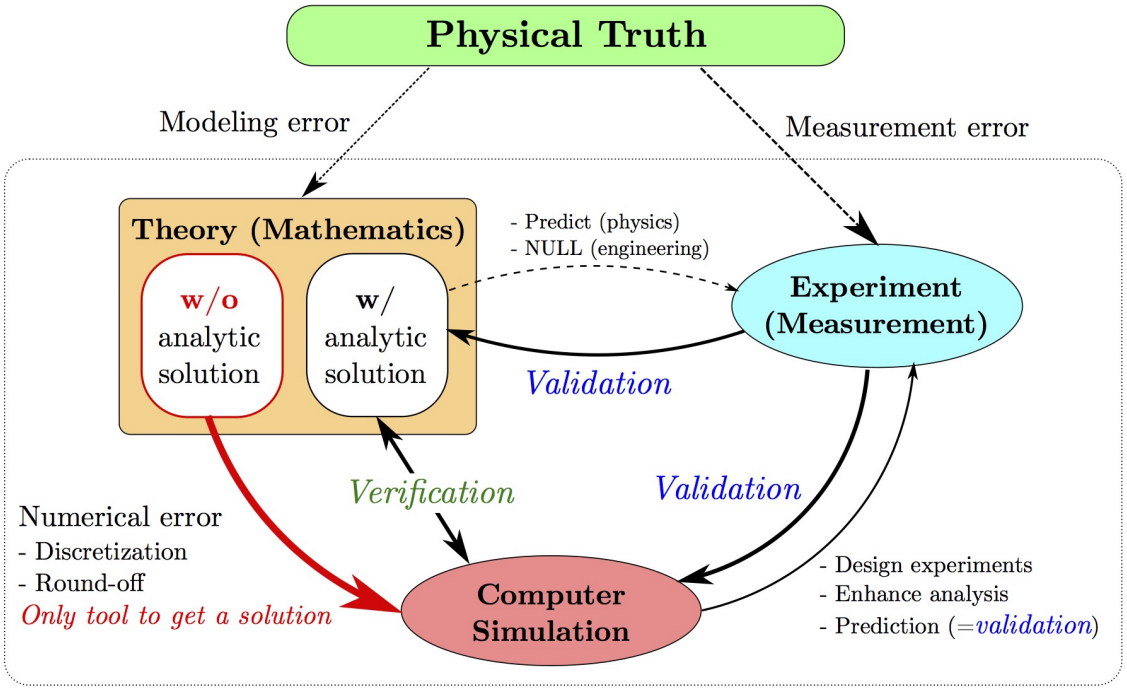

Figure 1.4: Relation between measurements, theory, and computer simulations. Figure from Plasma Dynamics Modeling Laboratory, Texas A&M University.

ever-increasing computing power [10, 26, 27, 28, 29]. While numerical methods are an important tool in research and design, they come with deficits (e.g. modeling uncertainties, numerical errors) [15, 30] so experiments will remain an important aspect in discovering a "physical truth." Given the above reasons, numerical modeling and simulations are the apparent starting point to investigate ETC's feasibility and to help guide its development. The numerical methods are discussed in Chapter II. Theory is also needed to investigate the physical phenomena, in this case ETC, which is used in the numerical modeling. Thermionic emission is not a new phenomena (Section 1.2.3) but theory has to be modified or developed in order to use it in the hypersonic flow environment. This thesis focuses on developing and implementing ETC theory into a numerical modeling approach and using it to investigate the feasibility of ETC.

1.2 Background

1.2.1 Hypersonics

In aerodynamics, flight speeds are categorized into regimes of flight or flows, which are *subsonic*, *transonic*, *supersonic*, and *hypersonic*. The keyword here is the word *sonic*, which refers to the speed of sound. The flight speeds are divided into these regimes because the flow behaves differently in each one and often require different approaches to accurately model them. If an object is traveling through the air well below the speed of sound, it is referred to as subsonic flight, or low-speed flight. As the speed of the object increases and approaches the speed of sound, some of the flow over the object will become faster than the speed of sound, but not all of it (both subsonic and supersonic flow). Supersonic flight is where the flow is entirely faster than the speed of sound. Hypersonic flight speed is generally described as being *very supersonic*. There is no discrete value at which the flow becomes hypersonic and is more of a regime where certain physical flow phenomena become more important. As a rule of thumb, speeds greater than five times the speed of sound are considered hypersonic [31]. The Mach number defines how fast an object is traveling in reference to the speed of sound. For example, flight occurring at five times the speed of sound would be Mach 5. The flow phenomena characterized by hypersonic flow include thin shock layers, an entropy layer, viscous interaction, and low-density, high-temperature flows [32, 33]. The high-temperature flow results in real-gas effects becoming important, and the flow being in state of thermal nonequilibrium and chemically reactive [34].

Hypersonic flight is characterized by very strong, oblique shocks as illustrated in Figure 1.5. As the speed is increased, the oblique shock wave moves closer to the surface and the shock layer[4] becomes very hot. Aspects of such high-temperature flows

[4]Flowfield region between shock and the body.

are that they are chemically reactive (i.e. dissociation and ionization of the gas) and often in thermal nonequilibrium [35]. These effects largely originate from the amount of energy in the flow. Flows at these high velocities inherently have a large amount of kinetic energy, which is converted to heat as it slows down and travels around the vehicle. Managing these high heating loads is vital and discussed in Section 1.2.2. Although the strong shock is oblique, the shock will be approximately normal near the leading edge. Figure 1.6 uses normal shock relations to approximate the temperature increase across the shock near the leading edge for different altitudes. The calorically perfect gas uses *ideal* gas relations and the chemically reacting gas account for real gas effects using NASA's Chemical Equilibrium with Applications (CEA) computer program [36]. The chemically reactive flow is represented by two limits: *equilibrium* and *frozen*. An equilibrium chemically reactive flow allows for energy transfer between energy modes and the flow to reach a steady-state (i.e. equilibrium). There is no energy transfer between energy modes for frozen chemically reactive flows (i.e. very nonequilibrium). The actual temperature increase behind the normal shock will lie between these two limits as the energy transfer between modes depends on the time-scale. The importance of modeling nonequilibrium is illustrated by the large difference between the two limits. By any account, the temperature increase across the shock in the nose region of a hypersonic vehicle is extremely high, leading to high-temperature flows very near the leading edge.

Modeling hypersonics, specifically aerothermodynamics, has advanced greatly in recent years [37]. From analytic methods discussed in detail in Refs. [21, 38] to higher-fidelity approaches such as computational fluid dynamics (CFD) and Direct Simulation Monte Carlo (DSMC) discussed in Refs. [25, 39, 40], modeling the phenomena involved has always been an important design tool in hypersonics. This investigation will utilize CFD and is discussed further in Chapter II.

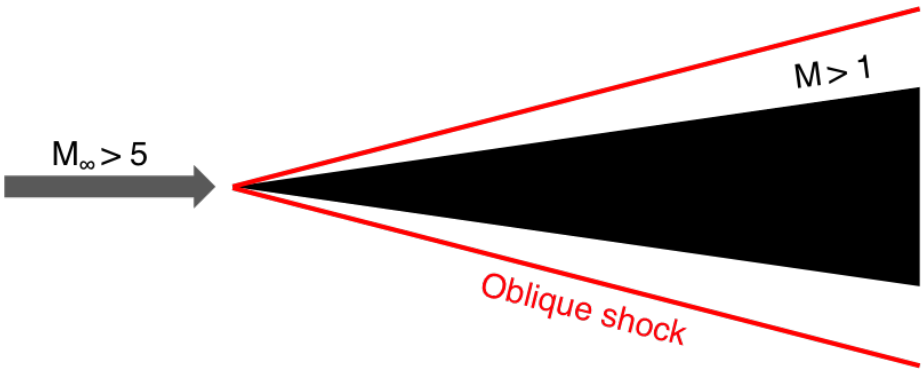

Figure 1.5: Illustration of strong, oblique shock experienced during hypersonic flight.

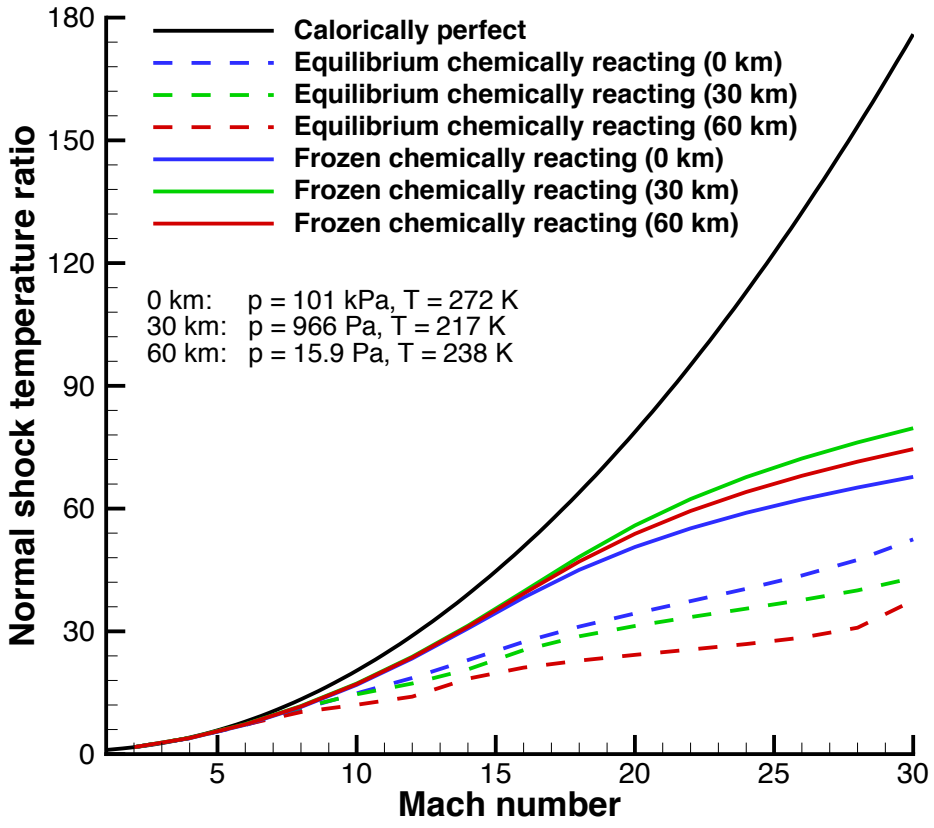

Figure 1.6: Temperature behind a normal shock wave, as a multiple of freestream temperature.

1.2.2 Thermal management

Generally, an object immersed in a flowing gas experiences some amount of heat transfer. As the speed increases, heat transfer becomes more significant. In the case of hypersonics, heat transfer is very significant with the strong shocks resulting in high-temperature flow leading to heat transfer from the flow into the vehicle called aerodynamic heating. Aerodynamic heating is such a concern in hypersonics, that it dictates the configuration of most vehicle shapes [11]. Even within hypersonics, the shape of the vehicle can greatly affect the type of flow phenomena present. For example, Figure 1.1(c) shows the X-43A that flew at Mach 9.68 with a slender shape and sharp leading edges. However, Figure 1.7 shows two vehicles that also traveled at hypersonic speeds: the Apollo 12 capsule that travelled at Mach 32 and the Space Shuttle Discovery that traveled at Mach 25, both during atmospheric reentry. The shape differences arise from whether drag is to be maximized or minimized. For reentry flight, deceleration through drag is vital requiring much blunter shapes such as the Apollo capsule. However, for hypersonic cruise and acceleration vehicles, such as the X-43A, drag is minimized in order to maximize the range, which results in high convective heat rates as shown from Eqs. 1.1 and 1.2.

Hypersonic vehicles can be classified into three distinct reference classes and their aerothermodynamic features are summarized in Table 1.1 [15, 16]:

1. *Winged re-entry vehicles* (RV-Ws): Launched into orbit via rocket and re-enter Earth's atmosphere with winged, controlled flight returning from orbit. Examples: Space Shuttle, Hermes, X-34, X-38, and Hopper/Phoenix.

2. *Non-winged re-entry vehicles* (RV-NWs): Launched into orbit via rocket and enter atmosphere uncontrolled, blunt shape often from outside orbit. Examples: Apollo, Viking, Orion.

3. *Cruise and acceleration vehicles* (CAVs): Vehicles with airbreathing propulsion

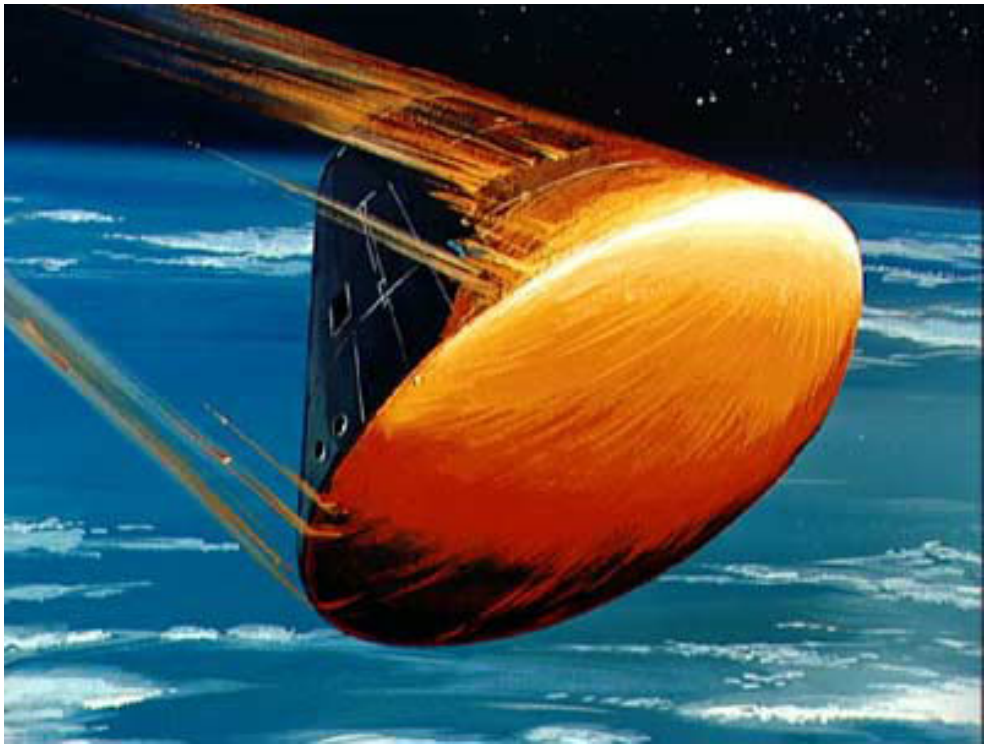

(a) *Apollo 12*: splash-down type reentry flight (11 km/s). Figure from NASA Illustrations.

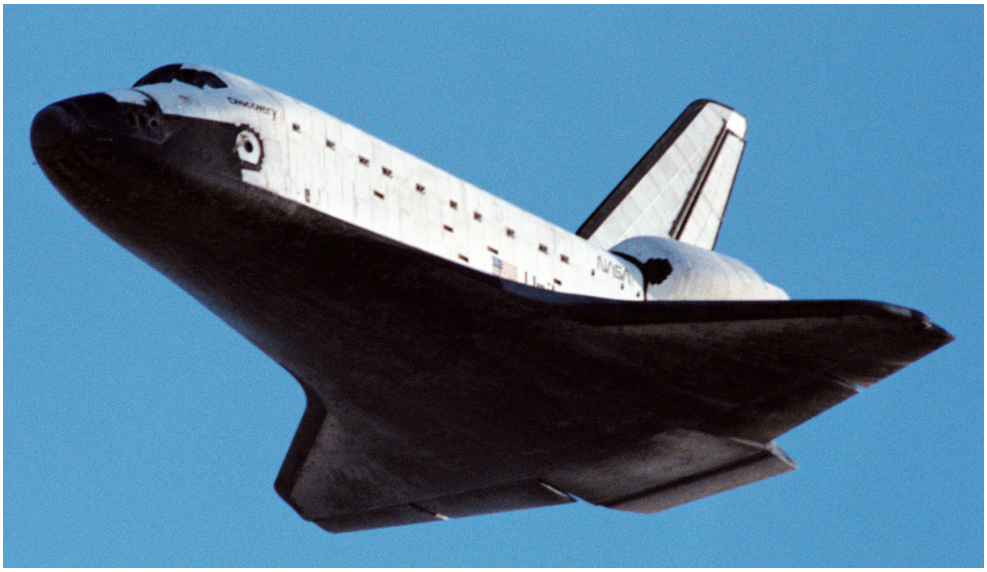

(b) *Space Shuttle Discovery*: glider type flight (7.8 km/s). Figure from NASA.

Figure 1.7: Re-entry vehicles.

(i.e. ramjet, scramjet). Examples: X-43A (Figure 1.1(c)) and X-51A.

4. *Ascent and Reentry Vehicles* (ARVs): Ideally launched into orbit using one stage (SSTO) and return to Earth without dispensing hardware. Examples:[5] NASP, Oriflamme, and the Japanese Space Plane.

Class	Winged re-entry vehicles (RV-W)	Non-winged re-entry vehicles (RV-NW)	Cruise and acceleration vehicles (CAV)	Ascent and Reentry Vehicles (ARV)
Mach number range	30-0	30-0	0-12[6]	0-28
Configuration	blunt	very blunt	slender	opposing design requirements[7]
Drag	large	large	small	small/large[8]
Flight time	short	short	long	long
Lift/drag ratio	small	zero	large	large/small[9]

Table 1.1: Aerothermodynamic features of the four reference classes of hypersonic vehicles.

Drag is desired for re-entry vehicles (RV-W, RV-NW) allowing for blunt shapes and avoiding the contradictory design requirements posed by Eqs. 1.1 and 1.2.[10] However, sustained flight vehicles (CAV, ARV) must minimize drag. The thermal environment experienced for each of these vehicles is managed by a thermal control system (TCS), also known as thermal protection system (TPS). Given that each class, especially between the vehicles designed for re-entry (RV-W, RN-NW) and sustained flight (CAV), has different design requirements, there are numerous methods of managing the thermal loads experienced, which are discussed in detail in Refs. [42, 43, 44, 45]. However, this thesis will focus on the slender vehicles, specifically the sharp leading edges, that will be required for sustained flight. There are three type of thermal

[5]No SSTO vehicle has been constructed as of this writing.

[6]Theoretical studies show that the hydrogen-fueled scramjet engine is viable up to Mach 16 and an alternative fueled scramjet possibly reaching orbital speeds [41].

[7]Slender body desired for ascent and blunt body for re-entry.

[8]Minimal drag desired for ascent and large drag desired for re-entry.

[9]Large lift desired for ascent and large drag desired for re-entry.

[10]Missiles generally also classify as another class of reentry vehicles, which are more slender due to deceleration not being required.

management systems that can be used to manage (i.e. cool) the heat that a hypersonic vehicle experiences during flight: passive, semi-passive, and active.

1.2.2.1 Passive

Passive thermal management approaches utilizes material properties in order to manage the high heat loads. These materials can withstand high-temperatures and also utilize radiative cooling[11] to divert the heat away from the vehicle. Some heat will inevitably be transfered into the structure of the vehicle through conduction. This is usually addressed by having short flight times or allowing for the vehicle structure to heat up (i.e. heat sink). Passive systems have been used extensively in RV-W and CAV type hypersonic vehicles. Benefits of passive TPS include that it is typically reusable,[12] simple, and well-tested. A type of material that meets this criteria is ulta-high temperature composites (UHTC), which were used on the X-43A [5]. Although UHTC materials have good thermal properties, they have some physical limitations such as weak fracture toughness and heavy weight that suggest they are not the ideal approach [46]. Equation 1.2 shows stagnation point heat transfer has a cubic relation with freestream velocity. So as hypersonic vehicles continue to fly faster and for longer durations, passive thermal management will not be sufficient to manage the immense heat loads predicted by Eq. 1.2.

1.2.2.2 Semi-Passive

Semi-passive thermal management approaches are very similar to passive approaches, by definition, and are often grouped together [45]. Semi-passive approaches are necessary if the heat fluxes are experienced for an extended period of time. To address the extended heat loads, a heat pipe can be used within the structure as

[11] Radiative cooling discussed in Section 2.1.1.

[12] For some passive TPS, certain components must be replaced. For example, the tiles on the Space Shuttle TPS.

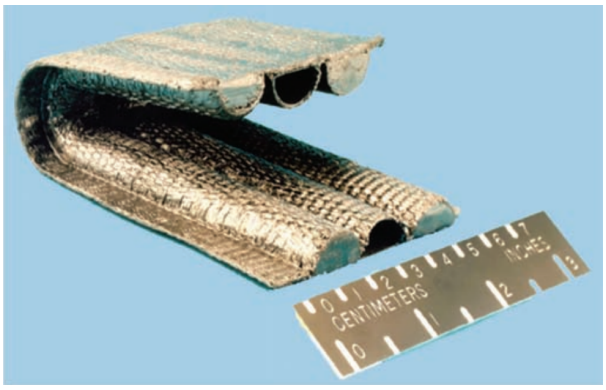

(a) Heat-pipe-cooled leading edge. Figure from NASA.

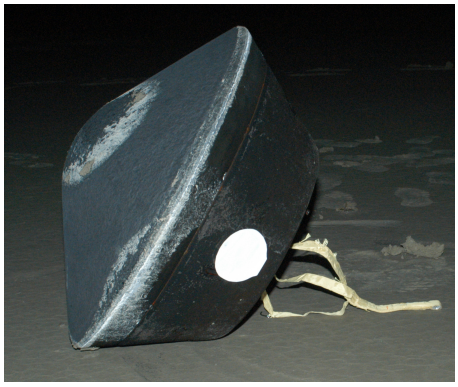

(b) *Stardust*: utilized ablation thermal protection system. Figure from NASA.

Figure 1.8: Semi-passive thermal protection systems.

shown in the vehicle leading edge in Figure 1.8(a). The heat is transferred away from the thermally intense location to another region of the vehicle where it can be radiated away. A downside to heat pipes is that the system adds weight to the vehicle and also volume is restricted with the sharp-leading edge radii. Ablation is another semi-passive approach to managing the extended heat loads. Ablating materials have significant heat management benefits primarily through a controlled thermochemical decomposition of the heat shield, which moves the heat into the flow as opposed to into the surface [47, 48, 49]. Ablation will be used for the Orion capsule and was used for the Stardust Return Capsule,[13] shown in Figure 1.8(b), and on the Apollo capsules. While ablation is appropriate for the short, thermally intensive environment of re-entry it is not ideal for sustained flight vehicles. The shape change of the surface, while permitted for the blunt bodies of re-entry flight, is unacceptable for the sharp leading edges of hypersonic vehicles as the aerodynamics of the vehicle are very sensitive to the shape and can lead to instabilities.

[13]Fastest re-entry speed into Earth's atmosphere by any man-made object, which entered at 12.9 km/s (Mach 36).

1.2.2.3 Active

As hypersonic vehicles continue to fly faster and farther, resulting in higher heat fluxes for longer durations, active cooling will be required. These approaches include convective cooling, film cooling, and transpiration cooling. Convective cooling involves the heat being transferred to a coolant flow through forced liquid convection within the structure. This system, like heat-pipe-cooled systems, will be limited by the size of the leading edge and also adds weight to the vehicle. Both film cooling and transpiration cooling manage the heat loads by injecting a coolant *into* the flow. Film cooling typically injects the coolant from a discrete location upstream of the thermally intense surface. This is appropriate for propulsion systems (e.g. within scramjets, rocket nozzles) but is not feasible for a leading edge. Transpiration cooling utilizes a porous structure where the coolant is injected through the pores continuously over large areas. The concept of transpiration cooling consists of allowing a gas (e.g. air, helium) to transpire through the porosity in the vehicle's surface and results in a lower heat flux at the surface [50]. A drawback to transpiration cooling, in this definition,[14] at the leading edges of hypersonic vehicles would be the coolant flow through the pores that could be impeded at the stagnation point due to the high stagnation pressure.

1.2.2.4 Electron Transpiration Cooling

Managing the intense heat loads experienced at the sharp, leading edges of vehicles during sustained hypersonic flight is a demanding prospect. The ideal TPS would reject more heat, with lower volume and mass requirements, and be suitable for use on sustained flight (i.e. non-degradable, no shape change) than any of the previous mentioned techniques. The theory behind ETC as a viable TPS system is provided

[14]The coolant used for transpiration cooling is typically a gas such as air or helium. ETC uses electrons as the transpiration species.

in Section 2.1.1. ETC utilizes thermionic emission, discussed in Section 1.2.3, and is similar to transpiration cooling but would use electrons instead of a gas. The transpiration cooling effect would not require a porous material as the electrons are emitted from the material surface. However, there are challenges to using ETC, which will be discussed in Section 5.3.5. A recent study using a simple 1D model [22], showed that ETC can be effective in an example hypersonic trajectory. This work did not account for any of the complex flow physics that can occur during hypersonic flight such as nonequilibrium and ionization. This thesis will complete such analysis that includes these nonlinear processes in order to better understand the viability of ETC.

1.2.3 Thermionic emission

Although ETC is a recently proposed approach, the underlying phenomenon, thermionic emission, is a well-studied field [51, 52, 53, 54, 55]. Motivation for studying thermionic emission stems from a common form of energy (i.e. power) conversion, where thermal energy can be directly converted to electricity and vice versa [56, 57, 58, 59]. Essentially, thermionic emission involves charged particles[15] being emitted from a heated source or the direct conversion of heat into electricity. The electrons are emitted when the thermal energy given to them is greater than the binding potential of the surface material. The binding potential of the material is defined as the work function. A material with a lower work function requires less thermal energy for an electron to be emitted.

The phenomenon was discovered by Edmond Becquerel over four decades before J.J. Thomson first identified the electron in 1897 [60, 61]. The relationship between heat and electricity was further advanced when Frederick Guthrie rediscovered the phenomenon in 1873 and noticed that certain metals when heated in air give off

[15]Electrons are typically the charged species emitted although ions can be emitted as well. This thesis will only consider electron emission.

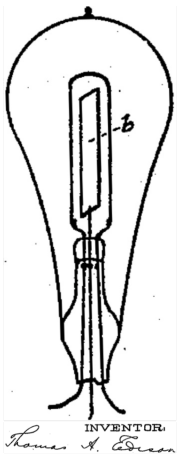

(a) Incandescent light bulb. Figure from U.S. Patent Office.

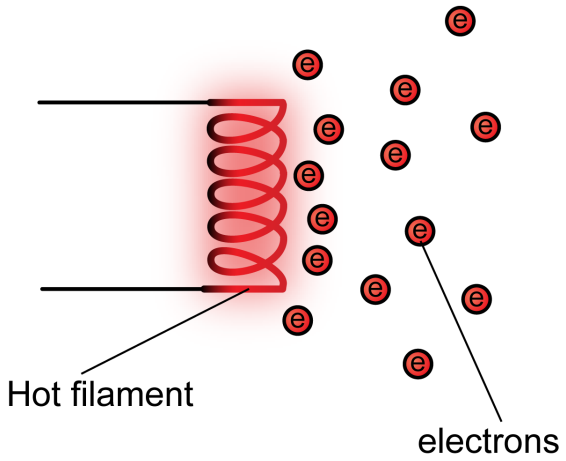

(b) Schematic of emission of electrons from hot metal.

Figure 1.9: *Edison Effect*: Emission of a current of electrons from a hot metal to a positively charged plate.

net amounts of positive electricity at lower temperatures and net amounts of negative electricity at higher temperatures [62]. The effect was discovered once again by Thomas Edison in 1880 while trying to explain the reason for breakage of lamp filaments and uneven blackening (darkest near the positive terminal of the filament) of the bulbs in his incandescent lamps shown in Figure 1.9(a) [63]. Edison observed a passage of a negative stream of electricity through a vacuum from an incandescent carbon filament to an adjacent metal plate that was positively charged relative to the filament. This led to the first electronic device patent [64]. This effect is shown in the schematic in Figure 1.9(b). The current increased with the filament temperature and there was no current when the plate was negatively charged relative to the filament. This one way current became known as the *Edison Effect*[16] [65].

At the beginning of the 20th century, O. W. Richardson[17] made contributions to thermionic emission that would be the foundation for all future work, including this thesis. In 1901, Richardson published a paper that detailed his experiments and showed that the current from a heated wire increased exponentially with the

[16]Occasionally used as a synonym for thermionic emission.
[17]J. J. Thomson was his doctoral advisor.

temperature of the wire [66] and he published another paper in 1903 that showed the presence of gas complicates emission greatly [67]. Richardson later proposed an emission law that followed an Arrhenius form [68]:

$$J_e \propto T_w^2 \exp\left(\frac{-W_F}{T_w}\right), \tag{1.3}$$

where J_e is the emission current density, T_w is the surface temperature and W_F is the material work function.[18] This equation became known as Richardson's law[19] and showed the relation between material properties (e.g. work function, temperature) and the amount of electron current from the surface in ideal conditions (i.e. vacuum, no retarding electric field). How thermionic emission affects heat transfer is discussed in Section 2.1.1 and how non-ideal conditions (e.g. hypersonic flight) can affect electron emission is presented in Chapter II.

Although using thermoelectric materials as a mechanism to reduce the thermal load on hypersonic vehicles is a recent approach, employing thermionic emission in high-speed flight is not a novel concept. In the 1960s, there was an interest to use thermoelectric materials on the nose of reentry vehicles and collect the emitted electrons as a source of power generation [69, 70]. Experiments were performed using the plasma arc tunnel at the Sandia Corporation using a range of different flow conditions, emissive materials, and geometries [71]. The modeling approach for ETC is evaluated using these experiments [72] and is presented in Chapter IV.

[18] Work function is essentially how much energy it requires a certain material to emit an electron. This property is discussed further in Section 2.1.1.

[19] Richardson received the 1928 Nobel Prize in Physics "for his work on the thermionic phenomenon and especially for the discovery of the law named after him."

1.3 Thesis Outline

This thesis is divided into six chapters. Chapter II presents the modeling approach used to investigate ETC from flowfield, plasma sheath, and material perspectives. The chapter also includes conditions of interest and the heat transfer theory involved in determining the surface temperature. The numerical results are detailed in Chapter III, which include a test case description, flowfield features, and how certain physics affect ETC peformance. In Chapter IV, results from the modeling approach are compared to a set of experimental measurements. The thesis is concluded in Chapter V, where the key points of interest from the previous chapters and areas that represent novel work are highlighted. Suggestions are also made for future research on ETC.

CHAPTER II

Modeling Approach

2.1 Introduction

Chapter I motivated the focus of this thesis as investigating ETC using numerical modeling. This chapter will detail the heat transfer theory involved as well as define the conditions of interest. The conditions of interest are discussed to justify the modeling approaches and corresponding assumptions. Finally, the modeling approaches to investigate ETC are presented including the modeling for the flow, plasma sheath, and material response.

2.1.1 Heat transfer theory

The thermal state of the leading edge of a hypersonic vehicle is defined by its surface temperature and the heat flux going into the surface. Energy must be conserved so that at steady state the heat flux going into the surface must equal the heat flux going away of it. Nature uses three physical sources to heat the vehicle surface: thermal conduction, mass diffusion, and radiation that combine to form aerodynamic heating. Thermal conduction, q_{cond}, occurs when there are temperature gradients in

the flow and is governed by Fourier's law of heat conduction,

$$q \propto \frac{\partial T}{\partial y}, \tag{2.1}$$

where q is the heat transfer rate. There are also species gradients in the flow that lead to mass diffusion heat transfer, q_{diff}. The sum of mass diffusion and thermal conduction heat transfer will be referred to as convective heat transfer, q_{conv}. Hypersonic flight is characterized by large temperature gradients in the flow that is most epitomized by a high-temperature gas flowing near a cool vehicle surface as shown in Figure 1.5 resulting in the high convective heating rates predicted by Equation 1.2.

If the shock-layer temperature is high enough, the gas itself can radiate heat to the surface called radiative heating. The intensity of the radiation is dependent on the volume of the high-temperature gas, which leads to radiative heating being more intense for blunt shapes.[1] According to Martin [73], radiative heating begins to be comparable to convective heating for a 30 cm radius sphere traveling over 12 km/s and is proportional to $\rho_\infty^{1.6} u_\infty^{8.5} R_n$. Since this thesis focuses on sharp-leading edges with a maximum velocity of 8 km/s (i.e. orbital velocity), radiative heating will be negligible and not considered.

The heat flux away from the surface can either go into the flow or into the vehicle. The heat flux into the vehicle is called in-depth surface conduction, q_{in}, and is also governed by Fourier's law of heat conduction, so it is driven by the temperature gradients in the material. Radiative cooling is typically the main form of heat transfer away from a hot surface, especially at the leading edge,

$$q_{rad} = \epsilon \sigma_{sb} T_w^4, \tag{2.2}$$

where T_w is the surface temperature, ϵ is the material emissivity, and σ_{sb} is the Stefan-

[1] Radiative heating was more than 30% of the aerodynamic heating of the Apollo re-entries.

Boltzmann constant. The flowfield is assumed to be optically thin (i.e. transparent)[2] so the heat from radiative cooling does not go into the flow but *through* it, which is an appropriate assumption for a sharp leading edge in a hypersonic flow [74].

The recently proposed ETC process is another mode of heat transfer away from the surface and towards the flow. ETC can be viewed as an *evaporation* of electrons from the hot surface and is in some ways analogous to how evaporation of molecules from liquid results in a cooler surface. For a liquid molecule to evaporate, it requires energy (e.g. heat) that is supplied to the liquid surface, and if steady-state evaporation is to occur, it would require a source of heat provided to the liquid surface. ETC is similar in that if the surface is hot enough, electrons will be emitted although the particles are a charged species and much smaller than liquid vapor. This phenomenon of converting heat into a current electrons or electricity is called thermionic emission, which is discussed in Section 1.2.3.

The emitted electrons carry away energy from the vehicle surface determined by the electrons overcoming the potential barrier and the kinetic energy associated with the emitted electrons resulting in a heat flux of [68]:

$$q_{ETC} = J_e\left(W_F + \frac{2k_B T_w}{e}\right). \tag{2.3}$$

The work function, W_F, is defined as the difference between the electrochemical potential of the electrons just inside the material surface and the electrostatic potential energy of an electron in a vacuum just outside the surface. Electrons are retained in the material surface and do work overcoming the potential barrier and escaping the material, so the work function is essentially the minimum energy required to remove an electron from a material. A material with a lower work function would require less thermal energy for an electron to be emitted. The material work function for ETC of leading edges would ideally be small and is discussed in Section 3.2.

[2]Ratio of the mean free path of photons to dimensions of the gas is large.

Richardson also showed that when electrons escape the hot body, they carry with them a kinetic energy on average of $2k_BT_w$ [67]. It is to be noted that the average kinetic energy of emitted electrons ($2k_BT_w$) is greater than the average kinetic energy of electrons in a unit volume at equilibrium ($\frac{3}{2}k_BT_w$). The larger value arises from the fact that more rapidly moving particles occur more frequently in an emitted stream than in a volume at equilibrium, on average [67]. More details of the derivation of Equation 2.3 can be found in Refs. [51, 68].

In ideal conditions,[3] the electron current density is a function of the material's surface temperature and work function as determined by Richardson [66, 68]:

$$J_{e,sat} = A_R T_w^2 \exp\left(\frac{-eW_F}{k_B T_w}\right), \tag{2.4}$$

where A_R is often referred to as the Richardson constant defined given by [75],

$$A_R = \frac{4\pi m_e k_B^2 e}{\hbar^3} \approx 1.20 \times 10^6 \text{ A/m}^2/\text{K}^2, \tag{2.5}$$

where $\hbar$ is the Planck constant and m_e is the mass of a single electron. It is to be noted that there is typically a material-specific correction factor typically on the order of 0.5 applied to the Richardson constant [76, 77] but this work will assume this correction factor is unity. This is due to the materials that will be used in ETC being currently developed and their exact material properties being largely unknown, as discussed in Section 3.2.3. This electron current density will be referred to as the saturation current as it is the maximum amount of current possible based on material properties (surface temperature and work function) and rises very quickly with increasing surface temperature.

ETC can be compared to radiative cooling using the ratio of heat flows away from

[3]Emitted electrons see no retarding electric field at the surface, are not reflected back to the surface through collisions, or see a virtual cathode created by space-charge limit.

the surface that is defined as,

$$\iota = \frac{q_{ETC}}{q_{rad}}, \tag{2.6}$$

and is plotted as a function of surface temperature and work function in Figure 2.1. When the ratio of ETC to radiative heat transfer (ι) is unity that means the surface is being cooled equally by ETC and radiative cooling. When $\iota > 1$, that means ETC is a more effective cooling mechanism than radiation. The cooling power of ETC rises very quickly with temperature and is a more effective cooling mechanism than radiative cooling for lower work functions and higher surface temperatures. The heat transfer provided by ETC depends on the emission current from the surface, so it is important to accurately determine this current. Blackbody radiation ($\epsilon = 1$) was assumed for the radiative cooling.[4] It is to be noted that ETC does not replace radiative cooling but supplements it. The saturation current is used in Figure 2.1, which assumes ideal emission conditions. Non-ideal conditions can limit the emission, which can lower the cooling power of ETC, and are discussed in Section 2.5, but Figure 2.1 shows the high potential of cooling power provided by ETC and motivation to accurately determine the level of emission. It is to be noted that ETC lacks charge neutrality in that a negative current (i.e. electrons) is emitted into a quasineutral flowfield. This could lead to some challenges since nature tends to desire charge neutral processes and motivates why the electric field is modeled as discussed in Section 2.3.

A schematic of the heat transfer at the surface is shown in Figure 2.2. The temperature of the surface is determined by balancing the heat transfer at the surface under steady state conditions,

$$q_{conv} = q_{in} + q_{rad} + q_{ETC}, \tag{2.7}$$

[4]Blackbody radiation is the most effective cooling radiation can provide. Grey body radiation ($\epsilon < 1$) is more typical so radiation would be less effective.

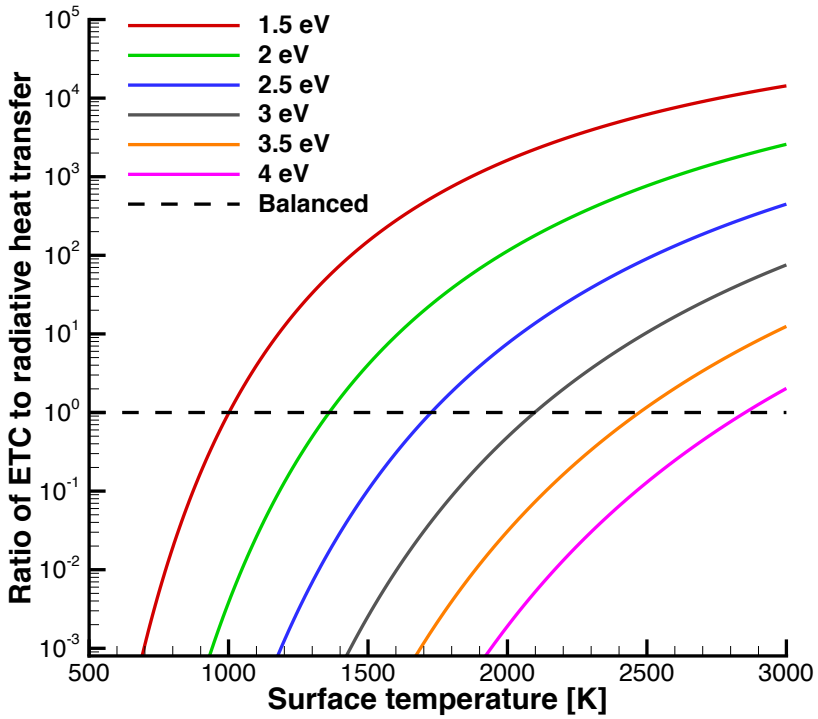

Figure 2.1: Ratio of ETC to radiative cooling effectiveness for various material work functions and surface temperatures where ETC is modeled using saturation current (i.e. Richardson current).

where the convective heat transfer is determined by gradients in the flow (e.g. temperature, species), the in-depth surface conduction determined by temperature gradients in the material, radiative heating determined by the surface temperature, and ETC cooling determined by the emission current density. Radiative cooling involves photons (p) leaving the surface and ETC involves electrons (e) leaving the surface.

2.1.2 Conditions of interest

Since ETC is a proposed mode of thermal management for slender hypersonic cruise vehicles, slender shapes at conditions typical of hypersonic flight will be considered. The X-43A is at the frontier of sustained hypersonic flight, so the conditions used for that flight will be used as the baseline (e.g. velocity, altitude). As motivated in Chapter I, the leading edges of these vehicles are the most susceptible to aerodynamic heating so this region will be the area of interest. Equation 1.1 revealed that

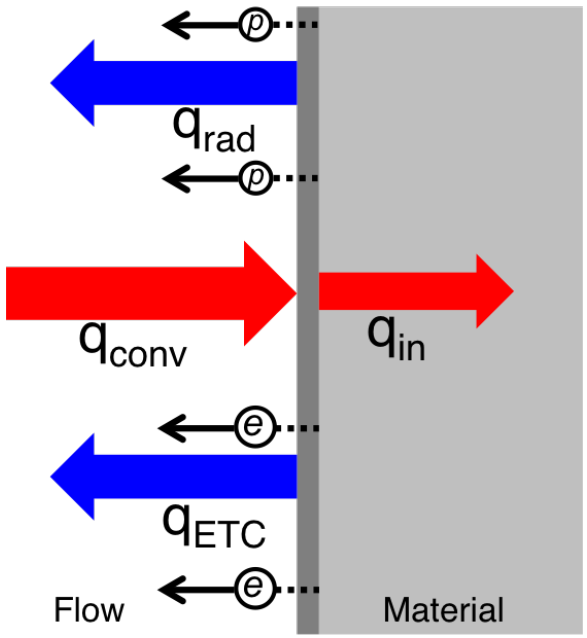

Figure 2.2: Heat fluxes at the surface of the hypersonic vehicle.

sharper leading edge radii will result in less drag and the X-43A used a very sharp leading edge radius of 0.13 cm to minimize the drag. However, this sharp leading edge was difficult to manufacture [78] and for this reason, the smallest leading edge radius considered in this thesis will be 0.1 cm. The maximum velocity of the X-43A was approximately 3.3 km/s at approximately 30 km altitude which guides the slowest velocity considered in this thesis to be 3 km/s. The fastest velocity will be orbital velocity (i.e. 8 km/s). The lowest altitude considered will be 30 km and the validity of modeling approach with increasing altitude will determine the maximum altitude investigated as discussed in Section 2.2.

2.2 Flowfield

The type of flow regime the hypersonic flight is in will determine which fluid modeling approach is used as well as the validity of it. One hypersonic vehicle can experience different flow regimes during a typical flight trajectory due to the variation of speed and atmospheric density with altitude. Also, the size or characteristic length

of the vehicle can affect the type of flow regime experienced. For example, the flow regime experienced by the Space Shuttle which had a wing span of almost 24 meters could be very different from sharp-leading edges considered in this study while both being hypersonic vehicles. The flow is typically characterized by what regime it is in, with one end of the extreme being rarefied gas and the other end continuum. In between these two regimes is the transitional regime, where assumptions in the continuum flow break down and rarefied gas effects become more important. The Knudsen number, Kn, is used to help determine which regime the flow is in,

$$Kn = \frac{\lambda}{L}, \tag{2.8}$$

where L is the characteristic length and λ is the mean free path given below for a hard sphere molecule,

$$\lambda = \frac{1}{\sqrt{2}\pi n \delta_c^2}, \tag{2.9}$$

where n is the number density of the flow and the kinetic collisional diameter, δ_c, is approximated by [79],

$$\delta_c^2 \approx \frac{m}{9\mu}\sqrt{\frac{3p}{\rho}}, \tag{2.10}$$

where μ is the viscosity and is approximated using the Sutherland-law [80] and the pressure and density of the air is calculated using an empirical atmosphere model [81].

Figure 2.3 presents the different types of flow regimes the leading edges of hypersonic vehicles will experience with increasing altitude. The mean free path steadily increases with increasing altitude due to the density of the atmosphere decreasing. Due to the increasing mean free path, the Knudsen number also increases with al-

titude. At low altitudes, the atmospheric density is relatively high and the flow is in the continuum regime that can be accurately simulated using CFD, which is relatively computationally inexpensive. It is to be noted that CFD is referred to in this work in the *traditional* sense (i.e. solving the Navier-Stokes equations numerically). However, as the density decreases with altitude, each of the characteristic lengths eventually reaches the regime of flow between continuum and free-molecular, called the transitional regime. This regime is characterized by both continuum and rarefied gas features. In this regime, the continuum approximation is less accurate and slip effects can be present lowering the accuracy of CFD in this regime. CFD modeling can still be used in the transitional regime as the effects are expected to be small, especially at lower Knudsen numbers [82]. Each of the characteristic lengths reaches the free-molecular (i.e. rarefied gas) regime at high-altitudes. For this regime, CFD is no longer a valid approach and the Boltzmann equation should be solved numerically. One common approach to solve the Boltzmann equation is DSMC. This approach represents atoms and molecules through out the flowfield as populations and simulating collisions on a probabilistic basis to model the underlying physics in the flow [83]. Given that a majority of the expected flight trajectory will be in the continuum and transitional regime, this thesis will use CFD to investigate ETC. Future work will be reserved for improving the accuracy of CFD modeling in the transitional regime by accounting for slip effects or using a hybrid particle-continuum method [40]. Investigating ETC in the free molecular regime with DSMC will also be reserved for future work.

The Reynolds number helps predict how susceptible the flow is to turbulence, and is defined as,

$$Re = \frac{2\rho_\infty u_\infty R_n}{\mu}. \tag{2.11}$$

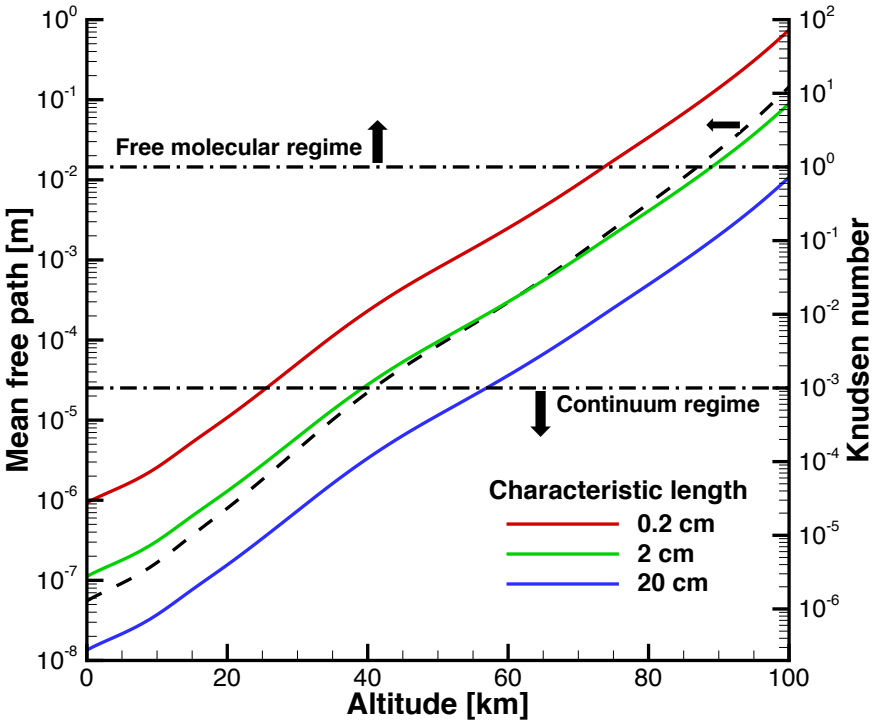

Figure 2.3: Flow regime versus altitude for different characteristic lengths of leading edge. Dashed black line denotes mean free path and colored lines correspond to Knudsen number.

As Re increases, the flow changes from laminar through a transition region to a turbulent regime. Experimental data for hypersonic viscous flow over a sharp cone,[5] concluded that the flow is entirely laminar at Reynolds numbers of 3×10^6 or less [84]. Figure 2.4 presents the freestream diameter based Reynolds number for different leading edge radii and freestream velocities with increasing altitude. For most of the cases considered and especially at the higher altitudes, the flow will be laminar near the leading edge. Downstream of the leading edge the flow is more susceptible to turbulence due to the increase in characteristic length and is an active area of research [85].

[5]Mach 10 freestream over a 8-deg cone.

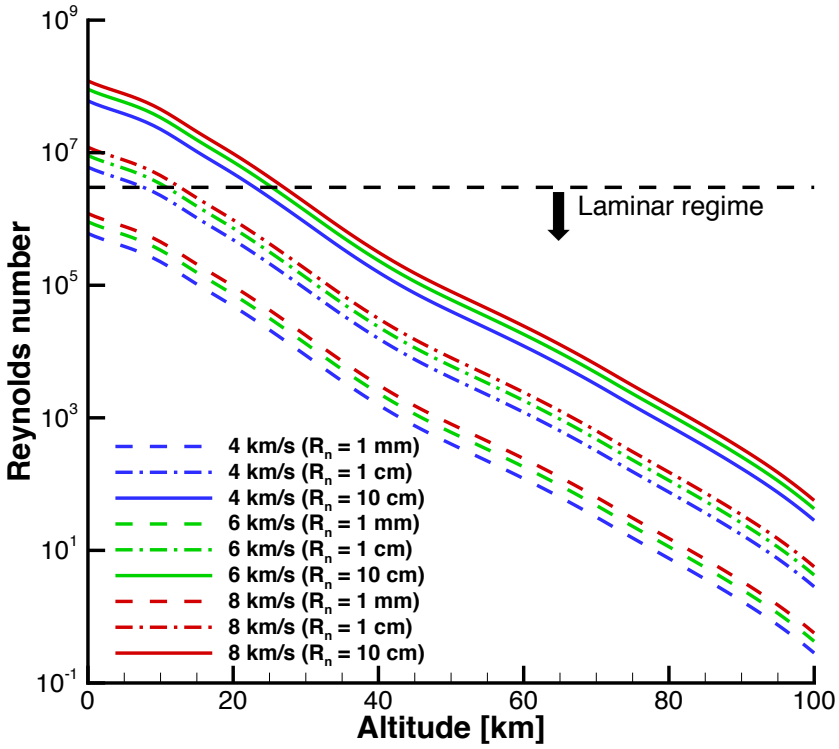

Figure 2.4: Reynolds number versus altitude for different characteristic lengths of leading edge at different freestream velocities.

2.2.1 Fluid

The numerical simulations of the fluid are performed using the CFD code LeMANS, which was developed at the University of Michigan for simulating hypersonic reacting flows [86, 87]. LeMANS is a parallel, three-dimensional code that solves the Navier-Stokes equations on unstructured computational grids. LeMANS includes thermo-chemical non-equilibrium effects and the flow is modeled assuming that the continuum approximation is valid. The approach used for modeling ETC assumes that the translational and rotational energy modes can be described by a single temperature, T_{tr}, and that the vibrational and electron translational energy modes are described by an another single temperature, T_{ve}. This assumes that the rotational mode is fully-excited, which is appropriate in this regime of flow[6] [21, 88].

LeMANS is capable of modeling turbulence although the presented work is as-

[6]Rotational temperature tends to equilibrate very quickly with translational temperature.

sumed to involve laminar flow, which is an appropriate assumption since the sharp leading edge is the only region of interest[7] [11, 89].

The fluid conservation equations solved by LeMANS to simulate flows with thermal nonequilibrium and finite-rate chemical reactions can be written as [86, 90],

Conservation of Mass

$$\frac{\partial \rho_s}{\partial t} + \nabla \cdot (\rho_s \mathbf{u} + \mathbf{J}_s) = \dot{w}_s \tag{2.12a}$$

Conservation of Momentum

$$\frac{\partial \rho \mathbf{u}}{\partial t} + \nabla \cdot \left(\rho \mathbf{u}\mathbf{u} + p\bar{\bar{I}} - \bar{\bar{\tau}} \right) = 0 \tag{2.12b}$$

Conservation of Energy

$$\frac{\partial E_t}{\partial t} + \nabla \cdot \left((E_t + p)\mathbf{u} - \bar{\bar{\tau}} \cdot \mathbf{u} + (\mathbf{q}_{tr} + \mathbf{q}_{ve}) + \sum_s (\mathbf{J}_s h_s) \right) = 0 \tag{2.12c}$$

$$\frac{\partial E_{ve}}{\partial t} + \nabla \cdot \left(E_{ve}\mathbf{u} + \mathbf{q}_{ve} + \sum_s (\mathbf{J}_s e_{ve,s}) \right) = \dot{w}_{ve} \tag{2.12d}$$

where ρ_s is the density of species s, $\mathbf{u}$ is the bulk velocity, p is the pressure, $\bar{\bar{I}}$ is the identity matrix, $\bar{\bar{\tau}}$ is the viscous stress tensor, h_s is the species enthalpy, and $\mathbf{J}_s$ is the diffusion flux of species s modeled using a modified form of Fick's law [91]. E and E_{ve} are the total and vibrational-electron-electronic energies per unit volume of mixture, respectively, while $e_{ve,s}$ is the vibrational-electron-electronic energy per unit mass. The source term $\dot{w}_s$ in Equation 2.12a is the species mass production and recombination (i.e. destruction) rate due to chemical reactions. The source term $\dot{w}_{ve}$ includes the energy transfer between nonequilibrium modes, the change of vibrational energy due to chemical reactions, and an approximation to the work done on the electrons by the electric field induced by the electron pressure gradient [86]. The heat fluxes in the energy conservation equations, $q_{t,ve}$, are modeled according to

[7] This assumes the flow does not reach boundary layer transition near the leading edge, which is an appropriate assumption.

Fourier's law as,

$$\mathbf{q}_{tr,ve} = -\kappa_{tr,ve} \nabla T_{tr,ve}. \tag{2.13}$$

The viscous stresses are modeled assuming the flow is a Newtonian fluid and Stokes' hypothesis is applicable [89] and computed using cell-centered and nodal values. The mixture transport properties are calculated using two different approaches, depending on flow characteristics. The first uses Wilke's semi-empirical mixing rule [92] where Eucken's relation [79] is utilized for species thermal conductivities, κ, and Blottner's curve fits [93] for species viscosities. This simple model is appropriate for flow where the maximum temperature is less than 10,000 K as it lacks capabilities to accurately represent ionized flow transport properties [94]. As will be shown in Section 3.3, the maximum flowfield temperature often exceeds 10,000 K, so a second approach is utilized using a more accurate model, especially for ionized flow, as suggested by Palmer and Wright [94]. This approach uses Gupta's mixing rule [95] where the thermal conductivities and species viscosities are determined using non-coulombic/coulombic collision cross section data [96]. A standard finite-rate chemistry model is used for eleven species reactive air, and Park's two-temperature model [34] is used to account for the effects of thermal non-equilibrium on the forward and backward reactions rates.

The partial derivatives in Equations 2.12 can be expressed in terms of conserved variables, $\mathbf{Q}$, inviscid flux, $\mathbf{F}$, viscous flux, $\mathbf{F}_v$, and source terms, $\mathbf{S}$,

$$\frac{\partial \mathbf{Q}}{\partial t} + \nabla \cdot (\mathbf{F} + \mathbf{F}_v) = \mathbf{S} \tag{2.14}$$

$$\mathbf{Q} = \begin{pmatrix} \rho_1 \\ \vdots \\ \rho_{NS} \\ \rho\mathbf{u} \\ E_t \\ E_{ve} \end{pmatrix}, \qquad \mathbf{S} = \begin{pmatrix} \dot{w}_1 \\ \vdots \\ \dot{w}_{NS} \\ 0 \\ 0 \\ \dot{w}_{ve} \end{pmatrix},$$

$$\mathbf{F} = \begin{pmatrix} \rho_1\mathbf{u} \\ \vdots \\ \rho_{NS}\mathbf{u} \\ \rho\mathbf{u}\mathbf{u} + p\bar{\bar{I}} \\ (E_t + p)\mathbf{u} \\ E_{ve}\mathbf{u} \end{pmatrix}, \qquad \mathbf{F}_v = \begin{pmatrix} \mathbf{J}_1 \\ \vdots \\ \mathbf{J}_{NS} \\ -\bar{\bar{\tau}} \\ -\bar{\bar{\tau}}\mathbf{u} + (\mathbf{q}_{tr} + \mathbf{q}_{ve}) + \sum_s (\mathbf{J}_s h_s) \\ \mathbf{q}_{ve} + \sum_s (\mathbf{J}_s e_{ve,s}) \end{pmatrix}.$$

In LeMANS, the set of governing equations is solved using the finite-volume method applied to unstructured grids with second-order spatial accuracy. A modified Steger-Warming Flux Vector Splitting scheme [97] is used to discretize the inviscid fluxes across cell faces. Several validation studies for LeMANS have been conducted in the hypersonic flow regime [86, 98, 99, 100, 90]. More details of LeMANS can be found in Refs. [86, 90].

2.2.2 Electron emission

A boundary condition is implemented into LeMANS to model thermionic emission at the material surface. The production rate of electrons is calculated by,

$$\dot{w}_e = \frac{J_e}{eN_{Av}} - \sum_i \dot{w}_i, \tag{2.15}$$

where $\dot{w}_i$ is the surface recombination rate of ions, which is calculated assuming the the surface is fully catalytic to ions [101],

$$\dot{w}_i = \frac{\rho_i}{M_i}\sqrt{\frac{R_u T_w}{2\pi M_i}}. \tag{2.16}$$

The electron current density is determined by Equation 2.4, which is a function of the material's surface temperature and work function. It is to be noted that this current is only realized in ideal conditions: emitted electrons see no retarding electric field at the surface, are not reflected back to the surface through collisions, or see a virtual cathode created by space-charge limits. The hypersonic flow environment near the leading edges is not typical of the aforementioned ideal conditions, and the effects these real hypersonic emitter conditions have on the level of emission are discussed in Section 2.5.

The introduction of electrons from the surface impact the conservation equations in Equation 2.12. The gas properties at the surface of the hypersonic vehicle are calculated in LeMANS by solving the species mass balance affecting the boundary condition of Equation (2.12a),

$$\rho_w D_{s,w} \nabla Y_{s,w} + \dot{m} Y_{s,w} = M_s \dot{w}_s, \tag{2.17}$$

and momentum balance altering the boundary condition of Equation (2.12b),

$$p_n + \rho_n u_n^2 = p_w + \frac{\dot{m}^2}{\rho_w}, \tag{2.18}$$

to obtain the species mass fractions ($Y_{s,w}$), gas density (ρ_w), and gas normal velocity (u_w). The mass blowing rate, $\dot{m}$, is defined as the product of the electron production rate and the electron mass,

$$\dot{m} = m_e \dot{w}_e \,. \tag{2.19}$$

The effect of electron emission on the conservation of energy, Equations (2.12c)-(2.12d), is discussed in Sections 2.3 and 2.5.

2.3 Electric field

Although electron flows in many respects are analogous to a gas, two important differences arise from electrons having a much smaller value of molecular weight and also carrying an electric charge, the strongest of intermolecular forces. Given that a large current of electrons will be emitted from the leading edge, this leads to a large amount of negative charge near the vehicle. This charge imbalance can produce an electric field that may influence the ionized flow near the hypersonic vehicle and change the cooling effect of ETC. LeMANS is modified in order to account for the electric field, to some extent, and to approximate the effects the electric field[8] can have on ETC. Starting with the generalized Ohm's law [102],

$$\nabla \cdot \Big[\tilde{\sigma} \cdot \Big(\mathbf{E} + \mathbf{u} \times \mathbf{B} \Big) \Big] = 0, \tag{2.20}$$

[8]Virtual cathodes and space-charge effects are considered in Section 2.5.

and defining the electric field as the divergence of the electric potential,

$$\mathbf{E} = -\nabla\phi. \tag{2.21}$$

Equation 2.20 can be written as,

$$\nabla \cdot (\tilde{\sigma} \cdot \nabla\phi) = \nabla \cdot \Big(\mathbf{u} \times \mathbf{B}\Big). \tag{2.22}$$

Magnetic field effects are neglected in this work due to the small Hall parameter,[9] which leads to $\mathbf{B} \approx 0$ and the conductivity tensor, $\tilde{\sigma}$, becoming a scalar,

$$\nabla \cdot (\sigma \cdot \nabla\phi) = 0. \tag{2.23}$$

Equation 2.23 states that the electric current density, $\vec{j}$, is conserved,

$$\vec{j} = \sigma\mathbf{E} \tag{2.24a}$$

$$\nabla \cdot \vec{j} = 0. \tag{2.24b}$$

Several models exist to calculate the electrical conductivity of the plasma in a hypersonic flow, which is discussed in detail in Refs. [98, 103]. Since the flow is *weakly* ionized,[10]

$$\alpha = \frac{n_e}{n} \ll 1, \tag{2.25}$$

where n is the number density of neutral particles in the flowfield, a model developed

[9]Magnetic field discussed in Section 2.4.

[10]Flowfield features of conditions of interest with ETC are presented in Section 3.3.

by Chapman and Cowling for a weakly-ionized gas will be utilized in this work [104],

$$\sigma = 3.34 \times 10^{-12} \frac{\alpha}{Q\sqrt{T}} \quad [\text{mho/cm}], \tag{2.26}$$

where Q [cm^2] is the collision cross section of the gas. A constant value of $Q \simeq 5 \times 10^{-17}$ cm^2 will be used as it is unclear what the best choice for Q is and this value produced results consistent with other semi-analytic approaches across the range of interest [98]. This semi-analytic model was evaluated using a continuum Boltzmann solver [105] for conditions typical of hypersonic flight and agreed well with the Boltzmann solutions for electrical conductivity compared to other semi-analytic and empirical models [98].

Equation 2.23 is solved at each CFD iteration using a parallel implementation of the successive over-relaxation (SOR) technique to find the distribution of the electric potential in the flowfield. Different computational boundary conditions are used depending on whether ETC is present or not. For simulations without ETC (i.e. no emission), a zero-gradient condition is used at the inlet, outlet, and symmetry computational boundaries. At the wall (i.e. vehicle surface), the electrical potential is calculated by assuming the flowfield ion and electron fluxes are equal at the wall [102, 106],

$$\phi_w = \frac{k_B T_e}{e} \log \left(\frac{n_i}{n_e} \sqrt{\frac{2\pi m_e (T_i + T_e)}{m_i T_e}} \right). \tag{2.27}$$

For simulations with ETC, the wall boundary condition must be modified to account for the electron emission and is discussed in Section 2.5.

The fluid governing equations given in Equation 2.14 can be augmented to model electric field effects by including the following source terms in the conservation of

momentum and energy equations [107, 108, 109, 110],

$$\frac{\partial \mathbf{Q}}{\partial t} + \nabla \cdot (\mathbf{F} + \mathbf{F}_v) = \mathbf{S} + \mathbf{S}_E \tag{2.28}$$

$$\mathbf{S}_E = \begin{pmatrix} 0 \\ \vdots \\ 0 \\ \sum_s e n_s c_s \mathbf{E} \\ \vec{j} \cdot \mathbf{E} \\ \vec{j} \cdot \mathbf{E} \end{pmatrix}.$$

These additional source terms account for the Lorentz force and Joule heating caused by the electric forces. Given the importance the electric field can have on understanding ETC, the accuracy of the electric field modeling and assumptions will be verified in future work by solving the Navier-Stokes equations coupled to Maxwell's equations using an algorithm similar to the one developed in Ref. [109].

2.3.1 Forced diffusion

The presence of an electric field will affect how charged species diffuse throughout the flowfield. Without an electric field, the diffusive fluxes are only dependent on the species gradients,

$$\mathbf{J}_s = -\rho D_s \nabla Y_s + \mathbf{J}_s^{SM}, \tag{2.29}$$

where D_s is the diffusion coefficient of species s and Y_s is the mass fraction of species s. The $\vec{J}_s^{SM}$ term appears due to a Stefan-Maxwell treatment to ensure mass conservation [111]. However, the electric field will cause the charged species (e.g. ions and electrons) to drift, impacting the diffusion of charged species [112]. The diffusive fluxes for charged species are modified to account for the drift velocity induced by

the electric field called *forced diffusion*,

$$\mathbf{J}_s = -\rho D_s \nabla Y_s + \mathbf{J}_{fd,s} + \mathbf{J}_s^{SM} \tag{2.30a}$$

$$\mathbf{J}_{fd,s} = \rho \mathbf{u}_d Y_i c_i \tag{2.30b}$$

where c_i is the charge number (1 for ions) and $\mathbf{u}_d$ is the drift velocity. The drift velocity is calculated in terms of the ion drift-diffusion approximation [111],

$$\mathbf{u}_{d,s} = \Big(c_s K_s - \sum_j c_j K_j Y_j\Big)\mathbf{E}, \tag{2.31}$$

where K_s is the ion mobility of species s. The ion mobility is approximated by the polarization limit model [113] and Blanc's law [114],

$$K_{s,j} = \frac{13.853 \cdot 10^{-4}}{\sqrt{P_j \mu_{s,j}}} \quad [\mathrm{m}^2/\mathrm{V/s}] \tag{2.32a}$$

$$\frac{1}{K_s} = \sum_j \frac{Y_j}{K_{s,j}} \tag{2.32b}$$

where P_j is the polarizability [96] of species j and $\mu_{s,j}$ is the reduced mass of species s and j. This is only an approximation because the model assumes the ion mobility is independent of temperature whereas experiments show positive temperature dependence for air ions [115]. Future work will be reserved for determining the mobility more accurately, which can be done by solving the complete Langevin equation or by simplifying this equation with the elastic sphere limit [116]. For electrons, the forced diffusion contribution is,

$$\mathbf{J}_{fd,e} = \rho K_e Y_e \mathbf{E}, \tag{2.33}$$

where the electron mobility can be approximated by the Einstein Relation:

$$K_e = \frac{e D_e}{k_B T_e}. \tag{2.34}$$

2.3.2 Schottky effect

The electric field at the wall can decrease the energy barrier that the emitted electrons must overcome at the surface, which effectively reduces the work function, known as the Schottky effect [112],

$$W_{F,c} = W_F - \sqrt{\frac{e^3 \mathbf{E}_w}{4\pi\epsilon_0}}. \tag{2.35}$$

The effect requires a large electric field at the surface to be able to significantly enhance the level of emission by lowering the work function and is small for the moderate electric fields experienced by ETC [112].

2.4 Magnetic field

An ionized flow is not only subject to electric fields but also magnetic fields. There have been multiple studies investigating the magnetohydrodynamic effect from inducing a magnetic field on the ionized flow during hypersonic flight [98, 117, 118, 119, 120, 121]. This work does not intentionally induce a magnetic field to the flow. However, with ETC, there is a current of electrons from the surface, which can induce a magnetic field as shown by Ampere's law [122, 123],

$$\nabla \times \mathbf{B} = \mu_0 J_e + \mu_0 \epsilon_0 \frac{\partial \mathbf{E}}{\partial t}. \tag{2.36}$$

This work assumes steady-state so Equation 2.36 becomes,

$$\nabla \times \mathbf{B} = \mu_0 J_e, \tag{2.37}$$

that can be approximated by using the characteristic length of the emission surface (i.e. electrode),

$$\mathbf{B} \approx L\mu_0 J_e. \tag{2.38}$$

Figure 2.5 presents the estimated magnetic field induced by the electron emission from the surface for different characteristic lengths of the emitter surface. The estimated magnetic field induced by electron emission reaches values on the order of 100 Teslas for the condition with a large emitter surface, surface temperature, and small work function, which is impossibly large.[11] However, larger surfaces (i.e. leading edge radii) correspond to lower surface temperatures (Equation 1.2) so the actual magnetic field induced during ETC will be significantly lower. Also, the emission current density shown in Figure 2.5 is determined using Equation 2.4, which is the maximum amount of emission possible (i.e. saturation current). As will be shown in Chapter III the actual emission current density is much smaller.

The Hall parameter is utilized to characterize how magnetized the plasma is, specifically the electrons, and is defined as,

$$\Omega_e = \frac{\omega_e}{\nu_m}, \tag{2.39}$$

where ω_e is the gyro frequency of the electrons and ν_m is the electron-neutral particle momentum transfer collision frequency, which can be estimated as a function of pressure for air [112, 124]:

$$\omega_e = \frac{e|\mathbf{B}|}{m_e}, \tag{2.40}$$

[11]The largest magnetic field produced in a lab is approximately 15 Tesla (see National Higher Magnetic Field Laboratory).

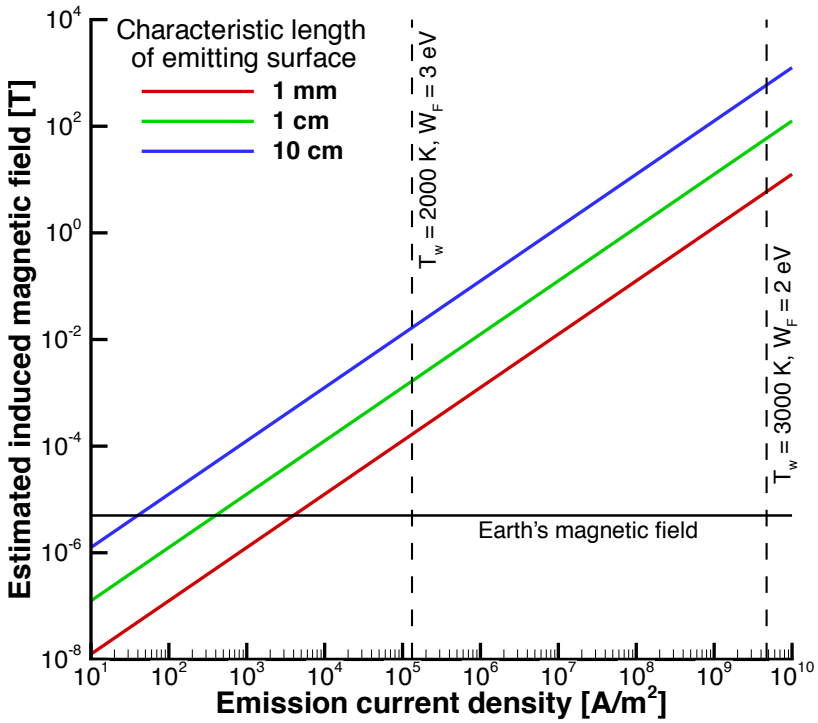

Figure 2.5: Estimated magnetic field induced by electron emission from a vehicle surface with ETC.

$$\frac{\nu_m}{p} = 5.2 \cdot 10^{11} \quad [\mathrm{s^{-1}\ Pa^{-1}}]. \tag{2.41}$$

If the Hall parameter is much greater than unity, the electrons are magnetized and magnetic field effects should be accounted for.[12] If the Hall parameter is much less than unity, the electrons are unmagnetized and magnetic field effects can be neglected. Figure 2.6 shows the resulting Hall parameter as a function of emission current density, pressure, and characteristic length of emission surface typical of conditions for ETC. The Hall parameter is always less than unity and mostly significantly less than unity except for low pressure (i.e. 0.01 atm) and large emission surface (i.e. 10 cm) at high levels of emission. Space-charge limits will bound the level of emission from the surface as discussed in Section 2.5, so these extreme levels of emission will not be realized. Given that the estimated Hall parameter is much less than unity, the

[12] At least for the electrons. It takes a stronger magnetic field to magnetize the ions due to their larger mass.

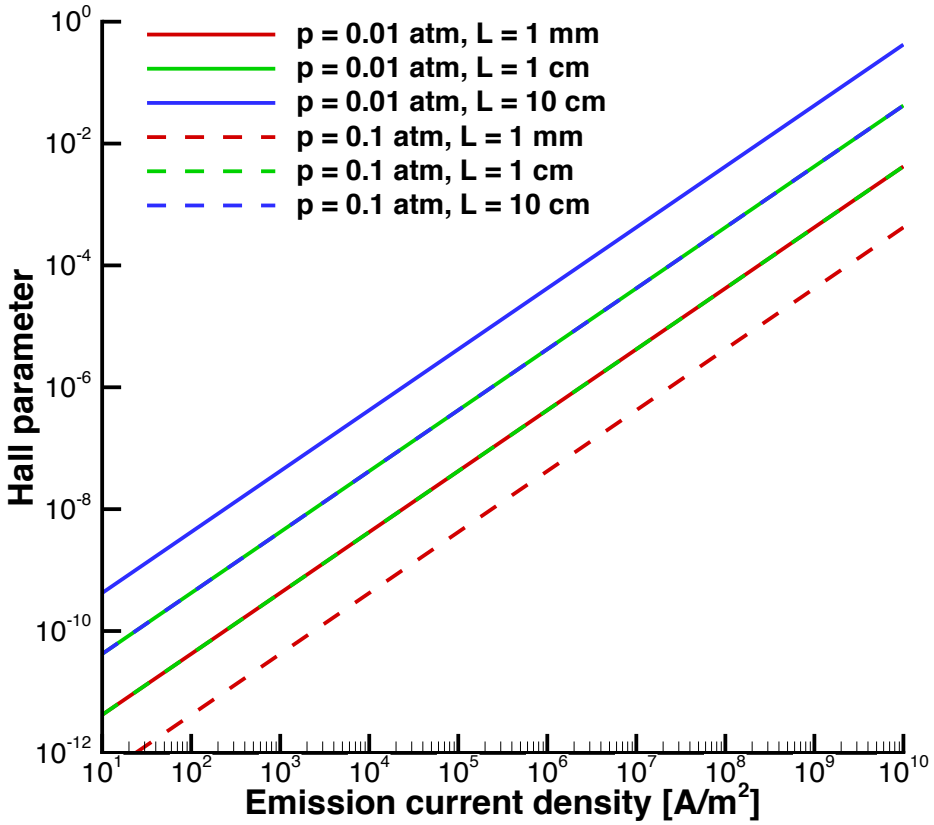

Figure 2.6: Hall parameter as a function of emission current density, pressure, and characteristic length of emission surface.

assumption to neglect the magnetic field effects is appropriate.

2.5 Plasma sheath

A plasma sheath forms near the wall, which is a non-neutral region between the quasineutral flowfield and the wall. The sheath typically occurs because the electrons are much more mobile than the ions due to their mass difference ($m_e \ll m_i$). This higher mobility of electrons leads to more electrons leaving this region than ions, leaving the region positively charged, which generates a negative potential difference between the flowfield and the wall. The length scale of this non-neutral region is on

the order of the Debye length:

$$\lambda_D = \sqrt{\frac{\epsilon_0 k_B T_e}{e^2 n_e}}. \tag{2.42}$$

Another important sheath parameter is the sheath collisionality, which is proportional to the number of collisions that occur within the sheath,

$$\tau = \frac{\lambda_D}{\lambda_{i,e}}, \tag{2.43}$$

where $\lambda_{i,e}$ is the ion-neutral and electron-neutral mean free paths,

$$\lambda_i = \frac{1}{(n_i + n_{neut})Q_i} \tag{2.44a}$$

$$\lambda_e = \frac{1}{(n_e + n_{neut})Q_e} \tag{2.44b}$$

where Q_i and Q_e are the collisional cross sections of the ions and electrons. The collisional cross section of electron-neutral collision is approximately $5 \cdot 10^{-20}$ m^2 [125] and the collisional cross section of the ion-neutral collisions is approximately $1 \cdot 10^{-19}$ m^2 [126]. For the cases of interest, the Debye lengths are significantly smaller than the ion-neutral and electron-neutral mean free paths,[13] which leads to the collisionality of the sheath being smaller than one. If $\tau \ll 1$, the sheath can be treated as collisionless [127]. For this work, the sheath is assumed to be collisionless, although there could be some collisions within the sheath since the collisionality is not *much smaller* than one. A previous study showed that the sheath width is four to ten times the Debye length so τ can be on order of one [128], and thus collisions could occur within the sheath impacting the sheath physics. Collisions within the sheath can impact the level of emission [127, 129, 130] and will be investigated in future work.

A collisionless sheath simplifies this work because it is difficult to resolve the

[13] Presented in Section 3.4.

sheath in the computational mesh because it would require many more cells to capture the sheath physics due to its small length scale as well as higher fidelity plasma modeling. Instead, an analytical model can be used to model the sheath physics and the sheath edge will act as the wall boundary condition in the CFD code similar to the schematic shown in Figure 2.7. The boundary conditions for the electric field modeling, discussed in Section 2.2, will be set at the sheath edge (i.e. the interface between the flowfield and plasma sheath). Richardson's temperature saturated current (Equation 2.4) determines the emitted current from the surface. Space-charge limits discussed in Section 2.5.1 will return a portion of the emitted electrons back to the surface before escaping the plasma sheath. The remaining current will escape the plasma sheath and be emitted into the flowfield. This is the current that is used in the ETC heat flux away from the surface (Equation 2.3). The sheath edge is also the *wall* potential the flowfield experiences. The sheath edge will be used as the computational boundary condition and analytical models discussed in Section 2.5.2 will be used to represent the plasma sheath physics.

2.5.1 Space-charge limit

An important aspect that was not considered in Richardson's equation (Equation 2.4) is the effect of space-charge limits [131, 132]. Richardson assumed that the emission from the surface experiences ideal conditions: emitted electrons see no retarding electric field at the surface, are not reflected back to the surface through collisions, nor see a virtual cathode created by space-charge limits. Space-charge-limited emission occurs when there is a significant electron cloud in front of the emissive surface, which creates a virtual cathode that forces the electrons back to the surface. At the point at which the emission reaches this space-charge limit, there will be no virtual cathode and the electric field at the solid surface will be zero. As emission is increased, the virtual cathode will move off the surface and become larger in voltage

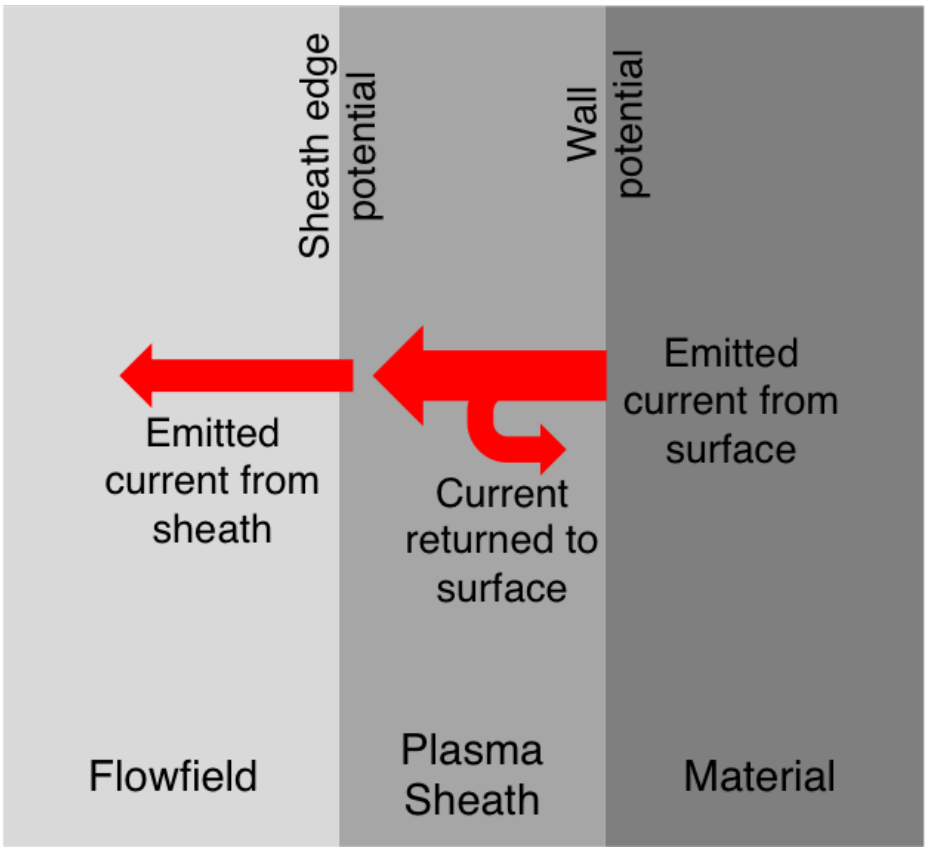

Figure 2.7: Plasma sheath schematic. The plasma sheath connects the material to the quasineutral flowfield.

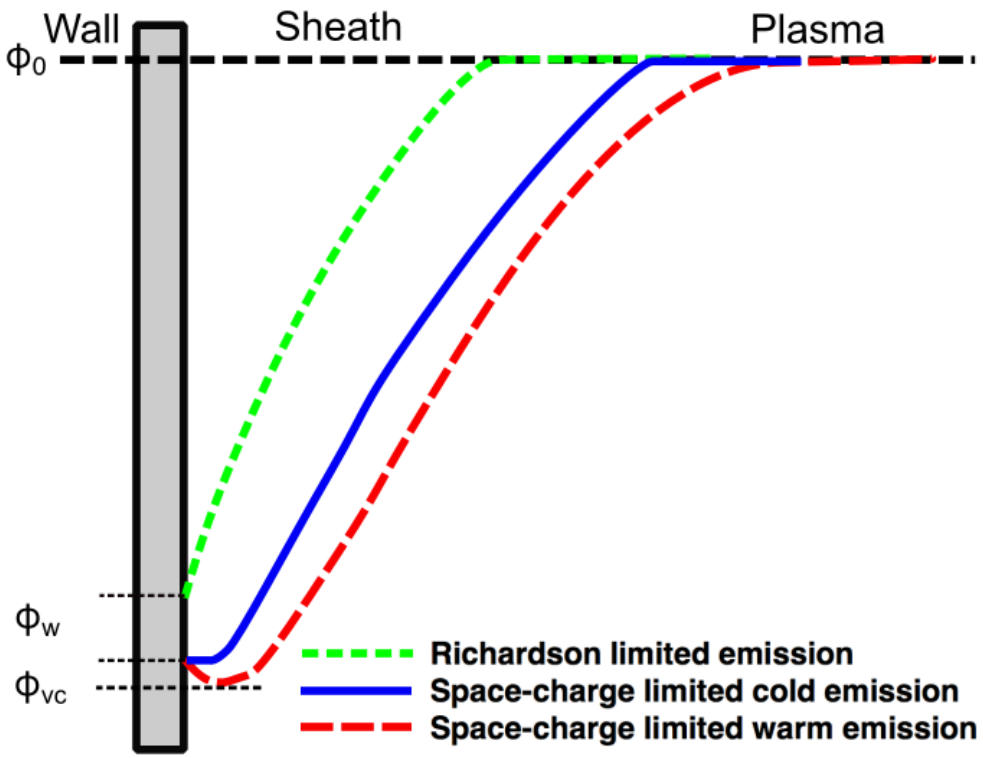

Figure 2.8: Sheath schematic where ϕ is the electric potential.

to enforce the space-charge limit. A schematic of the sheath is shown in Fig. 2.8. If the emission is not space-charge limited, the potential within the sheath will be similar to the green curve, where $E_w < 0$ such that plasma electrons are repelled back to the plasma and emitted electrons from the wall accelerate into the plasma. As emission is increased, it will reach the space-charge limit where the electric field is zero at the wall denoted by the blue curve. This type of emission will be referred to as cold emission as the electrons are emitted cold. As emission is further increased, the virtual cathode will move off the wall and create a potential well as denoted by the red curve in Fig. 2.8. This will be referred to as warm emission because the emitted electrons will have a finite temperature. Note that the net electron emission current that flows out of the sheath into the plasma is constant at space-charge limited current. This is why the electron emission is *limited* due to the space charges near the wall surface.

2.5.2 Analytic approaches

Emissive probes has been used for over 90 years to measure plasma properties (e.g. potential, temperature) and have been extensively studied [133]. Emissive probe theory was developed to relate measurable properties to desired plasma properties. Typically, the current was measured from the probe in order to determine the plasma potential and/or temperature. However for ETC, the plasma properties are known via CFD and the level of emission possible in these conditions is unknown.

2.5.2.1 Electrically floating surface

If the emissive surface is treated as an electrically floating surface (i.e. electrically insulated), the net current through the sheath must be zero:

$$J_e = J_{i,f} - J_{e,f}, \tag{2.45}$$

where $J_{i,f}$ and $J_{e,f}$ is the current density of flowfield ions and electrons through the sheath, respectively. Essentially, the amount of electrons that escape the sheath will be limited by the difference between the fluxes of flowfield ions and electrons reaching the sheath edge. Since the flowfield is quasineutral, the level of emission for treating the wall as an electrically floating surface is typically small. Typically, the net charge flow through the sheath edge is zero, so the boundary condition for plasma potential at the sheath edge will be a zero gradient. The wall potential can be approximated using relations provided by Hobbs and Wesson, which assume zero electric field at the surface (i.e. cold emission) [134]:

$$\phi_w \approx \frac{-k_B T_e}{e} \log\left[\frac{1-\Gamma}{\sqrt{\frac{2\pi m_e}{m_i}}}\right], \tag{2.46}$$

where Γ is the ratio of the emission to flowfield ($J_{e,f}$) electron current densities,

$$\Gamma = \frac{J_e}{J_{e,f}}. \tag{2.47}$$

This approximation assumes that the ions arrive at the wall cold and the electrons are emitted with negligible energy (i.e. not warm emission). The flowfield electron current density can be calculated by,

$$J_{e,f} = e n_{e,f} \sqrt{\frac{k_B T_e}{2\pi m_e}} \exp\left(\frac{e\phi_w}{k_B T_e}\right), \tag{2.48}$$

where $n_{e,\mathbf{f}}$ is the number density of flowfield electrons, which is assumed to equal the number density of flowfield electrons at the sheath edge without emission (assuming emission has no effect on $n_{e,f}$). This approximation is good up to Γ_{crit} in which a potential well forms such that a fraction of the emitted electrons return to the wall to maintain the current conservation in the sheath region. These critical values are space charge limited values [134],

$$\Gamma_{crit} = 1 - 8.3\sqrt{\frac{m_e}{m_i}} \tag{2.49a}$$

$$\phi_{w,crit} = \frac{-1.02 k_B T_e}{e}. \tag{2.49b}$$

Writing Eq. 2.45 in terms of Γ:

$$\frac{J_e}{J_{i,f}} = \frac{\Gamma}{1-\Gamma}. \tag{2.50}$$

As expected, emission is limited by both flowfield ions and electrons. The lightest ion commonly found in air is N^+ and the heaviest is O_2^+ which will lead to Γ_{crit} being between 0.94 and 0.97, which leads to the level of emission from the surface being at most 0.97 times the flowfield electron current. Since the critical level of emission is

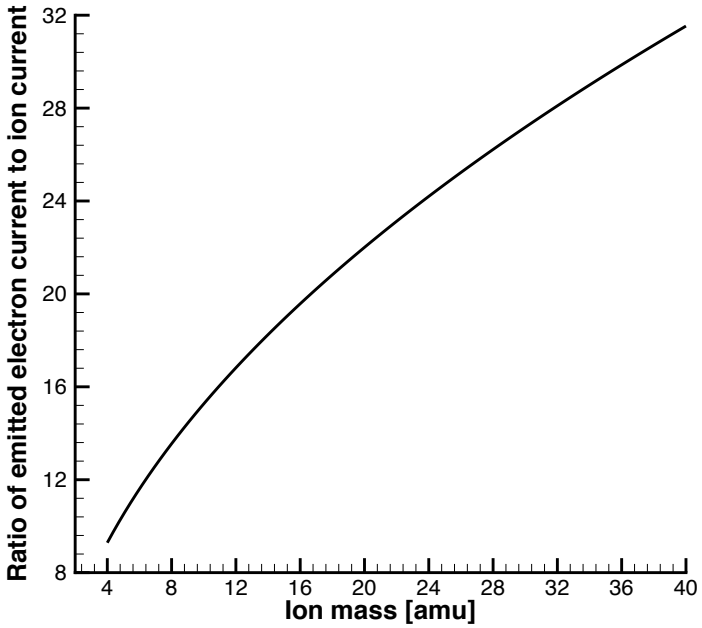

Figure 2.9: The critical ratio of emitted electron current to ion current (Eq. 2.50) versus different ion masses.

dependent on the mass of the ions, Equation 2.50 is plotted for different values of air ion species in Figure 2.9 using Γ_{crit}.

2.5.2.2 Negatively biased surface

If the surface is not floating electrically and is negatively biased, a net current is permissible through the sheath edge. A surface such as this would occur if the emitted electrons reattach downstream on the vehicle and travel back to the emitter surface completing the circuit as shown in the schematic in Fig. 2.10. The electrons, denoted by the red dots, are emitted from the leading edge, which is susceptible to high surface temperatures due to its sharp radius, through thermionic emission and carries energy downstream where it deposits the energy as heat on the cooler aft-body of the vehicle. The red arrow denotes the electrical current being conducted back through the vehicle to the leading edge to complete the circuit. In practice, this could be done by having a battery in the circuit and within the vehicle to help drive the current. This work focuses on the leading edge (emitter region) and assumes

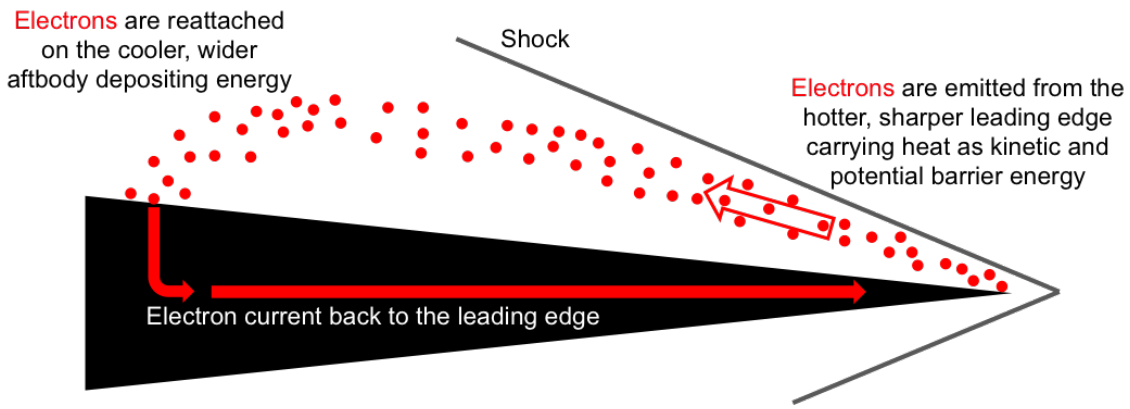

Figure 2.10: Electron Transpiration Cooling schematic.

that the surface can be biased relative to the quasineutral flow to a desired potential, whereas in reality the potential would be set based on the operating conditions.

Electrons being emitted from the leading edge of a hypersonic vehicle (cathode) and reattaching downstream (anode) is analogous to a double emissive probe. Similar to an electrically floating surface, this type of surface is also susceptible to space-charge limits. Ye and Takamura [135] derived an expression from Poisson's equation for space-charge limited current through the sheath for the case with zero electric field at the surface and assuming that the ions arrive cold from the plasma and electrons are emitted cold from the surface:

$$\Gamma = \frac{J_{e,sc}}{J_{f,i}} = \frac{G\sqrt{-\pi\Phi_w}}{1+G}\sqrt{\frac{2m_i}{\pi m_e}}, \tag{2.51}$$

$$\Phi_w = \frac{e(\phi_w - \phi_0)}{T_e}, \tag{2.52}$$

where Φ_w is the normalized sheath potential and Γ is now the ratio of the electron

emission current to the ion saturation current, $J_{f,i}$, defined by,

$$J_i = en_i C_s, \tag{2.53}$$

where C_s is the ion acoustic speed for cold ions,

$$C_s = \sqrt{\frac{k_B T_e}{m_i}}. \tag{2.54}$$

G is a function of the normalized sheath potential and can be determined by solving the following equations, which were derived from Poisson's equation,

$$G = \frac{-\beta_1 + \sqrt{\beta_1^2 - 4\beta_0\beta_2}}{2\beta_2} \tag{2.55a}$$

$$\beta_0 = -4\Phi_w^2 - 2\Phi_w(F^2 - 2F) \tag{2.55b}$$

$$\beta_1 = 4(-2F - 1)\Phi_w^2 + 8F\Phi_w - F^2 \tag{2.55c}$$

$$\beta_2 = 4\Phi_w^2 - 8\Phi_w^3 \tag{2.55d}$$

$$F = \exp(\Phi_w) - 1 \tag{2.55e}$$

This leads to the space-charge limited cold emission current equaling,

$$J_{e,sc} = en_i \frac{G\sqrt{-\Phi_w}}{1+G}\sqrt{\frac{2k_B T_e}{m_e}}. \tag{2.56}$$

If this current is less than the temperature saturated current determined by Equation 2.4 ($J_{e,sc} < J_{e,s}$), the emission is space-charge limited and ETC will be determined using Equation 2.56. This theory has been compared to a 1-D PIC simulation and a qualitative agreement is shown [136]. Equation 2.56 reaches a limit as the Φ_w

approaches negative infinity. Since G is a function of Φ_w, the limit is

$$\lim_{\Phi_w \to -\infty} \left(\frac{G\sqrt{-\Phi_w}}{1+G} \right) = \frac{\sqrt{2}}{2} \tag{2.57a}$$

$$\lim_{\Phi_w \to -\infty} J_{e,sc} = en_i \sqrt{\frac{k_B T_e}{m_e}}. \tag{2.57b}$$

Although high negative voltages may be difficult to realize or not ideal (e.g. arc discharges) in a hypersonic environment, this limit of the space-charge limited emission is still useful in this analysis. For example, it can be used to to determine if the saturated emission current densities predicted by Richardson in ideal conditions (Eq. 2.4) can even theoretically be obtained even if the surface could be biased significantly or if the emission will be space-charge limited no matter what the voltage bias of the surface is.

If the emitted electrons are not emitted cold and have a finite temperature, Equation 2.51, primarily G, can be modified to account for this [136]:

$$\Gamma = \frac{J_e}{J_{f,i}} = \frac{G_* \sqrt{-\pi \Phi_{vc}}}{1 + A \cdot G_*} \sqrt{\frac{2m_i}{\pi m_e}}, \tag{2.58}$$

where the normalized potential is now in reference to the virtual cathode potential instead of the wall potential (see Figure 2.8),

$$\Phi_{vc} = \frac{e(\phi_{vc} - \phi_0)}{T_e}. \tag{2.59}$$

G_* is derived from Poisson's equation as detailed in Ref. [136] and is a function of the normalized sheath edge potential and the ratio of emitted electron temperature

to electron temperature at the sheath edge,

$$\beta_3 G_*^3 + \beta_2 G_*^2 + \beta_1 G_* + \beta_0 = 0 \tag{2.60a}$$

$$\beta_3 = HF^2 - 2A^2F + 2\Phi_{vc}A^3 \tag{2.60b}$$

$$\beta_2 = F^2 + 2HF[\exp(\Phi_{vc}) - 1] - 2A^2[\exp(\Phi_{vc}) - 1] + 4AF + 6\Phi_{vc}A^2 \tag{2.60c}$$

$$\beta_1 = 2(F - 2A)[\exp(\Phi_{vc}) - 1] + H[\exp(\Phi_{vc}) - 1]^2 - 2F + 6\Phi_{vc}A \tag{2.60d}$$

$$\beta_0 = [\exp(\Phi_{vc}) - 1]^2 - 2[\exp(\Phi_{vc}) - 1] + 2\Phi_{vc} \tag{2.60e}$$

$$A = \sqrt{\frac{-\pi\Phi_{vc}}{\gamma}}\,\mathrm{erfc}\left(\sqrt{\frac{\Phi_{vc}}{\gamma}}\right)\exp\left(\frac{\Phi_{vc}}{\gamma}\right) \tag{2.60f}$$

$$H = \frac{A - 1}{\gamma} \tag{2.60g}$$

$$F = -\gamma A + 2\Phi_{vc} + \sqrt{-\pi\gamma\Phi_{vc}} \tag{2.60h}$$

where γ is the ratio of emitted electron temperature to electron temperature at the sheath edge,

$$\gamma = \frac{T_{e,w}}{T_e}. \tag{2.61}$$

This leads to the space-charge limited warm emission current equaling,

$$J_{e,sc} = en_i \frac{G^*\sqrt{-\Phi_w}}{1 + A \cdot G^*}\sqrt{\frac{2k_B T_e}{m_e}}. \tag{2.62}$$

The formation of the plasma sheath at the surface requires that the ions be accelerated up to speeds equal or greater to Mach 1 at the sheath edge, an inequality referred to as the Bohm criterion [137]:

$$v_i \geq C_s. \tag{2.63}$$

The previous theory assumes that the ion velocity is equal to Mach 1, but the theory

can be extended to account for supersonic ion velocities at the sheath edge:

$$v_i = \chi C_s, \tag{2.64}$$

where χ is greater or equal to unity. Modification of the theory to account for alpha was important to validate the plasma sheath simulation results using the method discussed in Section 2.5.4, as the collisionless sheath simulation allows ion velocity to be higher than ion acoustic speed. In the LeMANS simulation, the original Takamura and Ye theory is used assuming that collisionality is sufficient in the presheath and plasma so that $\chi = 1$ will be retained in the actual physics. The speed at which the ions enter the sheath can be determined by [138, 139],

$$v_i = C_s\sqrt{1 + \frac{\pi\lambda_D}{2\lambda_i}} \tag{2.65a}$$

$$\chi = 1 + \frac{\pi\lambda_D}{2\lambda_i}. \tag{2.65b}$$

Since the Debye length is much less than the mean free path of the ions for the cases considered[14], the ions will essentially enter the sheath at the speed of the ion acoustic speed. Details of the extension can be found in Appendix B but the only term modified is G and the ion saturation current,

$$G^{**} = f(\Phi_{vc}, \gamma, \chi) \tag{2.66}$$

$$J_i = en_i\chi C_s. \tag{2.67}$$

The effect of biasing the surface on the charged flowfield species convective heating rate is expected to be small due to the level of flowfield ionization being less than

[14]Presented in Section 3.4.

1% for the cases of interest and was not accounted for in previous ETC studies [140]. However, accounting for the bias in the heat transfer balance at the surface is still important to be able to truly understand the cooling benefits of ETC for leading edges. The heat transfer from the charged particles in the flowfield (i.e. plasma) to the surface can be written as [141],

$$q_{f,i} = e n_i v_i \left(I_{ioniz} + \phi_w + \frac{m_i v_i^2}{2e} \right) \tag{2.68a}$$

$$q_{f,e} = 2 k_B T_e n_{e,f} \exp\left(\frac{-e\phi_w}{k_B T_e} \right) \sqrt{\frac{k_B T_e}{2\pi m_e}}, \tag{2.68b}$$

where I_{ioniz} is the ionization potential of the ions. Some of the terms in Equation (2.68a) have already been accounted for in LeMANS. For example, a fully catalytic wall is used in LeMANS which accounts for the recombination energy (I_{ioniz} term) as well as the kinetic energy of the ions ($m_i v_i^2/2e$ term) in the convective heating calculations. Since the flowfield is quasi-neutral ($n_{i,f} = n_{e,f}$), a comparison of the effect the biased wall has on the flowfield electrons can be made where the terms already accounted for in LeMANS are removed,

$$\frac{q_{f,e}}{q_{f,i}} = \frac{2 k_B T_e}{e\phi_w} \exp\left(\frac{-e\phi_w}{k_B T_e} \right) \sqrt{\frac{m_e}{m_i}}. \tag{2.69}$$

This equation is plotted in Figure 2.11 and shows that sheath heating from the flowfield electrons is negligible compared to the sheath heating from the flowfield ions ($q_{f,e} \ll q_{f,i}$). For this reason, the effect of the biased wall on the heating from the flowfield electrons will not be accounted for in the CFD simulations. However, Equation 2.3 is modified to account for the effect of the biased surface on the flowfield ions as the potential will cause them to *accelerate* into the wall,

$$q_{ETC} = J_e \left(W_F + \frac{2 k_B T_w}{e} \right) - e n_i v_i \phi_w. \tag{2.70}$$

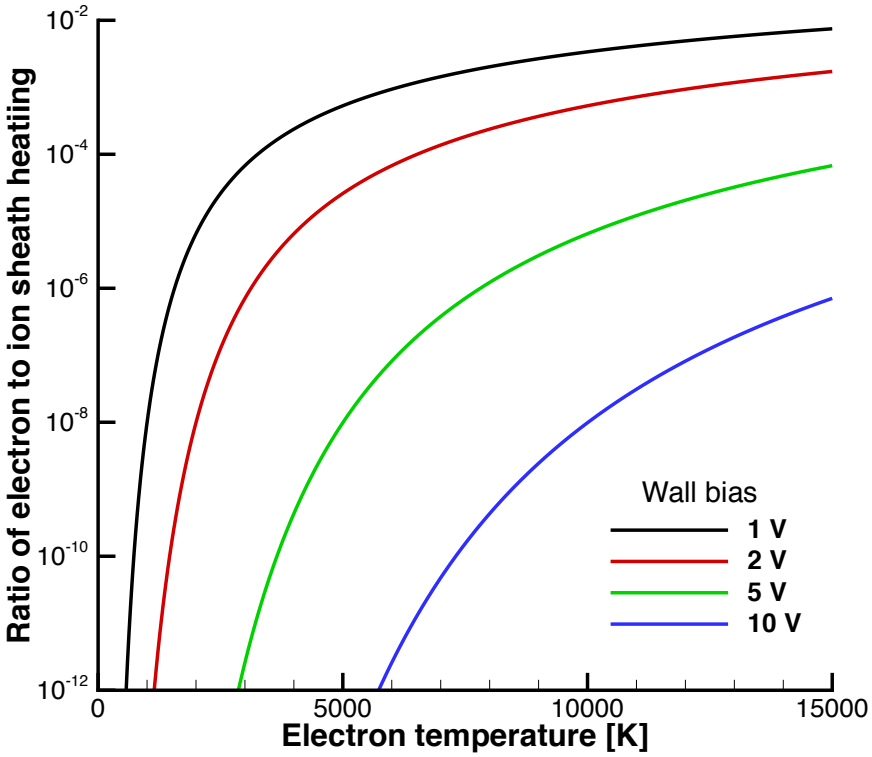

Figure 2.11: Ratio of electron to ion sheath heating (Eq. 2.69).

The biased wall will also have an effect on the emitted electrons as it will *accelerate* the electrons into the plasma increasing their energy,

$$q_{e,e} = \phi_w J_e. \tag{2.71}$$

However, this energy flux occurs at the sheath edge and not at the wall so it will not affect Equation 2.70 but *heat* the flowfield. Also, because the electron-electron energy transfer collision frequency is much larger than that for the electron-heavy particles (i.e. neutrals, ions), the energy the emitted electrons gain from the sheath bias is only transferred to the flowfield electrons [21, 88, 142]. On average, it takes approximately $m_h/(2m_e)$ more collisions for an electron to transfer its energy to a heavy particle (m_h) than for the energy exchange of two particles of the same mass [143]. Since the electron translational energy mode is assumed to be in thermal equilibrium with the vibrational-electronic energy mode and the electron temperature is not explicitly

solved for, it is difficult to account for this increase of flowfield electron energy in the current modeling framework precisely.[15] This work will assume that the emitted electrons transfer energy to the flowfield electrons at a significant enough distance away from the emitting surface, so that the heat transfer balance is not affected at the leading edge due to this energy increase of emitted electrons. This is a strong assumption and experiments are scheduled to investigate how the emitted electrons act in the hypersonic boundary layer. The adverse assumption would assume that *all* the energy gained by the electrons in the plasma sheath returns to the surface and directly affects Equation 2.70:

$$q_{ETC} = J_e\left(W_F + \frac{2k_B T_w}{e} - \phi_w\right) - en_i v_i \phi_w. \tag{2.72}$$

It is to be noted that the ion sheath heating term ($en_i v_i \phi_w$) is negligible compared to the electron emission terms for the conditions of interest as detailed in Section 3.6. However, under this assumption, in order to the vehicle to be cooled,

$$\left(W_F + \frac{2k_B T_w}{e}\right) > \phi_w. \tag{2.73}$$

This relationship is plotted in Figure 2.12, which shows that if the energy gained by the emitted electrons in the sheath is returned entirely to the wall, the biased sheath potential must essentially be smaller than the work function of the material in order for the surface to be cooled. Figure 2.12 also highlights that if the level of emission (J_e) is equal, materials with higher work functions carry more energy away from the vehicle.[16]

Future work is reserved for characterizing how this increase in emitted electron

[15] This energy could be included in $\dot{w}_{ve}$ but it is unclear how far away from the surface this source occurs.

[16] Typically, materials with lower work functions have a higher level of emission (Eq. 2.3) but space-charge limits can inhibit level of emission.

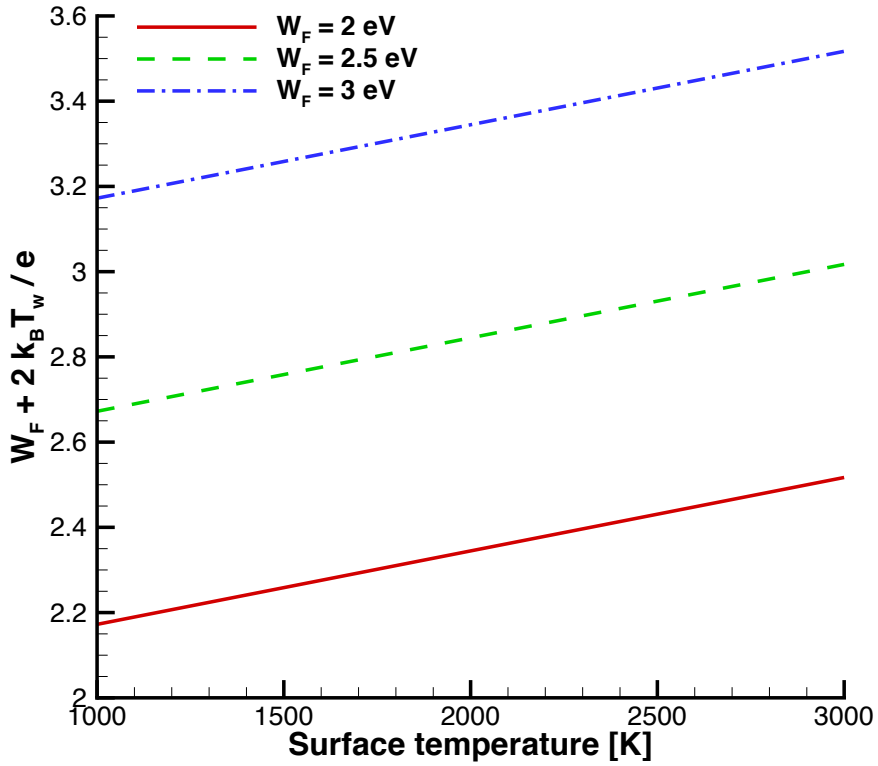

Figure 2.12: Emitted electron contribution to cooling rate of Eq. 2.72.

energy affects the heat transfer at the wall. This includes solving for the electron temperature in the flowfield explicitly similar to the approach in Ref. [144] and accounting for Equation 2.71 in the boundary condition similar to the approach in Ref. [142] to investigate this phenomenon from a modeling approach. Nevertheless, this increase in electron energy is used to approximate the electron temperature at the sheath edge in Section 2.5.3, which is then used in the sheath relations.

The net current provided by the biased surface leads to the plasma not being quasineutral at the sheath edge. There is a thin region that forms between the sheath edge and the quasineutral flowfield, called the presheath. This region forms to provide the ions with enough energy (i.e. velocity) to meet the Bohm criterion [112]. The potential at the sheath edge is usually on the order of a few electron temperatures

[112, 145] and can be approximated by [142],

$$\phi = \frac{k_B T_e}{e} \ln\left(1 - \frac{J_e}{e n_i \sqrt{\frac{2e\phi_w}{m_e}}}\right). \tag{2.74}$$

This potential will be used as the *wall* boundary conditions in the CFD simulations for cases with ETC.

2.5.3 Electron temperature approximation

The electron temperature is not solved for explicitly in LeMANS due to the increase in computational cost. Since the relations only need the electron temperature at the sheath edge, an approximation is developed to calculate the electron temperature there. The electron temperature at the sheath edge is determined by the emitted electrons that are accelerated through the potential of the sheath to reach the sheath edge and the flowfield electrons resulting from the ionization of the hypersonic flow,

$$T_e = \frac{n_{e,e}}{n_{e,t}} T_{e,e} + \frac{n_{e,f}}{n_{e,t}} T_{e,f}. \tag{2.75}$$

The electron temperature is determined from the mean electron energy, which is calculated by applying a biased Maxwellian velocity distribution function to both the emitted and flowfield electrons. More details of this derivation can be found in Appendix A.

2.5.4 Direct-Kinectic method

Numerical simulations are also performed on the collisionless sheath region near the surface using a grid-based direct kinetic method (DK) solver that was developed at the University of Michigan [128]. DK methods are an alternative, deterministic approach to particle-based methods for plasma simulations. A grid-based kinetic method employs discretized phase space in which the kinetic equations are solved

directly. The governing equation is the Boltzmann equation:

$$\frac{\partial f}{\partial t} + \mathbf{v} \cdot \frac{\partial f}{\partial \mathbf{x}} + \mathbf{a} \cdot \frac{\partial f}{\partial \mathbf{v}} = S, \tag{2.76}$$

where f is the velocity distribution function (VDF), t is the time, $\mathbf{v}$ is the velocity, $\mathbf{x}$ is the physical space, $\mathbf{a}$ is the acceleration, and S is the collisional source term. The acceleration can be written as,

$$\mathbf{a} = \frac{e(\mathbf{E} + \mathbf{v} \times \mathbf{B})}{m}. \tag{2.77}$$

Since this work assumes a collisionless sheath, the collisional source term is zero and Equation 2.76 becomes the collisionless Boltzmann equation, which is often referred to as the Vlasov equation.

The collisionless DK simulation solves for the Vlasov equation. Strang's time splitting is used for time integration. A 2nd order finite-volume method with modified Arora-Roe scheme is used to preserve positivity of the VDFs in the simulation. Poisson's equation is solved for the potential with two Dirichlet conditions: on the wall and at the sheath edge. The boundary conditions for the VDFs are assumed to be half-Maxwellian for the injected particles with a temperature for each species. An outflow boundary condition is used for the particles that leave the computational domain. The velocity, position, time, and potential are normalized by the ion acoustic speed, Debye length, ion plasma frequency, and electron temperature, respectively, in the simulation. More details of the numerical approach can be found in Chapter II of Ref. [128].

2.6 Solid material

The flow of energy into the solid material of the vehicle is modeled using a material response solver developed at the University of Michigan called MOPAR [146]. The numerical code is capable of simulating multidimensional thermal and structural response of materials exposed to hypersonic flows. The thermal portion of the code can model materials with temperature-dependent, anisotropic properties and the heat fluxes are computed using Fourier's law. MOPAR is strongly coupled with LeMANS in order to study quasi-static aerothermal and aerothermoelastic problems that arise in hypersonic flows such as ablation and in-depth surface conduction. The thermal response of the material is calculated by solving the heat equation written for a control volume, Ω, as,

$$\int_{\partial\Omega} q_i \hat{n}_i d\partial\Omega + \frac{d}{dt}\int_{\Omega} \rho\tilde{e} d\Omega = \int_{\Omega} S d\Omega, \tag{2.78}$$

where q_i is the heat flux in the i^{th} direction, $\hat{n}_i$ is the normal vector of the control surface, ρ is the material density, $\tilde{e}$ is the internal specific energy of the material, and S is the optional source term. The material response solver is discussed in detail in Refs. [146, 147, 148].

The general coupling procedure for MOPAR is discussed in Refs. [146, 148] but the procedure used for coupling with ETC is simpler due to no surface change (i.e. moving mesh) caused by ablation and only investigating one trajectory point at a time. The ETC coupling procedure is as follows:

1. LeMANS converges to a solution without ETC or in-depth surface conduction.
2. ETC is *turned on* and LeMANS converges to a new solution.
   (a) The ETC heating rate is subtracted from the convective rate ($\breve{q} = q_{conv} - q_{ETC}$).

3. This effective heating rate ($\check{q}$) is sent to MOPAR.

    (a) MOPAR determines the surface temperature based on the effective heating rate ($\check{q}$) while also accounting for radiative cooling.

4. MOPAR sends LeMANS the updated surface temperature.

    (a) LeMANS calculates the updated convective and ETC heating rates based on updated surface temperature.

5. Loop to Step (3) and repeat until convergence.

This framework can be extended to include ETC throughout an entire flight trajectory, which is reserved for future work.

2.7 Conclusion

This chapter detailed the modeling approach for investigating ETC. The discussion included the heat transfer theory involved, which detailed the energy carried by emitted electrons. If the levels of emission are as predicted by Richardson's current, the cooling power of ETC shows much potential and is even more effective than radiative cooling, which is currently the most effective way to cool leading edges of hypersonic vehicles. The conditions of interest were also discussed in this chapter, using the flight of the X-43A as the baseline case. The flowfield modeling was discussed in detail in this chapter. This included motivation for using CFD for the numerical simulations and showed that at higher altitudes, the validity of CFD decreases. The conservation equations were detailed as well as the updated boundary conditions to account for electron emission. The electric field modeling was detailed including forced diffusion and the Schottky effect and justification was provided for neglecting the magnetic field. Plasma sheath physics were also explored in this chapter in order to better estimate the level of emission and how space-charge limits can affect ETC.

The material response solver was also described in this chapter, which models the in-depth surface conduction. ETC will be investigated using this modeling approach to better understand the benefits and challenges of using it during hypersonic flight.

CHAPTER III

Numerical Results

3.1 Introduction

Chapter II presented the numerical modeling approach used to investigate the effects of ETC on leading edges of hypersonic vehicles. This approach was implemented into LeMANS and this chapter presents the numerical results of a detailed investigation of ETC for conditions typical of hypersonic flight.[1] First, the test cases are outlined that are applicable to conditions experienced at the leading edge of a hypersonic vehicle, which include the vehicle geometry, flight conditions, and material properties. The features of the flowfield and surface for cases without ETC are presented, which are used to justify assumptions made in the modeling approach (e.g. weakly ionized flow, collisionless sheath). The numerical results for the effects of ETC follow which are separated into different sections based on varying fidelity of modeling physics and surface types. The first approach is to model ETC using temperature saturated emission and to neglect space-charge-limits. The subsequent approaches account for space-charge limits for both a electrically floating surface and a non-floating surface (i.e. negatively biased surface). These investigations include looking at how different parameters (e.g. leading edge radii, work function) affect

[1]It may be of interest to the reader, to read Chapter IV first where the numerical method is assessed and verified to some extent using past experimental data.

ETC performance during hypersonic flight. Two additional investigations are then examined, which include the effect of electric field and in-depth material conduction on ETC. Finally, the chapter concludes by taking a step back from CFD and assessing the plasma sheath theory that was developed in Chapter II using a 1D direct kinetic plasma sheath solver.

3.2 Test case description

In order to investigate how ETC performs on a sharp leading edge in a hypersonic environment, an applicable test case must be determined and characterized. As discussed in the previous chapters, many different parameters can affect both hypersonic flight and ETC, which will be divided into three categories: 1) vehicle geometry, 2) freestream conditions, and 3) material properties.

3.2.1 Geometry

The geometry of the test case considered is representative of a 2D leading edge of a hypersonic vehicle and is shown in Figure 3.1. The baseline leading edge nose radius is 1.0 cm with a wedge angle of 5.0 deg, which was the geometry investigated in previous ETC studies [110, 140]. However, a smaller leading edge radius of 1 mm and a larger leading edge radius of 10 cm are also investigated in order to determine the effects of leading edge shape, specifically radius, has on ETC given the importance of leading edge radius on convective heating (Eq. 1.2). The majority of the study utilizes 2D planar leading edges but an axisymmetric (i.e. cone instead of a wedge) is also considered.

A mesh is generated for the geometry with only one-half of the leading edge considered in the numerical simulations in order to reduce the computational cost using the axial vector as the line of symmetry as shown in Figure 3.2. The computational grid contains approximately 20,000 cells, with 125 cells along the surface and 160

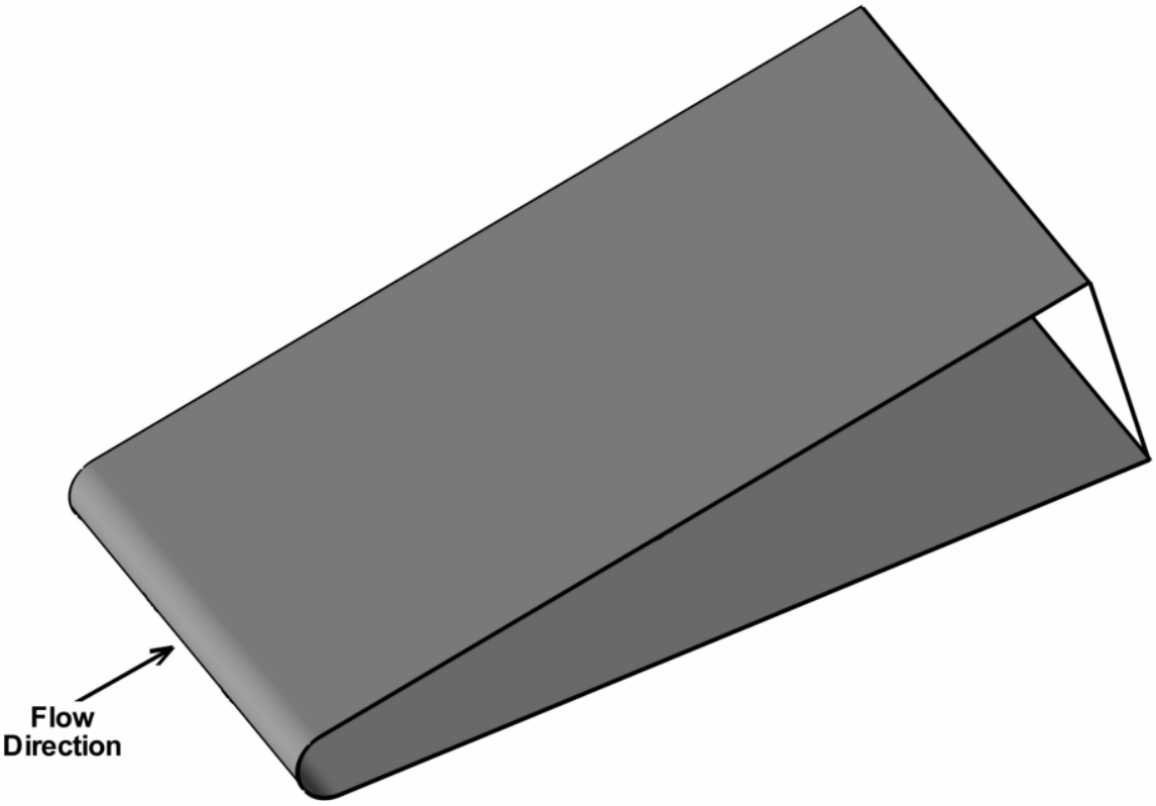

(a) 3-D view.

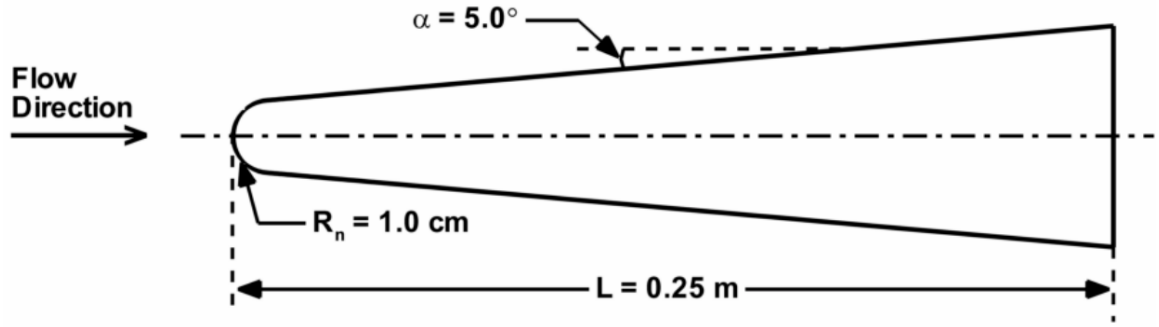

(b) Cross-sectional view.

Figure 3.1: Test case geometry.

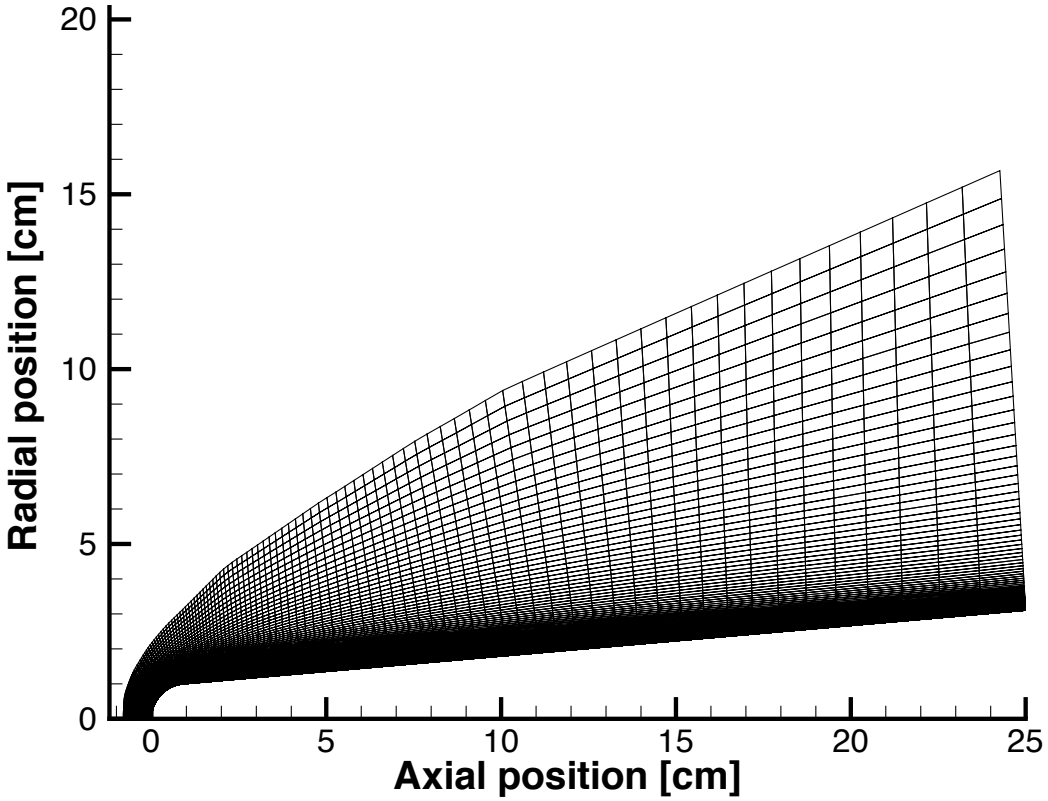

Figure 3.2: Computational grid for ETC study.

cells normal to the vehicle with a higher density of cells near the vehicle surface in order to capture the effects in the high gradient region of the boundary layer. A grid convergence study using the conditions, with and without ETC, revealed that the solutions are grid-independent using this mesh. This study employed a similar approach detailed in Ref. [149], where the mesh was continued to be refined until the surface properties (e.g. temperature and electron number density) proved to be grid independent.

3.2.2 Freestream conditions

The freestream is characterized by the species present in the flow, the density of the species, the temperature of the flow, and how fast the vehicle is traveling. For this chapter, the flow is treated as 11-species air.[2] The species present in the freestream

[2] N_2, O_2, N, O, NO, N_2^+, O_2^+, N^+, O^+, NO^+, and e^-.

Table 3.1: Freamstream conditions by altitude.

Altitude [km]	T [K]	ρ [kg/m^3]	
		N_2	O_2
30	217	1.18×10^{-2}	3.60×10^{-3}
60	238	1.76×10^{-4}	5.39×10^{-5}

(i.e. pre-shock), their density and temperature are determined by the altitude. The Naval Research Laboratory's temperature and density model, MSISE-00, is used to determine these properties by altitude [81]. The baseline altitude considered is 60 km as it was the altitude used in previous ETC studies [110, 140] but as discussed in Section 2.2, the continuum assumption begins to break down at high altitude so a lower altitude of 30 km is also investigated. This allows the effect that altitude (e.g. density of freestream) has on ETC to be determined and the lower altitude also allows for the sharpest leading edge (i.e. 1 mm) to be accurately modeled with negligible slip effects present. The freestream properties dependent on altitude are presented in Table 3.1. As shown in Figure 1.3, a typical hypersonic vehicle flight path will travel through different altitudes and velocities, however, this study will only investigate one trajectory point (i.e. flight velocity and altitude) at a time and investigate at steady-state.[3] As discussed in Section 2.1.2, the slowest velocity considered is 3 km/s and the fastest is 8 km/s with a baseline velocity equal to 6 km/s.

3.2.3 Material properties

The exact material properties for ETC are largely unknown as candidate materials are currently being identified, developed, and investigated. One of the purposes of this study is to determine how different material properties affect ETC and to help guide the development of the materials. Clearly, an appropriate material for ETC would

[3]With the exception of in-depth surface conduction in Section 3.8, which is flight duration sensitive.

have a low work function and also a high tolerance for heat and oxidizing atmospheres. Most typical low-work-function materials such as Ba-O impregnated porous tungsten, LaB_6, and cesium are not appropriate for a hypersonic environment due to easily being oxidized [22]. However, a class of materials called ceramic electrides is currently being developed as electron emitters and cathodes that may be suitable for ETC [150, 151, 152]. This class of material combines the beneficial properties of ceramics (e.g. high temperature tolerance and resistance to oxidation) with low electrical resistivity and low work functions ($\sim$ 2 eV) [153]. Another type of material that may be appropriate for ETC is a refractory metal composite [22] such as a mayenite electride-metallic titanium composite [154]. The issue of candidate materials for ETC is still an open question that requires detailed investigation since different materials may have various responses related to their electronic structure and properties, besides the work function [51, 155].

Since the issue of candidate materials for ETC is still an open question, this study investigates a range of material properties to identify material properties that maximize the benefits of ETC that will help guide material development. Two pertinent material properties to ETC are the material work function (i.e. how effective the material is at emitting electrons to cool the surface) and material emissivity (i.e. how effective the material is at emitting photons to cool the surface[4]). The spectrum of work functions considered is 2 to 3 eV, which is in the range of the materials currently being developed [22]. The material work function is assumed to be constant, whereas it could vary during hypersonic flight due to material degradation from the thermally intense, oxidized environment. The material radiative emissivity is assumed to be blackbody ($\epsilon = 1$) unless otherwise noted. Treating the surface as a blackbody allows radiative cooling to be as effective as possible. Lower material emissivities are also considered to investigate how ETC performs when radiative cooling is less effective

[4]Compared to an ideal radiator or *blackbody*.

Table 3.2: Material properties of potential ETC materials.

Material	Thermal conductivity, [W/m/K]	Specific heat capacity, [J/kg/K]	Density [g/cm^3]	Refs.
UHTC[5]	50 - 70	600 - 800	5 - 6	[156, 157, 158, 159]
Mayenite ceramic	~ 2	N/A	~ 3	[153, 160]
Titanium	~ 20	~ 500	4.5	[161]
Titanium diboride	~ 80	1000 - 1400	4.5	[162]

in Chapter IV.

Two additional material properties are required to determine the in-depth surface conduction, which are the material's thermal conductivity and specific heat capacity. The thermal conductivity is essentially the rate at which heat passes through the material and the specific heat capacity is the heat required to result in a temperature change of the material. Specific heat capacity for TPS materials are typically temperature dependent as is the thermal conductivity, while also being anisotropic. Thermal conductivities and specific heat capacities for certain materials that are currently used on TPS or could be used for ETC surfaces are provided in Table 3.2. The density of the material is included because it is used in combination with the specific heat capacity to determine the amount of heat that is required to increase 1 kg of material, by 1 K in temperature. Since the ETC material will likely be a hybrid material, properties such as thermal conductivity and specific heat will rely heavily on the as-manufactured state so they are still largely unknown. In order to clarify the analysis and to focus on *how in-depth surface conduction affects ETC* rather than determining the exact material properties, lower and upper bound values of thermal conductivity and specific heat capacity are chosen and assumed to be temperature independent and isotropic in the test cases. The thermal conductivities investigated are 10 and 80 W/m/K and the specific heat ratios are 600 and 1200 J/kg/K. The material density is assumed to equal 5 g/cm^3.

[5] ZrB_2-SiC composite that was used on HTV-2.

3.3 Flowfield features

The flowfield features without ETC are shown in Figure 3.3, which show the translational temperature contours for the baseline case of 6 km/s freestream velocity with a 1 cm leading edge radius at 60 km altitude. This velocity corresponds to Mach 19.4 at this altitude. The flow is characterized by a strong bow shock that develops around the leading edge. The translational temperature rises to over 16,000 K across the shock before decreasing in the shock layer. Figure 3.4 presents the distribution of translational and vibrational[6] temperatures along the stagnation line for freestream velocities of 4, 6 and 8 km/s and the level of ionization (α) for each case is shown in Figure 3.5. As the freestream velocity increases, the level of thermal nonequilibrium (i.e. the difference between translational and vibrational temperatures) increases along the stagnation line. The level of ionization along the stagnation line increases as the freestream velocity increases, which is expected due to the higher flow temperature for higher freestream velocity. However, even with the increase in ionization, the flow is still weakly ionized.

3.4 Surface features

The surface temperature and heat transfer profiles for the cases without ETC are shown in Figure 3.6 for the different freestream velocities of interest. Note that the distance along the leading edge is defined as, $s = \sqrt{x^2 + y^2}$, and is normalized by the leading edge radius, R_n. The surface temperature reaches over 3,100 K and the convective heating rate exceeds 600 W/cm^2. The convective heating rate increases with freestream velocity at nearly the rate predicted by Equation 1.2. The surface temperature and convective heat transfer for each case are highest near the stagnation point and decreases along the vehicle. For the cases without ETC, the steady-state

[6]The electron and electronic temperatures are assumed to equal vibrational temperature.

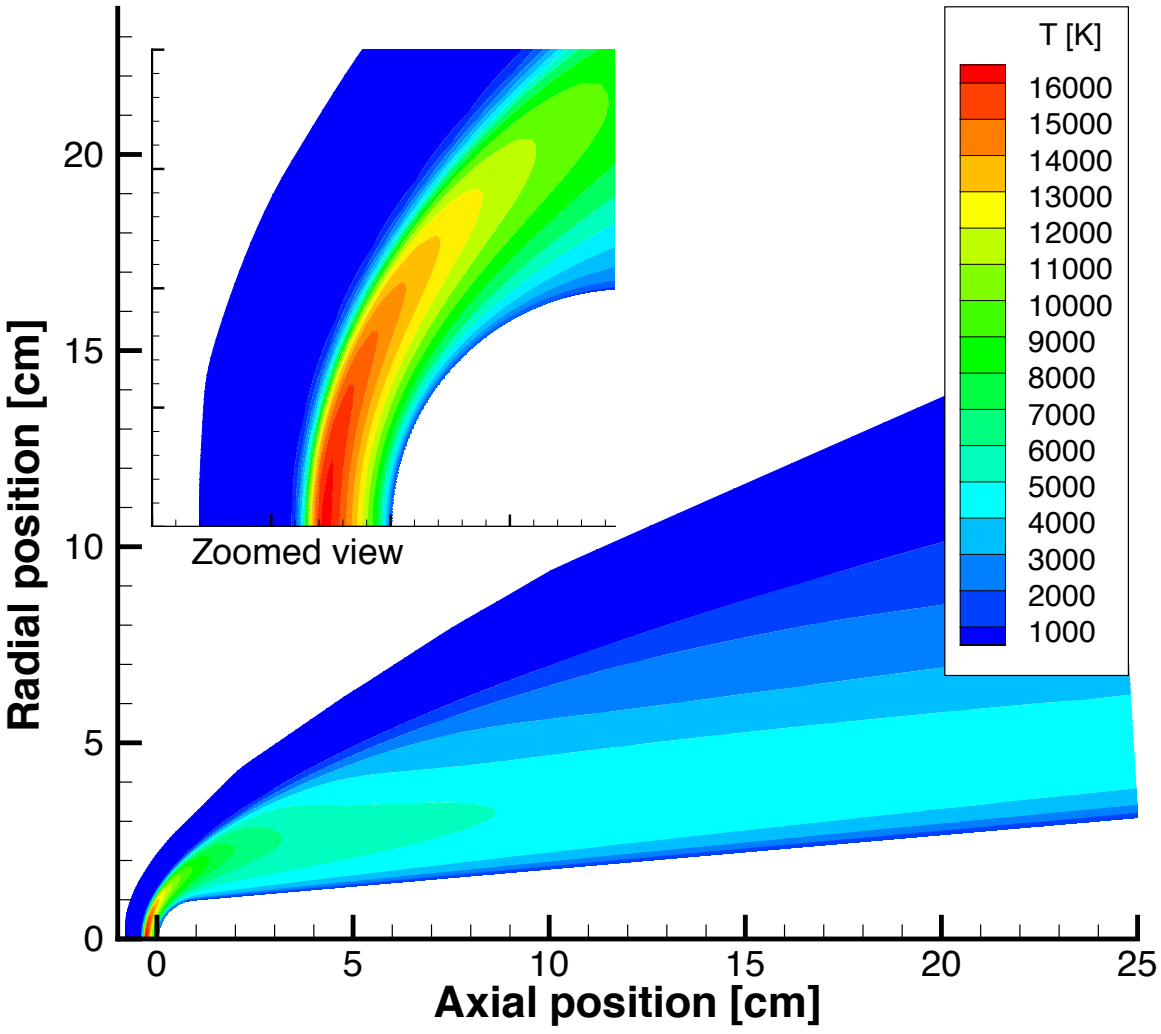

Figure 3.3: Temperature contour for the baseline case of 6 km/s freestream velocity with a 1 cm leading edge radius at 60 km altitude without ETC.

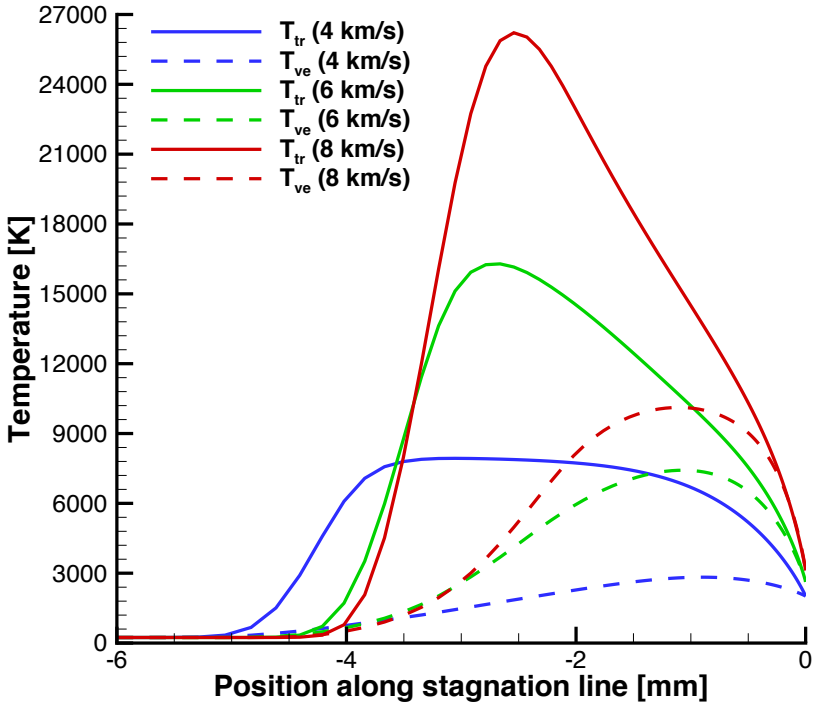

Figure 3.4: Temperature profiles along stagnation streamline for different velocities without ETC.

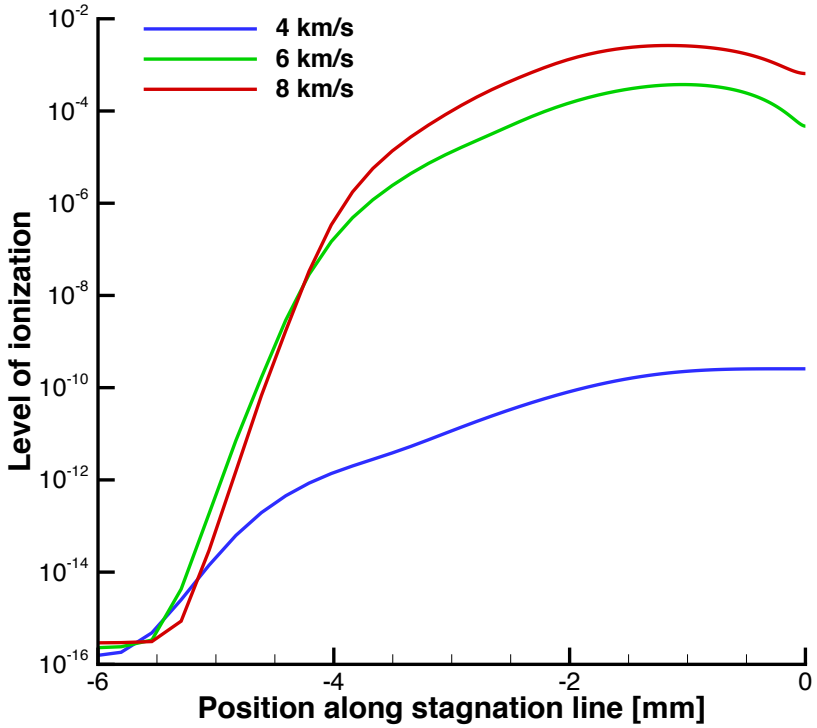

Figure 3.5: Level of ionization along stagnation streamline for different velocities without ETC.

surface temperature is determined by balancing the convective heating rate to the radiative cooling, which assumes blackbody radiation.[7] At these high temperatures, many of the current materials used for TPS on the sharp leading edges of hypersonic vehicles reach limitations. For example, at temperatures higher than approximately 1,900 K, Si-based UHTCs become susceptible to oxidation, which degrades the material and limits their use for extended flights [46]. Additionally, the melting point of a pure zirconium boride UHTC is near 3,000 K, but the presence of SiO_2, such as was used on the HTV-2, lowers the melting point to less than 2,000 K [163]. With the current state-of-the-art hypersonic flight vehicles reaching a top speed of approximately 3 km/s, these materials do not reach these surface temperatures[8] but as the speed of flight increases, they will no longer be suitable. The surface pressure profiles for different velocities are shown in Figure 3.7. The increase of pressure with increasing velocity highlights the increase of drag with increasing freestream velocity (Eq. 1.1). Although not shown, viscous contributions to drag also increase with freestream velocity [16, 164].

The Debye length, mean free path, and sheath collisionality profiles for the cases without ETC are shown in Figure 3.8. These profiles are pertinent to the analytic plasma sheath relations. The Debye length (e.g. the non-neutral region between the surface and quasineutral flow) is on the order of micrometers for the high freestream velocity cases (i.e. 6+ km/s). However, for more moderate freestream velocities (i.e. 4 km/s), the Debye length is much larger. This is due to the Debye length being inversely proportional to the square-root of the number density of electrons. Higher freestream velocities result in stronger shocks causing higher post-shock temperatures in the flow, making the flow more susceptible to ionization. This is an important trend that will be seen in future results and an influential flow characteristic in the

[7] If radiation is less than blackbody radiation, the surface temperature will increase in order to compensate to balance the heat transfer rate at the surface.

[8] At least for these operating conditions (i.e. geometry and altitude)

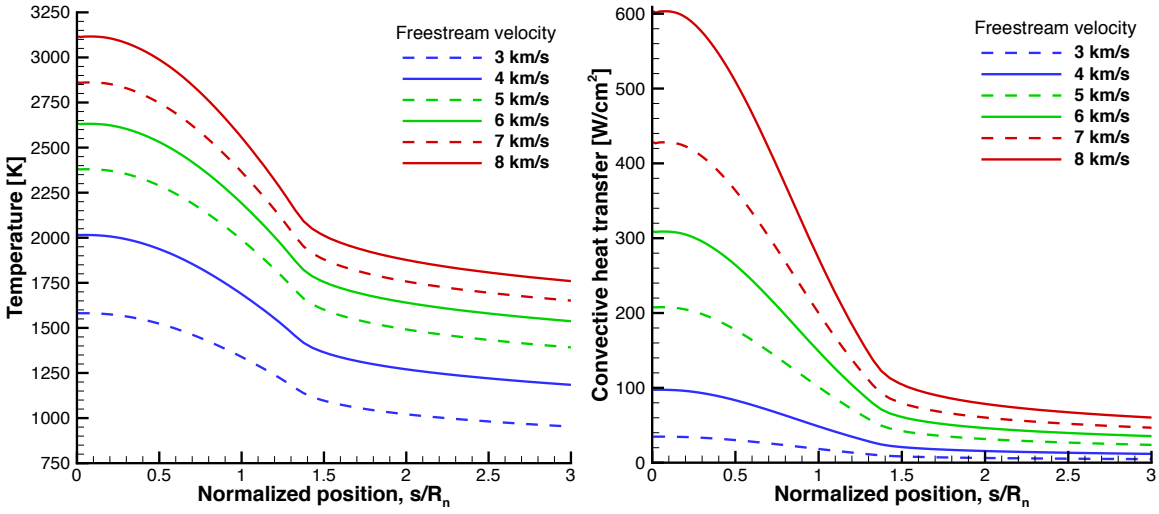

(a) Temperature.

(b) Convective heat transfer.

Figure 3.6: Surface temperature and heat transfer profiles for the cases without ETC.

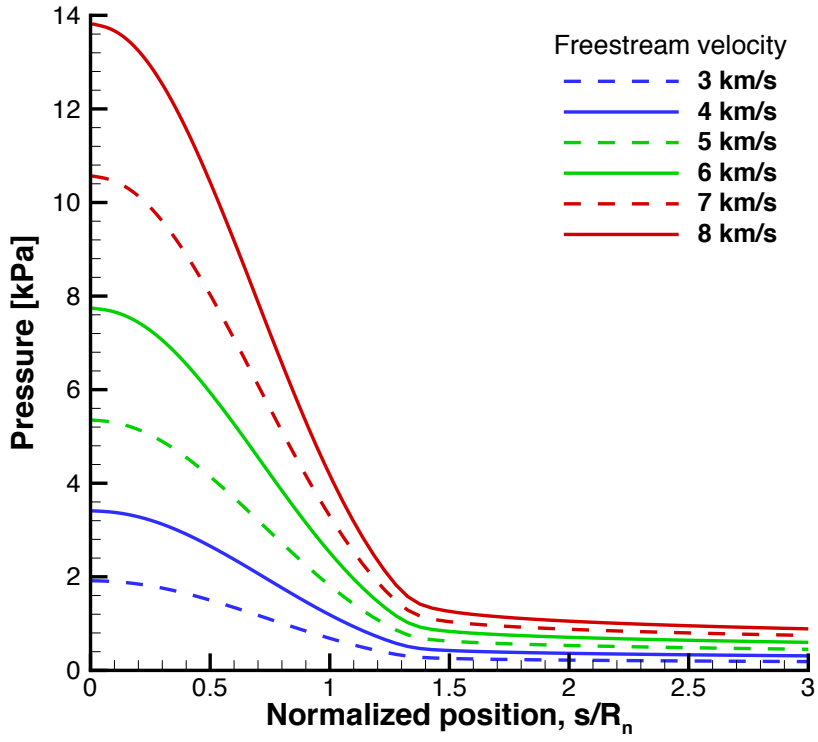

Figure 3.7: Surface pressure profiles for different velocities without ETC.

application of ETC to leading edges of hypersonic vehicles. The electron-neutral and ion-neutral mean free path profiles are shown in Figure 3.8(b). Both the electron-neutral and ion-neutral mean free paths depend on the number density of electrons and ions but are also dependent on the number density of neutral particles (Eq. 2.44a) that, since the flow is weakly ionized, have a significantly higher number density than the charged species. The electron-neutral mean free path is larger than the ion-neutral mean free path due to electrons having a smaller collisional cross section with neutrals. Relating the Debye length and mean free path of the charged species with neutrals results in the collisionality of the sheath (i.e. approximately how many collisions occur with the sheath). For the larger freestream velocities (i.e. 6+ km/s), the sheath collisionality is less than 0.1 for both charged species, which justifies the use of the collisionless sheath models discussed in Section 2.5.2. For the lower freestream velocity (i.e. 4 km/s), the collisionality of the sheath surpasses unity so the assumption of a collisionless sheath breaks down. However, as will be shown ETC is more effective at higher velocities so accurately modeling the sheath physics at lower velocities is less crucial.

3.5 Saturated emission

ETC is first modeled assuming the emission reaches saturation levels (i.e. Richardson current from Eq. 2.4). This results in the maximum amount of emission current possible based on material properties (e.g. temperature, work function) and assumes ideal conditions.[9] This approach is investigated first to see if ETC with an ideal emission assumption can produce cooling benefits to leading edges of hypersonic vehicles and to determine the maximum possible cooling benefits ETC can have, even if conceptual. Figure 3.9 shows that ETC has an overall small effect on the flowfield

[9]Emitted electrons see no retarding electric field at the surface, are not reflected back to the surface through collisions, nor see a virtual cathode created by space-charge limit.

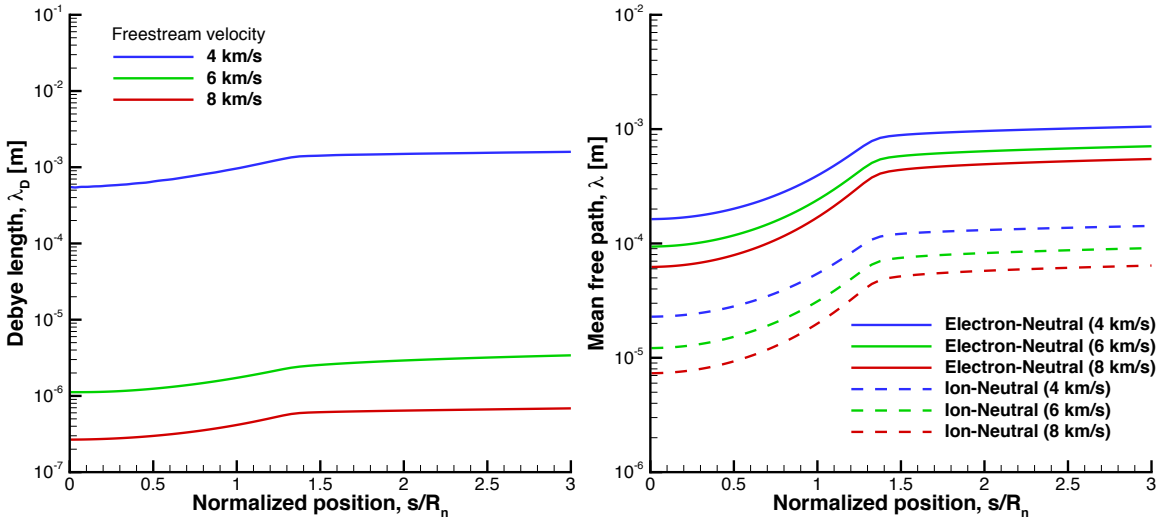

(a) Debye length.

(b) Mean free path.

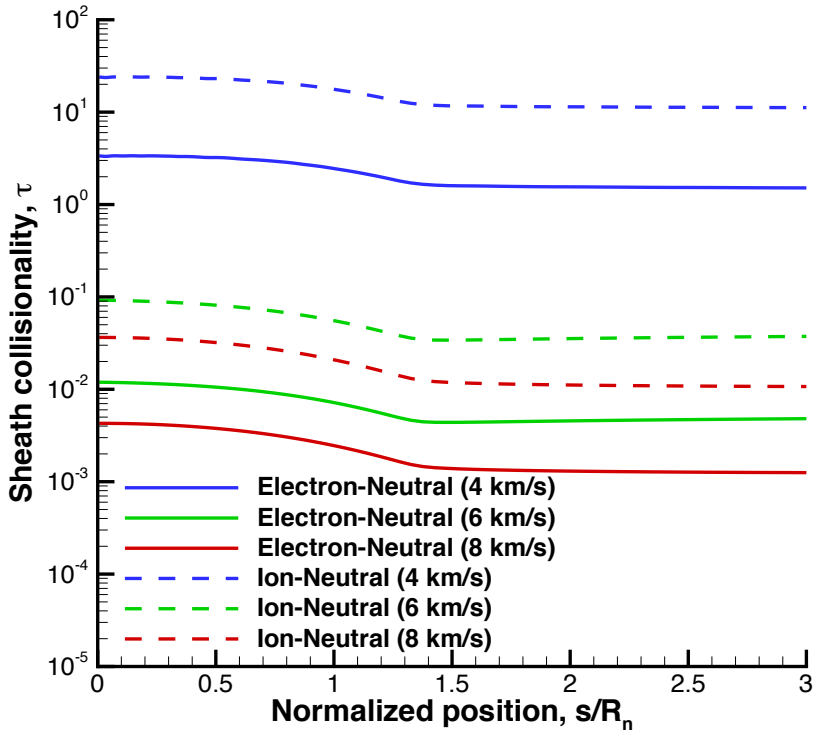

(c) Sheath collisionality.

Figure 3.8: Debye length, mean free path, and sheath collisionality profiles for the cases without ETC.

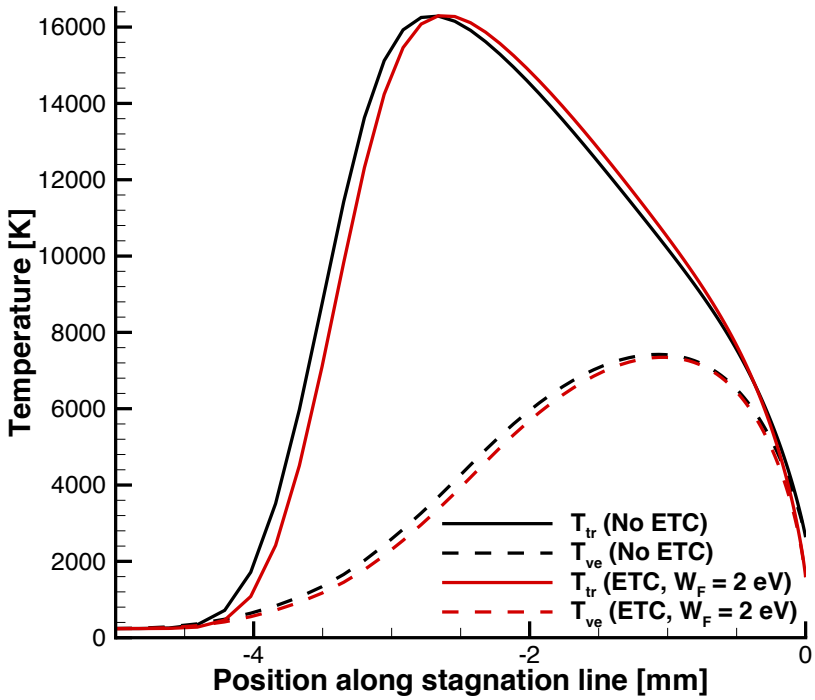

Figure 3.9: Temperature profiles along stagnation streamline without and with saturated ETC.

features for the baseline case of 6 km/s freestream velocity at 60 km. However, the differences include the shock standoff distance being slightly smaller and the surface temperature is lower for the case with electron emission. Figure 3.10 presents the charged species number densities along the stagnation streamline for the case with and without ETC. As expected, ETC increases the electron number density near the surface. The ion number density for the case with ETC decreases near the surface due to the recombination of ions given by Equation 2.16.

The temperature and heat transfer distributions along the vehicle surface are presented in Figure 3.11. Near the leading edge, the cases with ETC lower the surface temperature significantly with approximately a 18%, 28%, and 40% reduction compared to the case without ETC for the work function values of 2, 2.5, and 3 eV, respectively. However, this reduction in surface temperature results in higher convective heating rates as shown in Figure 3.11(b). It is expected that a lower surface temperature corresponds to a higher convective heat transfer because the flowfield

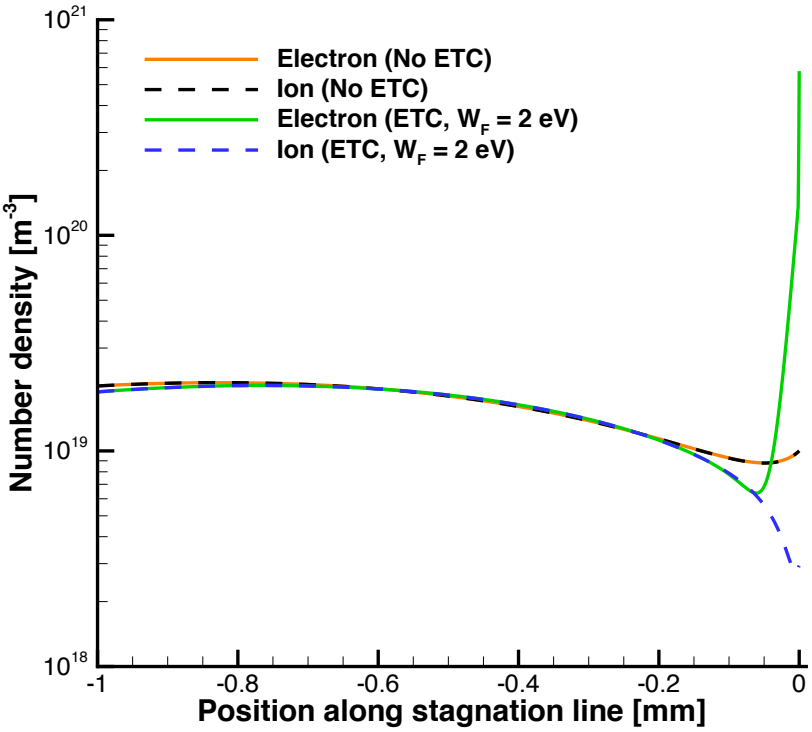

Figure 3.10: Charged species number densities along the stagnation streamline without and with saturated ETC.

temperature is minimally changed by ETC, and a larger temperature gradient will result in more convective heat transfer due to Fourier's Law. This reiterates how high convective heating rates are inherent to high-speed flight, which was discussed in Chapter I. Since high convective heating rates will always be present, especially if the goal is to maintain a cool vehicle surface, the key is to be able to manage the heating rates while keeping the surface at an operable temperature. ETC appears to meet this challenge for this one trajectory point and assuming ideal emission. Without ETC, the stagnation temperature is over 2,600 K and there are currently no materials that can withstand this temperature for an extended period of time while also being suitable for a leading edge of a hypersonic vehicle. However, with ETC and assuming the emission is saturated, the surface temperature is greatly reduced to much more manageable levels.

The emission current density and mass blowing rate profiles for this case are

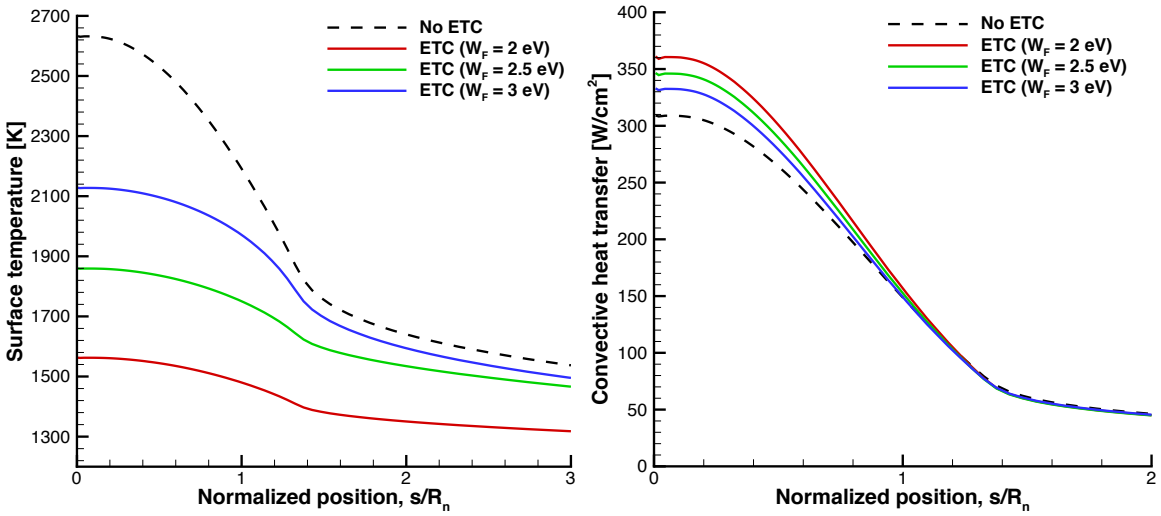

(a) Temperature.

(b) Convective heat transfer.

Figure 3.11: Surface temperature and heat transfer profiles for the cases with saturated ETC at 6 km/s freestream velocity.

shown in Figure 3.12. As expected, a lower material work function results in a higher emission current density from the surface, which also corresponds to a higher mass blowing rate from the surface. The mass blowing rate of the material (i.e. electrons) from the surface is negligible compared to ablative cooling.[10] The heat transfer rates away from the surface are shown in Figure 3.13. For each case with ETC, ETC is the dominant mode of cooling compared to radiation and becomes more effective at lower material work functions. For example, for a 3 eV material work function, ETC comprises approximately 60% of the cooling power but for a low work function of 2 eV, ETC encompasses 90% of the cooling power. ETC with saturation emission being more effective than radiative cooling is expected for these range of surface temperatures, as shown in Figure 2.1.

Given the promising trend ETC shows for the baseline case, the test cases are extended to look at different parameters and how ETC with saturated emission performs. Table 3.3 presents the stagnation point conditions for the same leading edge

[10]The ablative material that was used on Stardust, PICA, has a mass blowing rate on the order of 0.1 kg/s/m^2 [165]. It is to be noted that Stardust had a reentry velocity of nearly 13 km/s so the comparison is not necessarily fair.

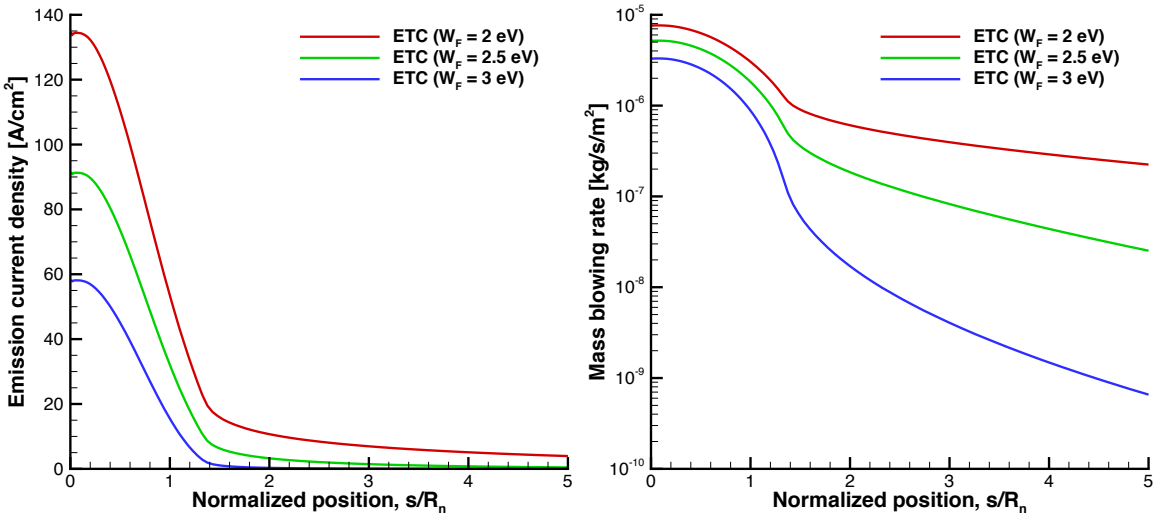

(a) Emission current density.

(b) Mass blowing rate from surface due to emission.

Figure 3.12: Emission current density and mass blowing rate surface profiles for the cases with saturated ETC at 6 km/s freestream velocity.

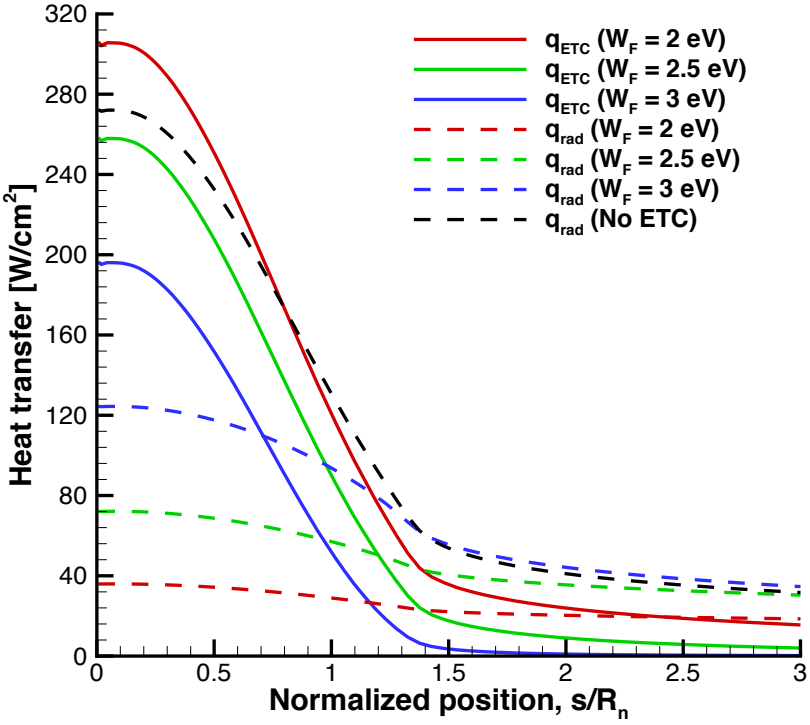

Figure 3.13: Heat transfer rates away from the surface without and with ETC.

radius of 1 cm at 60 km altitude but at different velocities. A work function of ∞ corresponds to a case without ETC as it would require infinite energy to remove an electron from the surface. As discussed previously, for cases without ETC, the convective heating rate is balanced only by radiative cooling and increases with freestream velocity. For the slowest freestream velocity considered, 3 km/s, ETC only reduces the surface temperature noticeably for the lowest work function considered, 2 eV, and the cooling power from ETC is equivalent to the cooling power provided by radiation for this case. However, as the freestream velocity is increased, the temperature reduction of the surface is magnified and ETC becomes the more dominant mode of cooling, especially at higher velocities and lower work functions. For example, for the most extreme case considered, 8 km/s freestream velocity and 2 eV work function, ETC provides over 90% of the cooling power of the surface compared to radiative cooling. This trend is expected because the cooling power of ETC with saturated emission rises very quickly with temperature as was shown in Figure 2.1. This trend is also what makes ETC a promising concept in that it is passive at slower velocities where suitable TPS exist and as the velocity is increased to where no current TPS is suitable, ETC becomes active and keeps the surface at manageable surface temperatures. For example, if the flight speeds theoretically vary from 3 to 8 km/s at this altitude, the surface temperature would increase by 1,540 K. But if ETC was utilized with a material work function of 2 eV and saturation emission was realized, the surface temperature would only increase by 300 K. Another way to view the benefit of ETC is that flying at 8 km/s with a material work function of 2 eV results in a lower stagnation surface temperature than flying at 4 km/s without ETC. It is to be reminded that this trend appears when ETC is assumed to reach saturation limits, which is not always the case as will be shown in Section 3.6. Additionally, blackbody radiation was assumed for these cases. If the material emissivity is less than one, as shown by the only non-blackbody case ($\epsilon = 0.8$), radiative cooling is less effective

and ETC is more active and can be for even for less thermally intense flows (i.e. slower freestream velocities) as will be shown in Chapter IV. One axisymmetric case is also considered at 6 km/s. Compared to the 2D planar case, the axisymmetric case results in slightly higher surface temperatures but ETC is also slightly more effective at cooling.

A larger leading edge radius of 10 cm is also considered with the results shown in Table 3.4. The larger leading edge radius results in significantly lower convective heating rates compared to the smaller leading edge, as expected from Equation 1.2. ETC even causes a slight increase in stagnation temperature for the 4 km/s freestream velocity case with material work functions of 3 and 2.5 eV. This increase in surface temperature results from ETC cooling rates occurring at negligible amounts (i.e. less than 1 W/cm^2) due to the already low surface temperature of the material but the emission of even a relatively small amount of electrons from the surface causes an increase of diffusive heat transfer. Diffusive heat transfer is negligible for the cases without ETC but for the case with ETC, the surface is assumed to be fully-catalytic, which results in an increase in diffusive heat transfer to the wall from the exothermic recombination of emitted electrons to the flowfield ions (Eq. 2.16). For the remaining cases, ETC results in a lower surface temperature but the temperature reduction is much less compared to a smaller leading edge radius. This supports the idea that ETC is more effective at cooling hotter surfaces and since a blunter leading edge results in a cooler surface, ETC is less effective.

Table 3.3: Stagnation point conditions for 1 cm leading edge radius at 60 km altitude for cases with saturated emission.

u_∞, [km/s]	W_F, [eV]	T_w, [K]	T_w, % reduction	q_{conv}, [W/cm^2]	q_{rad}, [W/cm^2]	q_{ETC}, [W/cm^2]
3	∞	1580	-	35	35	-
	3	1570	0.6	35	35	0.2
	2.5	1530	3.2	35	31	4
	2	1360	14	37	19	18
4	∞	2020	-	94	94	-
	3	1930	4.5	99	78	21
	2.5	1730	14	101	51	50
	2	1470	27	104	26	78
5	∞	2390	-	183	183	-
	3	2090	13	213	109	104
	2.5	1830	23	219	65	154
	2	1540	36	226	33	193
6	∞	2630	-	272	272	-
	3	2170	17	322	125	197
	2.5	1890	28	331	72	259
	2	1590	40	343	36	307
6[a]	∞	2770	-	200	200	-
	3	2140	23	234	72	162
	2.5	1870	32	248	41	207
	2	1560	44	260	20	240
6[b]	∞	3220	-	609	609	-
	3	2280	29	642	153	489
	2.5	1980	39	661	87	574
	2	1660	48	682	43	639
7	∞	2860	-	380	380	-
	3	2220	22	448	138	310
	2.5	1930	33	461	79	382
	2	1620	43	475	39	436
8	∞	3120	-	535	535	-
	3	2230	29	635	153	482
	2.5	1980	37	651	87	564
	2	1660	47	668	43	625

[a] $\epsilon = 0.8$ instead of $\epsilon = 1.0$ (i.e. blackbody radiation).

[b] Axisymmetric geometry (i.e. cone) instead of 2D planar wing (i.e. wedge).

Table 3.4: Stagnation point conditions for 10 cm leading edge radius at 60 km altitude with saturated emission.

u_∞, [km/s]	W_F, [eV]	T_w, [K]	T_w, % reduction	q_{conv}, [W/cm^2]	q_{rad}, [W/cm^2]	q_{ETC}, [W/cm^2]
4	∞	1350	-	19	19	-
	3	1390	+3	21	21	0.01
	2.5	1380	+2	22	21	0.5
	2	1280	5	25	19	6
6	∞	1730	-	50	50	-
	3	1690	2.3	47	46	1.3
	2.5	1600	7.5	48	37	11
	2	1390	20	49	21	28
8	∞	2100	-	111	111	-
	3	1960	6.7	112	83	29
	2.5	1750	17	118	53	65
	2	1490	29	127	28	99

A smaller leading edge radius is also considered. However, in order to accurately model this sharper leading edge radius and for the continuum approximation to still be valid, it must be considered at a lower altitude as discussed in Section 2.2. An altitude of 30 km is chosen and the baseline geometry of 1 cm leading edge radius is considered first with the results shown in Table 3.5. The lower altitude results in a higher surface stagnation surface temperature compared to the higher altitude cases in Table 3.3, which is expected due to the more dense flow. However, these higher surface temperatures result in ETC being more active and effective with the surface temperature being reduced up to 58% and 65% for the 6 and 8 km/s freestream cases with 2 eV material work function, respectively. This shows that ETC is more effective at lower altitudes, at least for when emission is assumed to be saturated. The results for the smaller leading edge radius are provided in Table 3.6. The very sharp leading edge results in large convective heating rates. Saturated ETC also results in significant reduction of the surface temperature for each freestream velocity and material work function considered. These reductions in surface temperature result in massive convective heating rates and ETC is the primary method of cooling for each

Table 3.5: Stagnation point conditions for 1 cm leading edge radius at 30 km altitude with saturated emission.

u_∞, [km/s]	W_F, [eV]	T_w, [K]	T_w, % reduction	q_{conv}, [W/cm^2]	q_{rad}, [W/cm^2]	q_{ETC}, [W/cm^2]
4	∞	2710	-	308	308	-
	3	2220	18	442	137	305
	2.5	1940	28	500	81	419
	2	1640	39	566	41	525
6	∞	4220	-	1790	1790	-
	3	2460	42	2000	208	1800
	2.5	2130	50	2080	117	1960
	2	1790	58	2190	58	2130
8	∞	5450	-	4990	4990	-
	3	2630	52	5470	272	5200
	2.5	2280	58	5600	154	5450
	2	1920	65	5740	77	5660

case. For the most extreme example (i.e. 8 km/s freestream velocity and a material work function of 2 eV), ETC provides 99% of the surface cooling. Although ETC is effective at cooling at this low altitude it is to be reminded that the higher freestream flow density found at lower altitudes increases the drag (Eq. 1.1).

If saturation emission is realized, ETC can be a very effective cooling mechanism for leading edges of hypersonic vehicles and maintaining the surface temperature at a manageable surface temperature even as the freestream velocity reaches orbital velocities. However, it is be remembered that this type of emission is ideal and only happens in conditions where emitted electrons see no retarding electric field at the surface, are not reflected back to the surface through collisions, nor see a virtual cathode created by a space-charge limit. The following section will explore how these effects can affect ETC performance. Investigating ETC assuming saturation emission is still a beneficial study as it determines the maximum cooling power ETC can provide, even if conceptual.

Table 3.6: Stagnation point conditions for 1 mm leading edge radius at 30 km altitude with saturated emission.

u_∞, [km/s]	W_F, [eV]	T_w, [K]	T_w, % reduction	q_{conv}, [W/cm^2]	q_{rad}, [W/cm^2]	q_{ETC}, [W/cm^2]
4	∞	3380	-	741	741	-
	3	2400	29	1340	187	1150
	2.5	2090	38	1490	108	1380
	2	1760	48	1650	54	1600
6	∞	4870	-	3200	3200	-
	3	2620	46	5080	267	4810
	2.5	2270	53	5360	152	5210
	2	1920	61	5730	76	5650
8	∞	6220	-	8510	8510	-
	3	2820	55	15,200	361	14,800
	2.5	2450	61	15,800	207	15,600
	2	2070	67	16,400	106	16,300

3.6 Plasma sheath effects

As discussed in Section 2.5, plasma sheath physics play an important role on how emitted electrons behave and can limit how many electrons escape the near wall region to the flowfield. For example, emission can lead to a significant electron cloud forming near the emission surface creating a virtual cathode that forces a portion of the electrons back to the surface before leaving the plasma sheath. Section 2.5 introduced two classes of analytic sheath models developed by the plasma sheath community depending on the emissive surface type to determine this limit. The first approach treats the emissive surface as an electrically floating surface.[11] This is the type of surface that is expected to occur if there is not an internal circuit or battery *driving* the emission and the emissive surface is electrically insulated from where the electrons are collected. The second surface type investigated treats the surface as a negatively biased surface.[12] A surface such as this would occur if the emitted electrons reattach downstream on the vehicle and travel back to the emitter surface completing

[11] Analogous to an emissive floating Langmuir probe.
[12] Analogous to an emissive double probe.

the circuit as shown in the schematic in Figure 2.10. This circuit, assuming the same current of electrons are collected on the aft-body of the hypersonic vehicle, would prevent the vehicle from obtaining a net charge and be potentially less susceptible to electric arcing.[13]

3.6.1 Electrically floating surface

If the emissive surface is electrically floating and non-conducting, then by definition, the net current through the sheath must be zero[14] and the analytic models discussed in Section 2.5.2.1 are utilized in the CFD framework. It is to be noted that the theories assumed only one ion species, whereas the hypersonic environment used in LeMANS has multiple ion species. Having more than one ion in species in the flowfield will have an effect on space-charge limits, but is is assumed that the effect is minimal. For this work, the ion masses are averaged by number density and an average ion mass is used in the sheath models implemented in LeMANS.

Figure 3.14 presents the surface temperature profiles for the baseline case of a hypersonic leading edge with a 1 cm radius and a freestream velocity of 6 km/s at 60 km altitude. The cases including plasma sheath physics result in a slightly lower surface temperature near the leading edge compared to the case without ETC. However, near the leading edge, these cases does not realize the significant surface temperature reductions predicted by temperature saturated ETC. This is due to the emission being greatly limited by space-charge limits as shown in Figure 3.15(a). For the space-charge limited cases, a significant portion of the electrons are returned to the surface and do not escape the sheath contributing to the ETC heat transfer shown in Figure 3.15(b). For example, only 3% and 8% of electrons emitted from the surface escape the plasma sheath for material work functions of 2 and 3 eV, respectively, compared to saturated emission. Additionally, although the same level of space-

[13]Discussed briefly in Section 5.3.5.

[14]If the surface is conducting, then only the integrated total current to the surface must be zero.

charge limited emission is obtained for the 2 and 3 eV material work function cases, the 3 eV case results in a slightly higher value of ETC heat transfer and thus a slightly lower surface temperature. This is due to the emitted electrons overcoming a larger potential barrier (Eq. 2.3). This contradicts the results for the cases in Section 3.5, where space-charge limits were neglected, in that a lower work function does not always result in lower surface temperatures and higher ETC heat fluxes if space-charge limits are reached. If space-charge limits are reached, minimizing the material work function is no longer necessary and can even be less beneficial to ETC. This suggests that there is an *ideal* work function where the temperature limited emission (i.e. saturated) predicted by Equation 2.4 equals space-charge limited emission if space-charge limits are present,

$$W_F = \frac{-k_B T_w}{e} \log\left(\frac{J_{e,sc}}{A_R T_w^2}\right). \tag{3.1}$$

This is the material work function that would precisely result in the maximum amount of emission allowed by space-charge limits while also preserving an as large as possible potential barrier in the material for the electrons to overcome to maximize the cooling benefits. For this test case, the ideal material work function at the stagnation point would be 4.2 eV.

Both slower and faster velocities are also considered to investigate how freestream velocity affects space-charge limits for an electrically floating surface. The surface temperature profiles for the 4 km/s profile are shown in Figure 3.16(a). For this case, ETC actually results in a slightly higher surface temperature that is due to the level of emission that escapes the plasma sheath being imperceptible as shown in Figure 3.17(a). This level of emission does not produce a high enough ETC heat transfer rate to offset the increase in diffusive heat transfer the emitted electrons incur by recombining with the flowfield ions at the assumed fully-catalytic wall. However, a

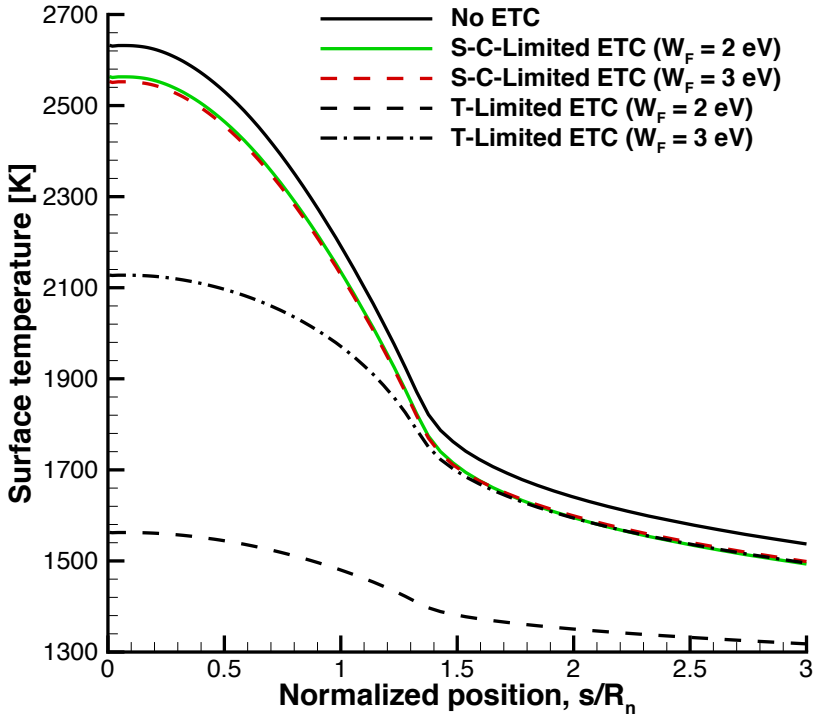

Figure 3.14: Surface temperature profiles for electrically floating surface for 6 km/s case.

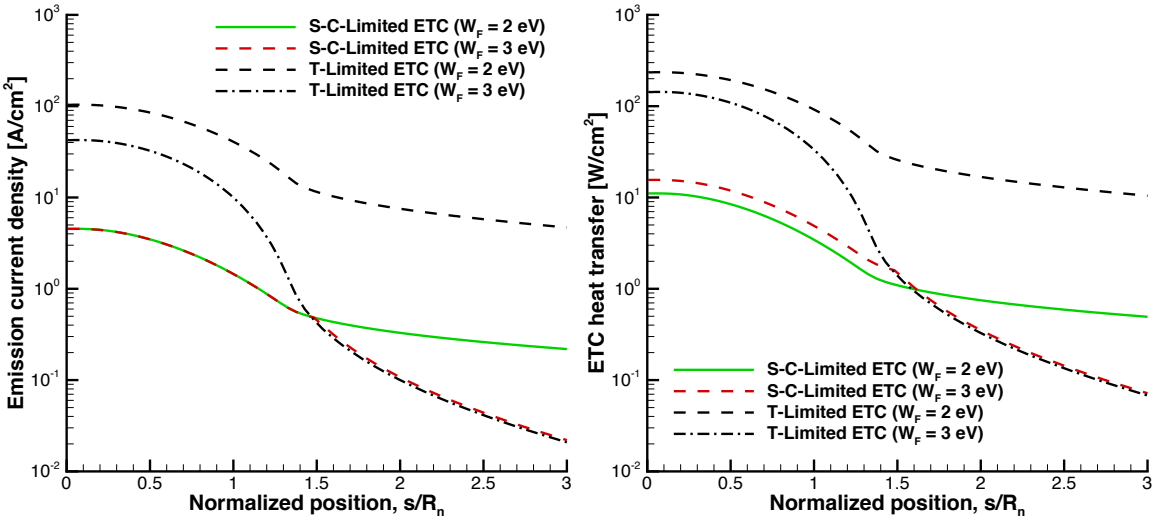

(a) Emission current density.

(b) ETC heat flux.

Figure 3.15: Surface emission current density and ETC heat transfer profiles for the cases with an electrically floating surface at 6 km/s freestream velocity.

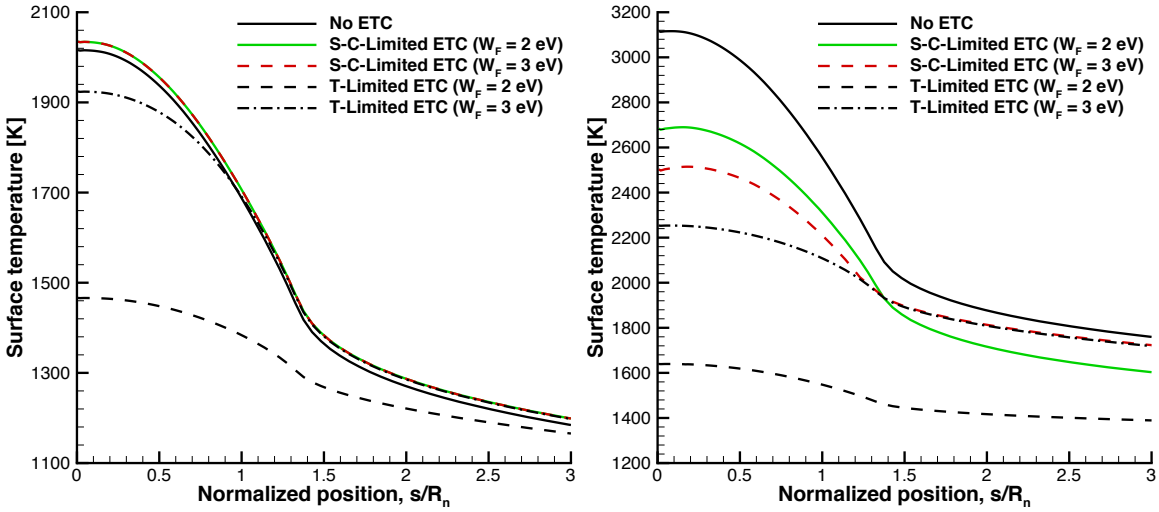

(a) 4 km/s.

(b) 8 km/s.

Figure 3.16: Surface temperature profiles for the cases with an electrically floating surface at 4 and 8 km/s freestream velocities.

higher freestream velocity of 8 km/s, results in a higher reduction in surface temperature with ETC compared to the slower velocities as shown in Figure 3.16(b). The surface temperature is reduced by approximately 14% and 20% for the cases with a work function of 2 and 3 eV, respectively. Although this is a distinct reduction in surface temperature, this case does not reach the ideal reductions in surface temperature determined with saturated emission. It is to be noted that, similar to the 6 km/s case, the higher work function value results in an appreciably larger reduction in surface temperature. This is because the space-charge limited emission determined for each material work function is less than the saturated emission as shown in Figure 3.17(b). Since each case has essentially the same emission, the cases with a higher work function retains a larger potential barrier within the material for the electron to use more energy to overcome providing additional cooling for the same level of current emission (Eq. 2.3). The ideal work function provided by Equation 3.1 is approximately 3.5 eV for this 8 km/s case, which is smaller than the ideal work function for the 6 km/s case but still larger than the targeted work function of 2 to 3 eV for ETC materials [22].

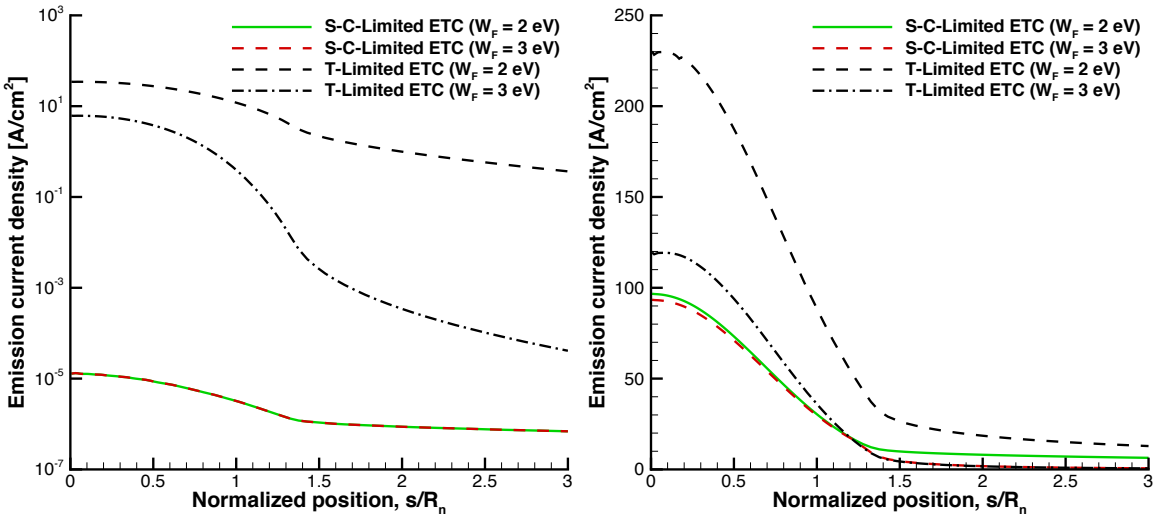

(a) 4 km/s. (b) 8 km/s.

Figure 3.17: Surface emission current density profiles for the cases with an electrically floating surface at 4 and 8 km/s freestream velocities.

As shown, higher velocities are less impacted by space-charge limited emission compared to slower velocities. This is because the level of ionization impacts space-charge limits as shown in the relations in Section 2.5.2.1. Larger levels of ionization at the surface[15] result in neutralizing the space-charge to some extent. This is why thermionic energy converters have historically used an easily ionizable gas, such as cesium, to improve the converter's efficiency [166]. The ion number density surface profiles for each freestream velocity are shown in Figure 3.18. The 4 km/s case has a significantly lower ion number density at the surface, which is why it was also the most affected by space-charge limits. As the freestream velocity increases so does the ion number density at the surface helping overcome space-charge limits. The higher ion number density results from the stronger shocks associated with higher velocities causing higher post-shock temperatures as shown in Figure 1.6, which ionize the flow.

While ETC can still result in reductions in surface temperature of a leading edge of a hypersonic vehicle, space-charge limits prevent ETC for an electrically floating surface from being as effective as predicted by the saturated emission assumption.

[15]Or sheath edge since the sheath is collisionless.

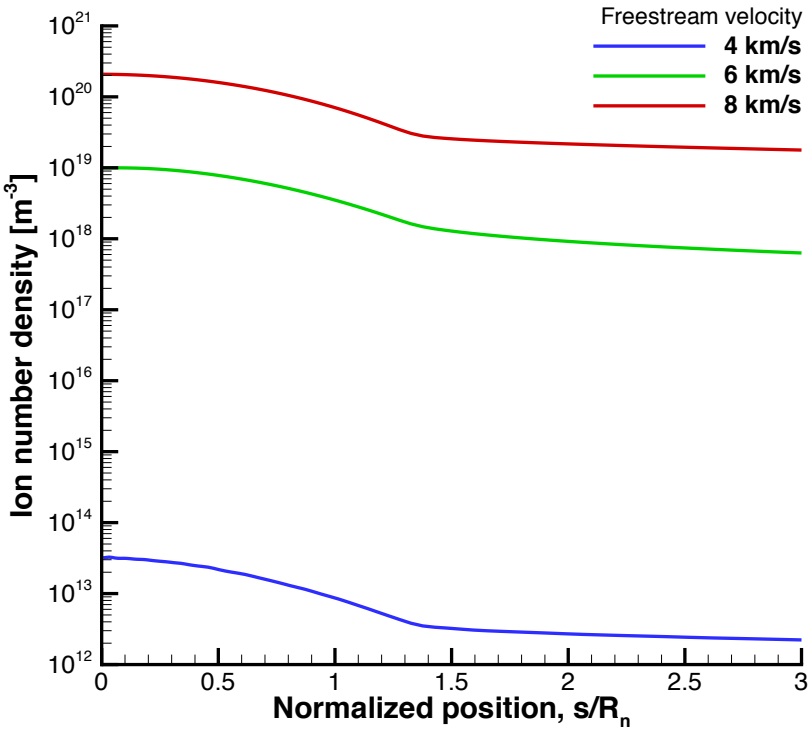

Figure 3.18: Ion number density surface profiles for different velocities without ETC.

These limits are less of a restriction for higher freestream velocities due to higher levels of ionization. However, even at orbital velocity where the level of ionization is the highest, the emission is still space-charge limited resulting in a leading edge surface temperature reduction of 20%. If higher surface temperature reductions are desired, the surface cannot be electrically floating and must be biased as discussed in the following section.[16]

3.6.2 Negatively biased surface

If the emissive surface is negatively biased where the collecting surface is electrically connected to the emissive surface,[17] a net current is permissible through the sheath and the analytic models discussed in Section 2.5.2.2 are utilized in the CFD framework. It is to be mentioned that the analytic model for the plasma sheath in the

[16] At least for this shape of leading edge (R_n = 1 cm) at an altitude of 60 km.

[17] Electrons emitted from the leading edge and collected on the aft-body as shown in Figure 2.10

presence of electron emission assumes a local 1D structure and the multidimensional effect of the plasma sheath is not taken into account. This is reserved for future work. While the theory for electrically floating emissive surfaces has been extensively studied and assessed over the past 90 years [133], the theory utilized in this work for negatively biased surfaces has been largely recently developed. For this reason, the analytic models used for this type of surface are assessed using a solver specialized for plasma sheaths in Section 3.9.

As discussed in Section 2.5.2.2, there are multiple approaches to model the emission for this type of surface. If the emission is exactly space-charge limited (i.e. saturation emission equals space-charge limited emission), then the emission from the surface will be cold in that the electrons will have negligible energy after being emitted and are accelerated by the sheath into the flow. If the saturation emission is larger than space-charge limited emission, the electrons will be emitted with a finite temperature but a virtual cathode will form pushing a portion of the electrons back to the surface to enforce the space-charge limit. To determine how *warm* the emission is, the ratio of the temperature of the emitted electrons at the surface to the temperature of the emitted electrons at the sheath edge is utilized, which is referred to as γ. A larger γ denotes that the electrons are emitted with a higher finite temperature. To see the effect of temperature of the emitted electrons on space-charge limits, Equation 2.51 is plotted against Equation 2.58 for varying values of γ in Fig. 3.19 for helium.[18] Figure 3.19 shows that warm emission results in a higher space-charge limit than with cold emission. This trend makes sense because electrons emitted with a finite temperature will have more energy to help overcome the virtual cathode. Electrons emitted with a higher finite temperature result in a noticeably less restrictive space-charge limit. This shows the importance of characterizing the temperature of the emitted electrons with respect to the plasma electrons at the sheath edge.

[18]Helium is chosen for consistency with previous investigations of the sheath model [136]. It is to be noted that the emission is ion mass independent as shown in Equations 2.56 and 2.62.

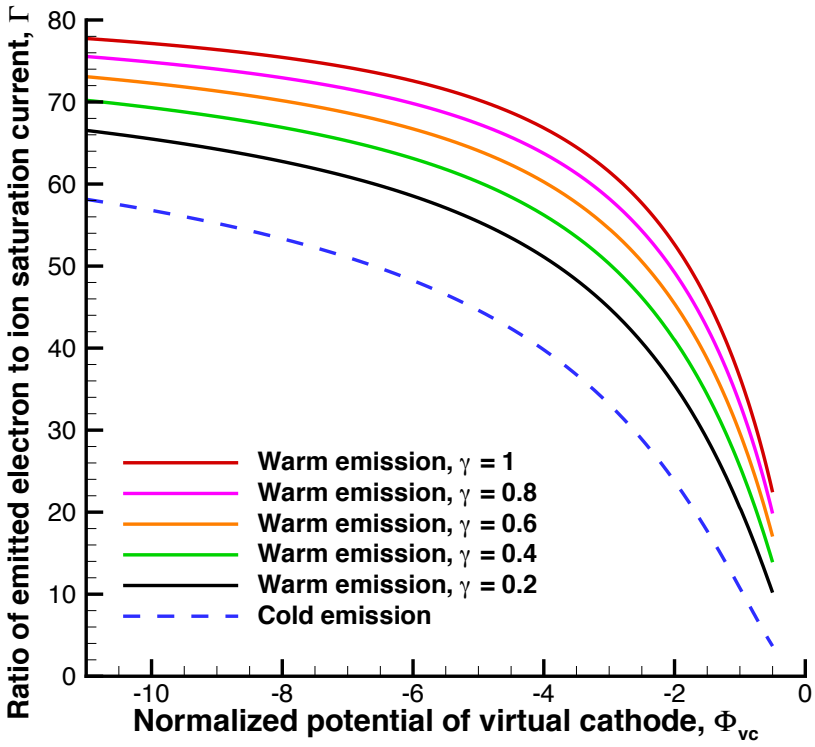

Figure 3.19: Cold vs. warm emitted electron temperature space-charge limited emission ($\gamma = T_{e,w}/T_e$).

A second important parameter for the sheath models for a biased surface is how to represent the electron temperature (T_e). The electron temperature is used to determine or normalize many of the sheath parameters such as the normalized sheath potential (Eq. 2.52), which the analytic models rely heavily upon. Given the importance of the electron temperature in determining the level of emission from the leading edge of the hypersonic vehicle, an approach is developed (see Appendix A) to approximate the electron temperature without solving for it explicitly. In the CFD solver, the electron temperature is assumed to equal the vibrational temperature. However, electrons emitted from the surface gain kinetic energy due to the sheath potential, which leads to an increase in electron temperature at the sheath edge. As shown in Figure 3.19, the ratio of emitted-to-plasma electron temperature plays an important role in space-charge limited current for the electron emission. Therefore, a modified electron temperature at the sheath edge is used, which includes the effect

of the emitted electrons. Figure 3.20 presents the ratio of emitted electron temperature to the plasma temperature at the sheath edge for various conditions typical of a hypersonic flow over a sharp leading edge. It is to be noted that the plasma (i.e. flow) temperature at the sheath edge equals the wall temperature, which is a valid assumption since few, if any, collisions occur within the sheath. The temperature of the emitted electrons is assumed to be the same as the wall temperature. For the cases of interest, the number density of the emitted electrons will be between one and two times the flowfield electron number density. A *small* wall bias (-1 V) and a *large* wall bias (-5 V) are investigated. A larger wall bias is not considered because it would significantly accelerate the flowfield ions into the wall, offsetting the cooling effect of electron emission, and the higher emission benefits from having a larger wall bias plateau in any case at higher biases (Fig. 3.19). As expected, higher wall biases result in higher electron temperatures at the sheath edge because the emitted electrons gain kinetic energy due to the sheath potential. The ratio of wall temperature to electron temperature at the sheath edge is on the order of magnitude to work where the electron temperature was explicitly solved for hypersonic test cases without ETC [144]. Approximating the electron temperature is important because it is used in many of the equations for ETC. For example, if it is assumed the electron temperature at the sheath edge equals the wall temperature, the normalized sheath voltage would be an overprediction, which has an important effect on space-charge limited emission (Fig. 3.19).

These different approaches are implemented into LeMANS to see if modeling the emission at a higher fidelity has an effect on the predicted surface properties. Figure 3.21 presents the surface temperature profiles for the baseline case of a 1 cm leading edge radius with a freestream velocity of 6 km/s at 60 km altitude. For the cases with space-charge limits accounted for, -1 and -5 V are chosen as the wall bi-

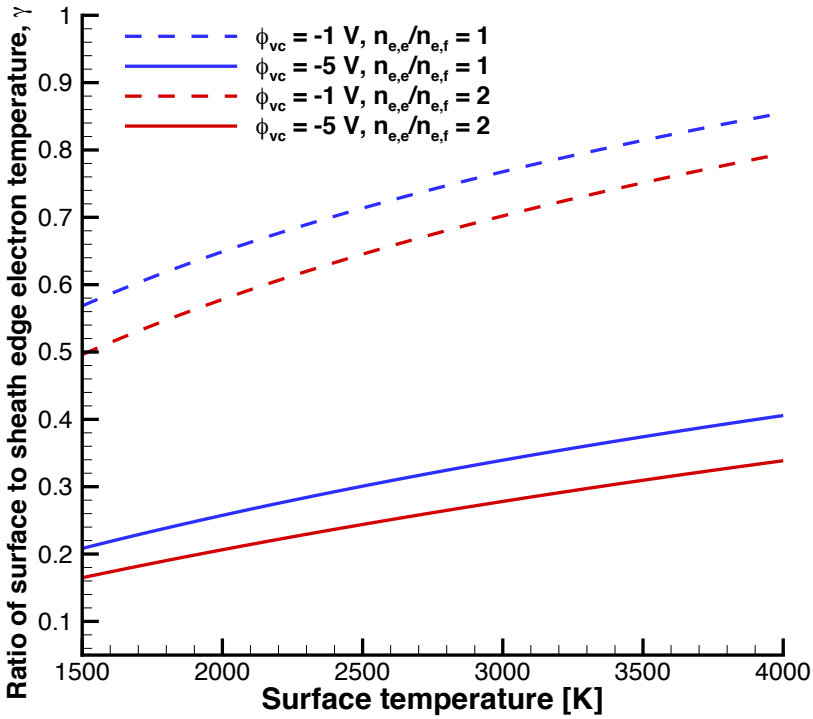

Figure 3.20: Ratio of emitted electron temperature to plasma temperature.

ases.[19] It is to be noted that in actuality the wall bias (i.e. the sheath potential) would be determined globally based on the flow conditions but are set as distinct values in this test case in order to investigate their effect. Future work is reserved for developing an approach to determine the sheath potential based on operating conditions instead of setting it to a discrete value, while this work focuses on the effect the bias has on emission even if its value is conceptual. The surface temperature profiles are shown in Figure 3.21(a) where the electron temperature is assumed to equal the wall temperature ($T_e = T_w$, $\gamma = 1$) in the analytic models. Similar to the electrically floating surface, the cases modeling plasma sheath physics are still space-charge limited and the saturated emission ETC surface temperature reductions are not realized, even with a biased surface. If space-charge limited emission (S-C-Limited ETC) is modeled assuming cold electron emission (Eq. 2.56), ETC results in approximately a 6% and 8% reduction in surface temperature at the leading edge for the -1 and -5 V

[19]If the emission is warm, -1 and -5 V are technically used as the virtual cathode values. See Figure 2.8.

biased surface cases, respectively. If space-charge limited emission is modeled assuming warm emission (Eq. 2.62), ETC results in approximately a 8% and 9% reduction in surface temperature for the -1 and -5 V biased surface cases, respectively. At least for this condition, whether the emission from the surface is modeled as cold or warm, it has minimal effects on the final surface temperature.

If the electron temperature approximation (Eq. 2.75) is used, the resulting surface temperature profiles are shown in Figure 3.21(b). The resulting surface temperatures are similar to the cases without the electron temperature approximation and usually slightly smaller. If space-charge limited emission (S-C-Limited ETC) is modeled assuming cold electron emission (Eq. 2.56), ETC results in approximately a 5% and 11% reduction in surface temperature at the leading edge for the -1 and -5 V biased surface cases, respectively. If the space-charge limited emission is modeled assuming warm emission (Eq. 2.62), ETC results in approximately a 8% and 14% reduction in surface temperature for the -1 and -5 V biased surface cases, respectively. If the magnitude of the surface bias is small (i.e. -1 V), the predicted surface temperature shows minimal differences from the cases without an electron temperature approximation. But for a larger magnitude of surface bias (i.e. -5 V), there is a noticeable difference in the results as the electrons are affected more by the bias, resulting in a higher electron temperature. A higher electron temperature has competing effects in the analytical models. For example, a higher electron temperature will result in a smaller normalized sheath potential (Eq. 2.52), which suggests the space-charge limit would be more restrictive. However, a larger electron temperature is also used to determine the space-charge limited current from the surface (Eqs. 2.56 and 2.62) and a higher electron temperature results in a less restrictive space-charge limited current. At least for this case, the higher electron temperature results in a less restrictive space-charge limit as the surface temperatures are reduced more for the temperature approximation case.

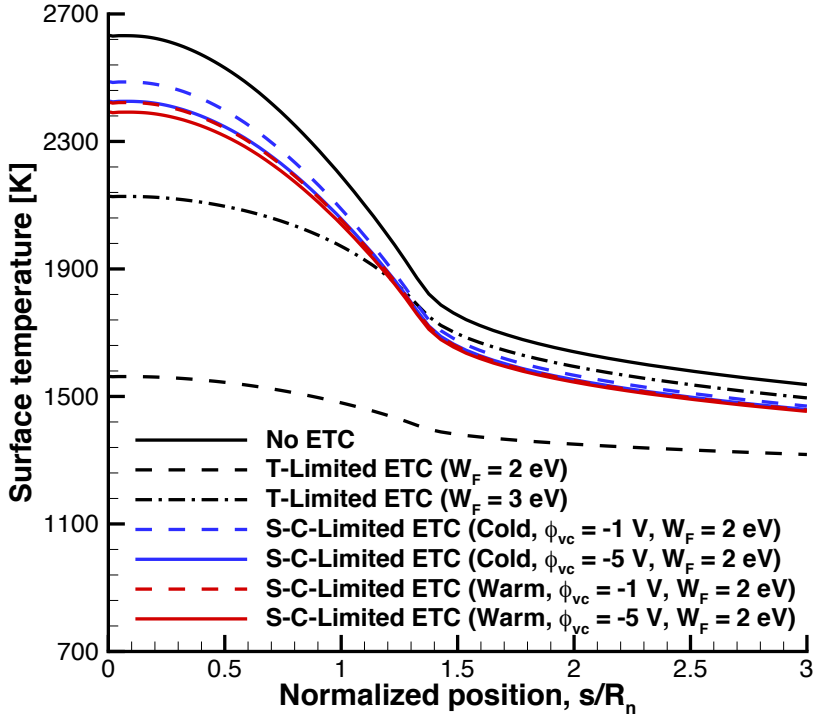

(a) Electron temperature equals surface temperature.

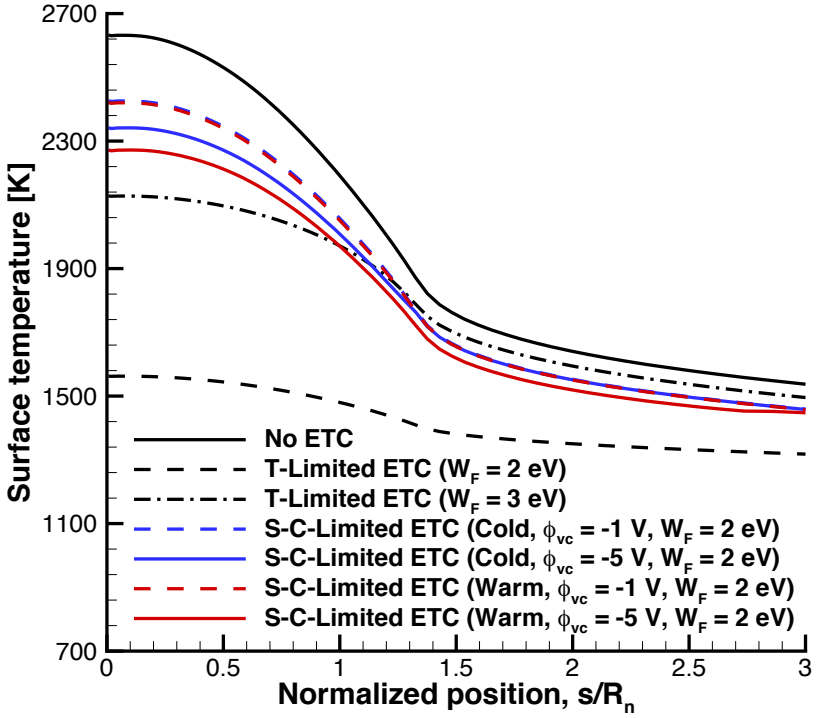

(b) Electron temperature approximation (Eq. 2.75).

Figure 3.21: Surface temperature and heat transfer profiles for the cases with saturated ETC at 6 km/s freestream velocity.

The resulting electron temperatures at the sheath edge are shown in Figure 3.22. The electrons are accelerated through the sheath, which results in a higher electron temperature. The electron temperature at the sheath edge for the cases with the largest magnitude of sheath bias, - 5 V, results in electron temperatures of 11,100 and 11,700 K ($\sim$ 1 eV) for the cold and warm emission cases, respectively. Having a higher electron temperature results in a smaller magnitude of the normalized potential of the virtual cathode, which the space-charge limited emission is sensitive to (Fig. 3.19). The resulting normalized potential of the sheath is presented in Figure 3.23. If the electron temperature at the sheath edge is assumed to equal the wall temperature, then the magnitude of the normalized virtual cathode potential is significantly overestimated, especially if the sheath is biased significantly (i.e. -5 V). For example, if the electron temperature is approximated, the normalized potential of the virtual cathode is near -5 but if the electron temperature at the sheath edge is assumed to equal the wall temperature, the normalized potential is nearly -25, which is a significant difference. Having a more accurate approximation for the electron temperature is important because it allows for important sheath parameters to be determined (γ, Φ_{vc}, and C_s) and thus all of the following results will use the electron temperature approximation as well as the warm emission theory unless otherwise noted. The warm emission theory is more applicable to ETC since the emission will rarely be perfectly space-charged.

The emission current density is shown in Figure 3.24(a), which shows how much the emission is limited by space-charge. The power required to *drive* the emission equals how much the sheath is biased with respect to the flow (ϕ_{vc}) multiplied by the emission current density and is shown in Figure 3.24(b). This is equivalent to the energy the emitted electrons gain between the surface and the flow by accelerating through the sheath (Eq. 2.71). A larger magnitude of biases results in higher levels of current but requires more power to *drive* the emission as expected.

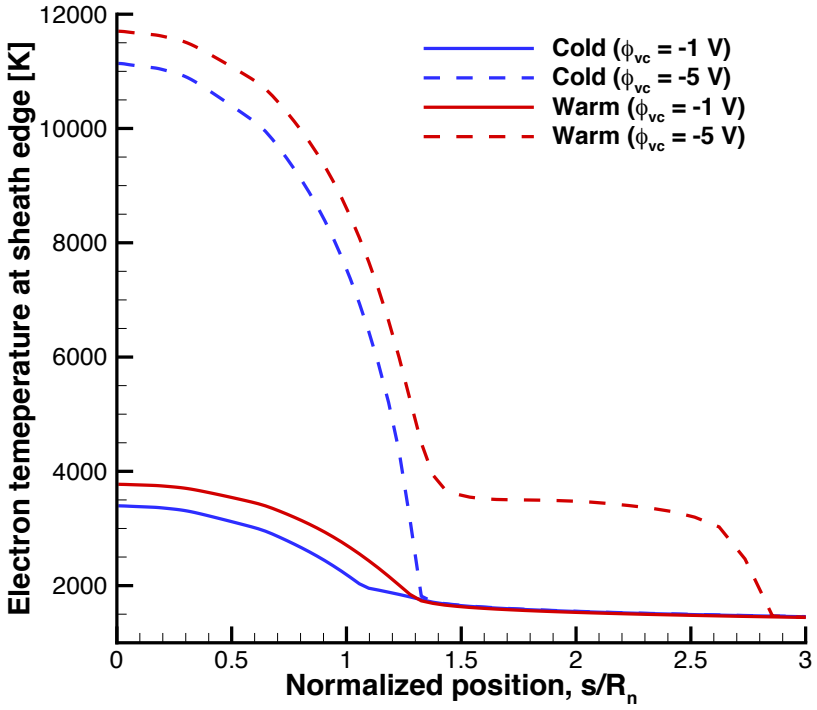

Figure 3.22: Electron temperature at sheath edge profiles for cold and warm emission cases.

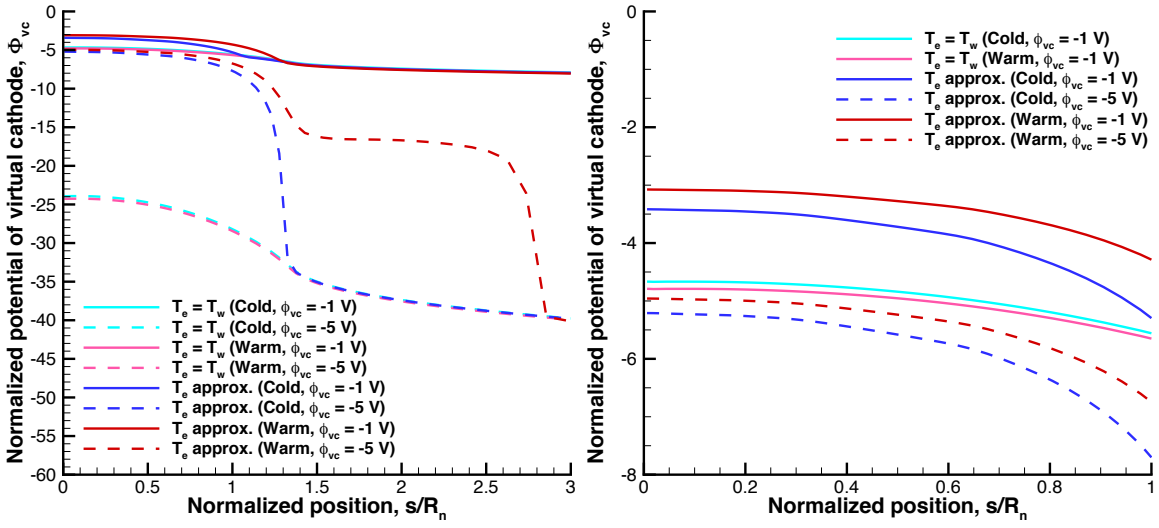

(a) Full view.

(b) Zoomed view.

Figure 3.23: Normalized potential of virtual cathode for cases with and without electron approximation.

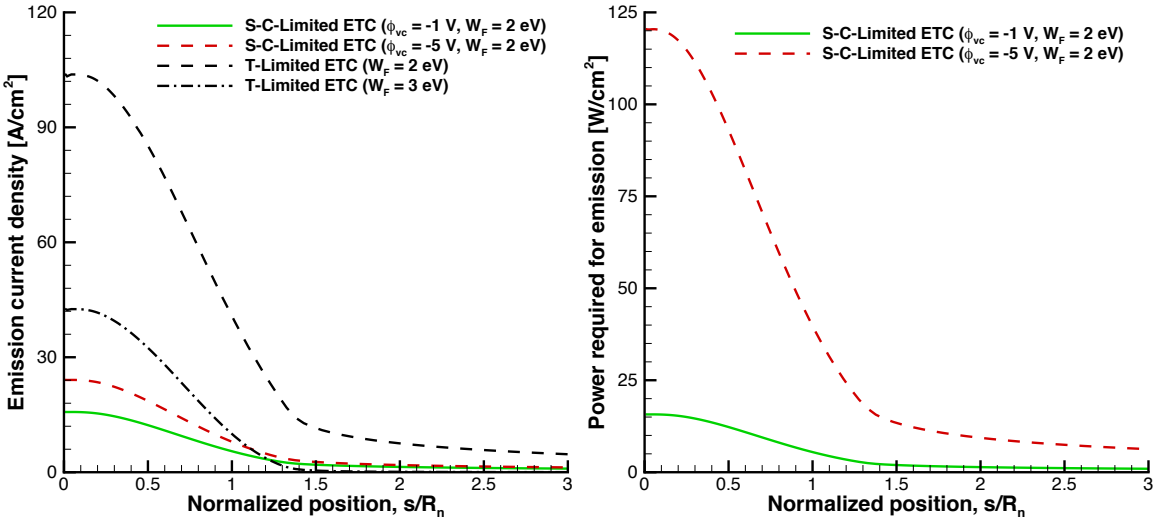

(a) Emission current density.

(b) Power required for emission.

Figure 3.24: Surface profiles for emission current density and power required for emission for space-charge limited negatively biased surface.

Having a biased surface as opposed to an electrically floating surface greatly complicates the modeling of ETC as it introduces an expanded set of parameters that are not well-characterized for leading edges of hypersonic vehicles largely because ETC is a new approach. One of the purposes of this study is to be able to determine if biasing the surface to allow a net charge through the sheath will make ETC more effective. For the baseline test case (i.e. 1 cm leading edge radius at an altitude of 60 km traveling at 6 km/s), biasing the surface does result in ETC being more effective at cooling the surface compared to an electrically floating surface. For the floating surface case, ETC only results in less than 3% reduction of the stagnation point temperature and for the biased surface cases, ETC results in a 8% and 14% reduction in temperature for the -1 and -5 V biases, respectively. Although this is a larger decrease in surface temperature it is still much less than the saturated emission surface reduction of 40% and the surface temperature remains relatively high. However, this is only for one trajectory point and as seen in Section 3.5, ETC behaves differently at varying conditions. For this reason, the test cases are once again extended to look at different parameters and how space-charge limits with a negatively biased surface

affect ETC.

Table 3.7 presents the stagnation point conditions for the same leading edge radius of 1 cm at 60 km altitude but includes slower and faster velocities. This table includes results from using two different biased potentials (ϕ_{vc}). It is to be remembered that this biased potential is normalized by the electron temperature at the sheath edge and then used in the sheath relations. The biased potential of negative infinity is a conceptual case where the biased potential is assumed to be infinite as derived by Equation 2.57. Although this magnitude of negative voltage is clearly unattainable, the results from using it provide insight in to whether even a higher voltage could allow the emission to overcome the space-charge limit or whether the emission will be restricted regardless based on flow conditions (e.g. level of ionization). It is to be noted that this theoretical -∞ case is modeled using cold emission theory[20] without the electron temperature approximation, whereas the cases with a finite bias are modeled using warm emission with the electron temperature approximation. This can result in the negative infinity case resulting in less emission than the -5 V case occasionally, especially if the -5 V case emission has already plateaued. Both cold and warm emission plateau similarly as shown in Figure 3.19 but warm emission reaches slightly higher levels of emission. Table 3.7 also provides the ideal material work function, which is the work function that would result precisely in the space-charge limited emission, if present. Finally, the table also includes the power required to *drive* the emission which is the emission current (J_e) multiplied by the bias of the surface (ϕ_{vc}).

For the slowest freestream velocity considered of 4 km/s, biasing the surface does not allow the emission to overcome the restrictive space-charges and results in negligible emission from the surface. This is even seen for the negative infinity bias case, which means that no matter how much the surface is biased, ETC will not be effective

[20]Since this limit was only easily obtainable using cold emission theory (Eq. 2.57).

at these conditions. However, for the higher velocity of 8 km/s, the biased surface overcomes space-charge limits and allows for the emission to reach saturation levels and results in a significant reduction in surface temperature. This is due to the higher number of charged flowfield species at the sheath edge for higher freestream velocities as shown in Figure 3.18. For this geometry and altitude, ETC is not effective for relatively low freestream velocities but reaches full effectiveness as the freestream velocity is increased to orbital speed.

Table 3.7: Stagnation point conditions for 1 cm leading edge radius at 60 km altitude including plasma sheath effects.

u_∞, [km/s]	ϕ_{vc}, [V]	T_w, [K]	% reduction vs. No ETC	% increase vs. saturated ETC[a]	$\frac{J_{e,sc}}{J_{e,T}}$	Ideal W_F [eV]	Power required [W/cm^2]
4	No ETC	2020	-	-	-	-	-
	-1	2030	+0.5	38	$\sim$0	N/A	0
	-5	2030	+0.5	38	$\sim$0	N/A	0
	-∞	2030	+0.5	38	$\sim$0	N/A	N/A
6	No ETC	2630	-	-	-	-	-
	-1	2420	8	52	0.24	3.5	25
	-5	2270	14	43	0.42	3.2	217
	-∞	2380	10	50	0.29	3.6	N/A
8	No ETC	3120	-	-	-	-	-
	-1	1660	47	0	1	2	230
	-5	1660	47	0	1	2	1150
	-∞	1660	47	0	1	2	N/A

[a] Compared to saturated emission with a work function of 2 eV.

A larger leading edge radius of 10 cm is also considered to evaluate the effect of leading edge radius on space-charge limited emission with a biased surface. Table 3.8 presents the results and once again the 4 km/s case is very space-charge limited. However, as shown for the corresponding saturated case in Table 3.4, ETC was already not that effective for this leading edge shape and velocity with stagnation point temperature decrease of 5%. If the freestream velocity is increased to 6 km/s or higher, the ionization in the flow increases enough for the emission to overcome space-charge

limits and the temperature reduction reaches saturation predicted benefits. Since the 6 km/s case is not space-charge limited for this case but is for the smaller leading edge of 1 cm, this shows a leading edge smaller than 10 cm but larger than 1 cm would be appropriate for the velocity at this altitude if space-charge limits are to be avoided. However, a larger radius results in more drag (Eq. 1.1).

Table 3.8: Stagnation point conditions for 10 cm leading edge radius at 60 km altitude including plasma sheath effects.

u_∞, [km/s]	ϕ_{vc}, [V]	T_w, [K]	% reduction vs. No ETC	% increase vs. saturated ETC[a]	$\frac{J_{e,sc}}{J_{e,T}}$	Ideal W_F [eV]	Power required [W/cm^2]
4	No ETC	1350	-	-	-	-	-
	-1	1370	+1.5	7	0.18	2.4	0.5
	-5	1360	+0.7	6	0.34	2.3	4.4
	-∞	1370	+1.5	7	0.18	2.4	N/A
6	No ETC	1730	-	-	-	-	-
	-1	1390	20	0	1	2	12.5
	-5	1390	20	0	1	2	63
	-∞	1390	20	0	1	2	N/A
8	No ETC	2100	-	-	-	-	-
	-1	1490	29	0	1	2	45
	-5	1490	29	0	1	2	227
	-∞	1490	29	0	1	2	N/A

[a] Compared to saturated emission with a work function of 2 eV.

A smaller leading edge radius is also considered. Similar to the saturation emission investigation, in order for the modeling approach (i.e. continuum approximation) to be still valid, this investigation must be performed at a lower altitude. An altitude of 30 km is chosen and the baseline geometry of 1 cm leading edge radius is considered first with the results in Table 3.9. Similar to all the previous conditions, the 4 km/s case is still greatly space-charge limited. However, as the freestream velocity is increased the space-charge limits are less restrictive. For example, for the 6 km/s case the emission is still slightly space-charge limited with -1 V but if the surface bias is -5 V the emission reaches saturation level emission as it does for the 8 km/s

freestream velocity case for both surface biases. This is due to the larger density of flow at this altitude, which corresponds to more charged species in the flowfield as well. This shows that ETC can be more effective at lower altitudes, although lower altitudes also correspond to larger drag (Eq. 1.1). The results of the smaller leading edge radius of 1 mm are provided in Table 3.10. The results show similar trends as the 1 cm leading edge radius. The emission is space-charge limited for the slowest velocity but as the velocity is increased saturation level emission is obtained, which shows ETC can be an effective approach for thermal control at this altitude.

Table 3.9: Stagnation point conditions for 1 cm leading edge radius at 30 km altitude including plasma sheath effects.

u_∞, [km/s]	ϕ_{vc}, [V]	T_w, [K]	% reduction vs. No ETC	% increase vs. saturated ETC[a]	$\frac{J_{e,sc}}{J_{e,T}}$	Ideal W_F [eV]	Power required [W/cm^2]
4	No ETC	2710	-	-	-	-	-
	-1	2720	+0.4	66	0.05	4.3	11
	-5	2690	0.7	64	0.08	4.1	96
	-∞	2700	0.4	65	0.06	4.2	N/A
6	No ETC	4220	-	-	-	-	-
	-1	2820	33	58	0.65	3.5	605
	-5	1790	58	0	1	2	4650
	-∞	2380	44	33	0.81	2.8	N/A
8	No ETC	5450	-	-	-	-	-
	-1	1920	65	0	1	2	2430
	-5	1920	65	0	1	2	12,200
	-∞	1920	65	0	1	2	N/A

[a] Compared to saturated emission with a work function of 2 eV.

As shown in this section, space-charge limits play an important role in the level of emission from the vehicle surface greatly impacting ETC performance on leading edges of hypersonic vehicles. If the surface is electrically floating, the emission is greatly limited, especially at lower freestream velocities. However, if the surface is biased or electrically connected to the collecting surface, space-charge limits are less

Table 3.10: Stagnation point conditions for 1 mm leading edge radius at 30 km altitude including plasma sheath effects.

u_∞, [km/s]	ϕ_{vc}, [V]	T_w, [K]	% reduction vs. No ETC	% increase vs. saturated ETC[a]	$\frac{J_{e,sc}}{J_{e,T}}$	Ideal W_F [eV]	Power required [W/cm^2]
4	No ETC	3380	-	-	-	-	-
	-1	3370	0.3	91	0.08	5.0	53
	-5	3290	3	87	0.13	4.7	460
	-∞	3330	1.5	89	0.11	4.8	N/A
6	No ETC	4870	-	-	-	-	-
	-1	2280	53	16	0.61	2.5	2170
	-5	1920	61	0	1	2	12,300
	-∞	1920	61	0	1	2	N/A
8	No ETC	6220	-	-	-	-	-
	-1	2070	67	0	1	N/A	6920
	-5	2070	67	0	1	N/A	34,600
	-∞	2070	67	0	1	N/A	N/A

[a] Compared to saturated emission with a work function of 2 eV.

restrictive. However, these limits still can hinder ETC on lower velocities and higher altitudes. This shows that ETC is more effective for not only hotter surfaces as shown in Section 3.5 but also when there are more charged species present in the flowfield.

3.7 Electric field effects

The numerical results presented in the previous sections are calculated assuming that the flow is charge neutral outside the plasma sheath. This is generally an appropriate assumption because the plasma sheath by definition is the only non-neutral region where the quasineutral flowfield is connected to the charged surface. However, electron emission from the surface introduces a charge imbalance near the vehicle as can be seen in Figure 3.10 for the saturated emission case. Space-charge limit results can reduce the amount of emission escaping the plasma sheath as discussed in Section 3.6. However, even with space-charge limits there is still is a charge imbalance at the sheath edge as shown in Figure 3.25. This charge imbalance, while significantly

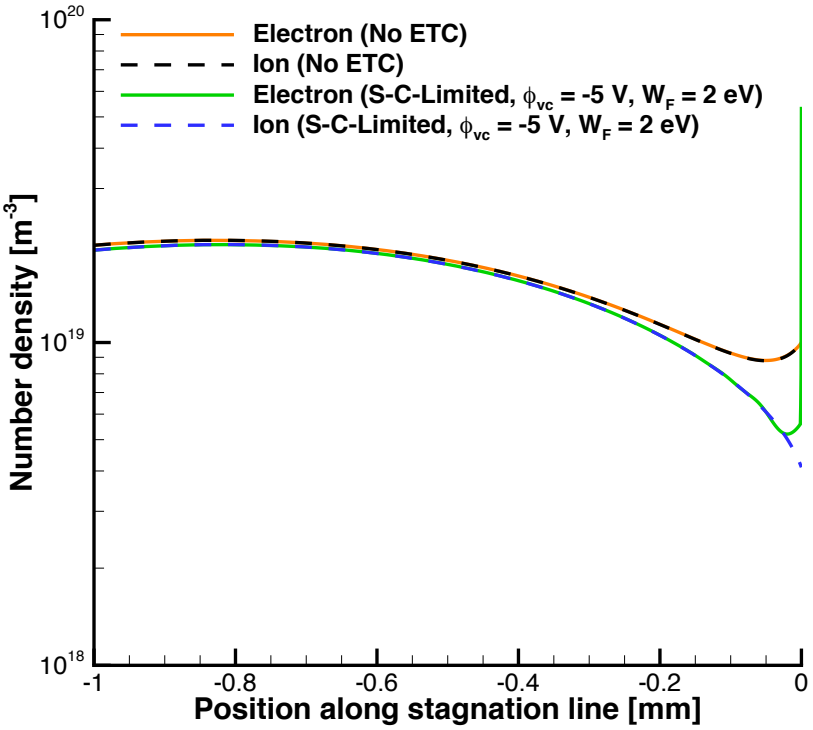

Figure 3.25: Charged species number densities along the stagnation streamline for space-charge limited emission.

smaller than the charge imbalance resulting from the saturated emission case, can produce an electric field that may influence the ionized flow around the hypersonic vehicle and change the cooling effect of ETC. It is to be noted that the results for this section are for a single trajectory point: 6 km/s freestream velocity at 60 km altitude and a leading edge radius of 1 cm. For the cases with ETC, the emission is modeled including plasma sheath effects where the space-charge limited emission is modeled as warm and the electron temperature approximation is used.

The electric field approximations discussed in Section 2.3 are implemented into the CFD framework and the results are as follows. The calculated electrical conductivity profiles in the flowfield are shown in Figure 3.26(a), where the top half corresponds to no ETC and the bottom with ETC. The conductivity of the flow is strongly related to the temperature of the flowfield, since the electrical conductivity is highest in the near post-shock region before decreasing gradually downstream. The differences

between the case with and without ETC are seen more clearly along the stagnation streamline, which is shown in Figure 3.27(a). The electrical conductivity is largely unchanged with ETC due to the temperature of the flowfield being largely unchanged (Fig. 3.9) and the model used for electrical conductivity being strongly dependent on temperature (Eq. 2.26). ETC will have a larger effect on the electron temperature of the flow as discussed in Section 2.5, which is not explicitly solved for in this work and could impact the flow conductivity to a greater degree. Nonetheless, differences still arise in the conductivity near the surface due to this being the region where the temperature is most affected by ETC and also the model being dependent on electron number density, which changes greatly with ETC (Fig. 3.10). The calculated electrical potential profiles in the flowfield are shown in Figure 3.26(b), where the top half corresponds to no ETC and the bottom with ETC. For the case without ETC, the flowfield is all at the same potential, which means the electric field of the flowfield is zero since the electric field is the gradient of the potential (Eq. 2.21). For the case with ETC, gradients of the potential are still relatively small resulting in a weak electric field. The electric potential profiles along the stagnation streamline without and with ETC are shown in Figure 3.27(b). The case without ETC shows a negligible change of the electric potential along the stagnation streamline. The case with ETC shows a small change in electric potential near the surface, which induces an electric field. The absolute value of the electric potential is less important since it is largely dependent on the boundary conditions. So although without and with ETC result in markedly different electric potentials their gradients, and thus electric fields, are similar.

The electric potential surface profiles are provided in Figure 3.28(a). For the case without ETC, the electric potential at the surface is determined by Equation 2.27 that was derived assuming the flowfield ion and electron fluxes are equal at the surface. For the case with ETC, the sheath edge is treated as the wall boundary condition

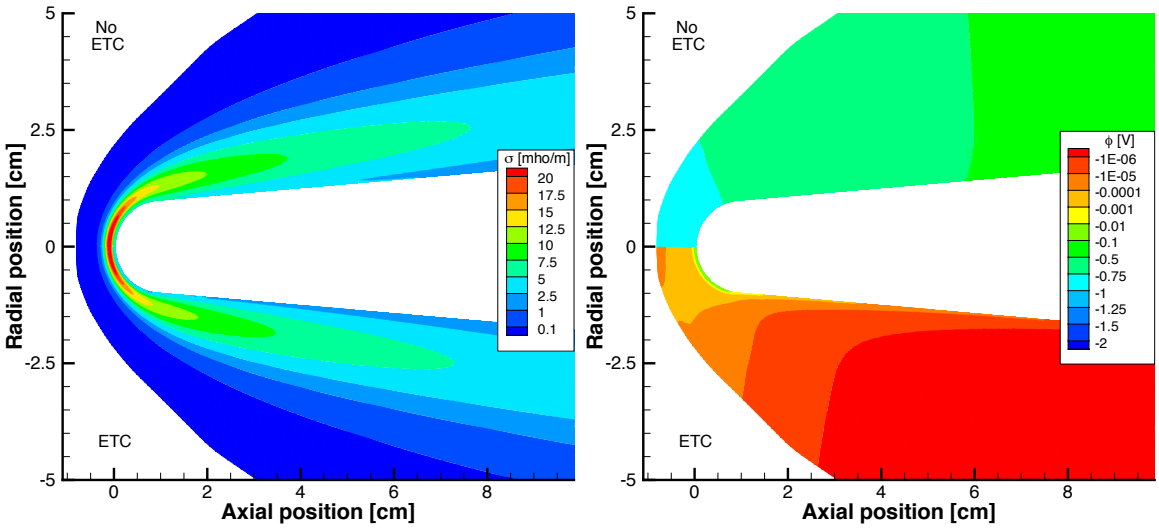

(a) Electric conductivity. (b) Electric potential.

Figure 3.26: Electric conductivity and potential contours for cases without (top) and with ETC (bottom).

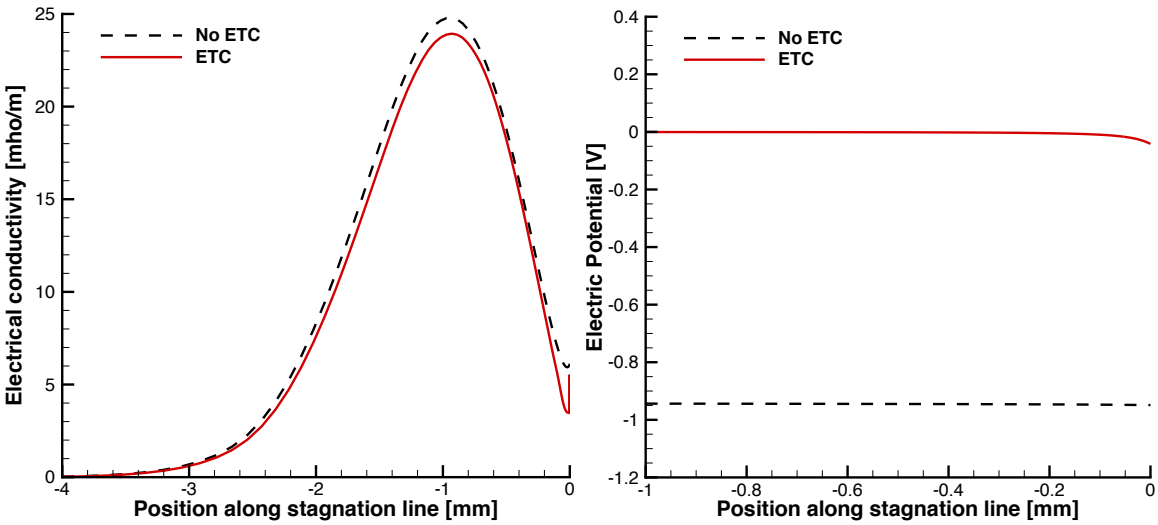

(a) Electric conductivity. (b) Electric potential.

Figure 3.27: Electric conductivity and potential profiles along stagnation streamline without and with ETC.

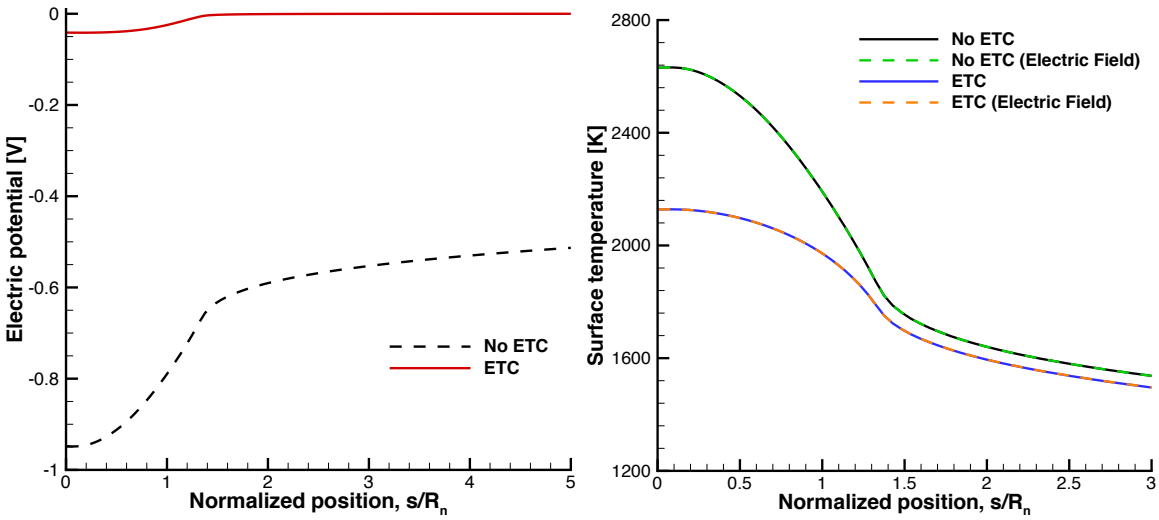

(a) Electric potential.

(b) Temperature.

Figure 3.28: Electric potential and temperature surface profiles for the cases including electric field effects.

since the sheath models utilized represent the physics between the sheath edge and the surface. The sheath edge potential is estimated by Equation 2.74. Although at different absolute values, the surface potentials follow similar shapes along the surface.

Finally, given the focus of the surface temperatures of the leading edges in this work, the effect of including electric field has the surface temperature profiles is shown in Figure 3.28(b). The results show that the calculated electric field has almost no effect on the surface temperature for both the case without ETC and the case with ETC. These results suggest that the calculated electric field is too small to change the underlying physics of the thermionic emission for the conditions considered in this study. However, more work is needed to increase the physical accuracy of the electric field modeling because the current approach is approximate. A higher fidelity of electric field modeling will better represent how the emitted electrons move in the flowfield, which is an important aspect to ETC (i.e. how the electrons move downstream and where they reattach?) and is reserved for future work.

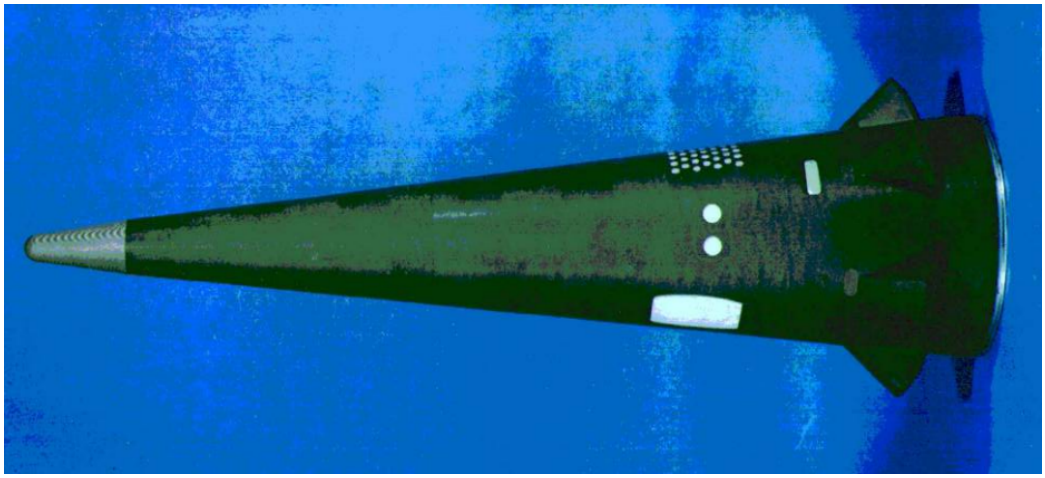

Figure 3.29: IRV-2 vehicle geometry with nose shown in grey. Figure from *Sandia National Laboratories*.

3.8 Surface conduction effects

The numerical results presented in the previous sections did not allow for heat to conduct into the material and only considered steady-state. This section considers how heat conducting into the material will affect ETC and its corresponding cooling benefits. The geometry utilized for the surface conduction investigation is slightly different than the previous geometries investigated. The geometry of the test case is based on the IRV-2 vehicle nose shape [167]. The nose radius of the geometry is 1.905 cm with an 8.42 deg. cone angle as shown in Figure 3.29. This geometry is used because it is typical of a sharp leading edge for a hypersonic vehicle and computational grids have already been generated for both the flow and material, and the grids were verified in a previous study [146]. Previous ETC studies have used a 2D planar wedge with a 1 cm leading edge radius and 5 deg. wedge angle so the grids are scaled down to match a 1 cm nose radius and will be used as a 2D planar wedge instead of an axisymmetric cone. The computational domain and boundary conditions are shown in Fig. 3.30.

Simulations are performed using MOPAR for the conditions of interest mentioned in Section 3.2 without ETC implemented. The baseline case of 1 cm leading edge

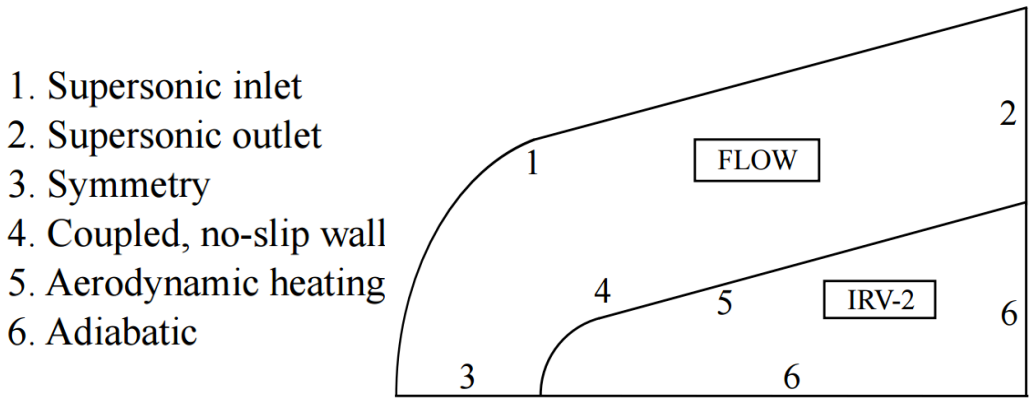

Figure 3.30: The computational domain and boundary conditions for simulations.

radius flying at 6 km/s at an altitude of 60 km is investigated. The purpose of the simulations is to assess the effect in-depth surface conduction has on surface temperature and determine typical in-depth surface heat transfer profiles for the test cases of interest. Figure 3.31 presents the surface temperature profiles for different thermal conductivities, heat capacities, and durations of flight. It is to be noted that the initial temperature of the entire material is assumed to equal 300 K. Similar trends are seen in surface temperature profiles for both thermal conductivities. The cases with the largest specific heat capacity (1200 J/kg/K) and shortest flight duration (5 seconds) result in the lowest surface temperature. This trend is expected since it takes more heat for a material with a larger specific heat capacity to heat up. For example, it takes twice as long for the 1200 J/kg/K case (10 seconds) to match the 600 J/kg/K case (5 seconds). The lower conductivity results in higher surface temperatures compared to the higher thermal conductivity. This is because the lower conductivity conducts heat into the surface at a slower rate resulting in a higher amount of heat staying near the surface, raising the surface temperature.

The in-depth material surface conduction heat transfer profiles are shown in Figure 3.32. For both thermal conductivities, the shortest durations result in the highest conduction of heat into the material. This is due to the limited time for the heat to conduct into the material, resulting in large temperature gradients within the mate-

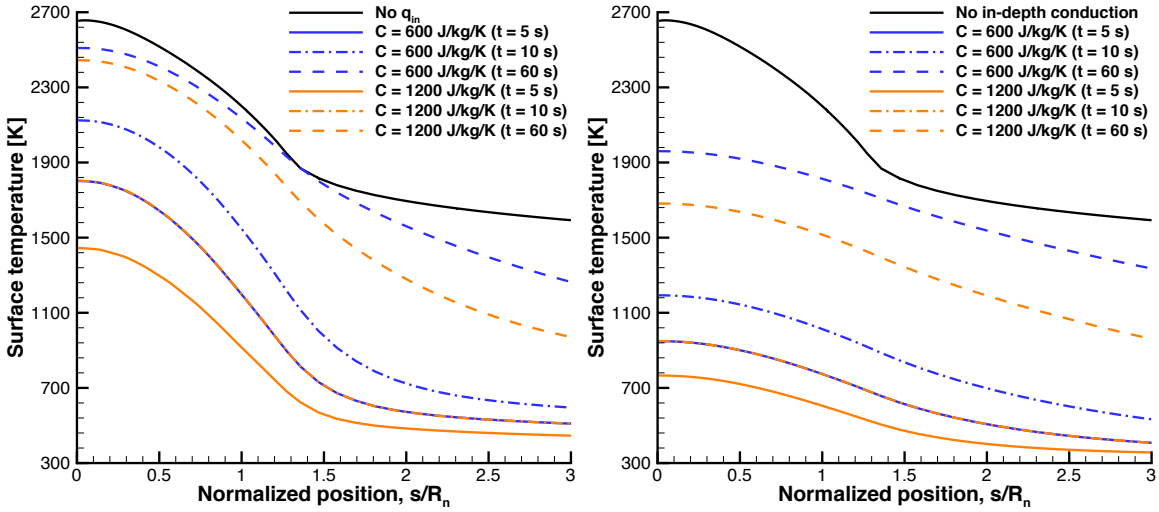

(a) Thermal conductivity = 10 W/m/K. (b) Thermal conductivity = 80 W/m/K.

Figure 3.31: Surface temperature profiles with in-depth surface conduction and without ETC.

rial driving the higher heat flux due to Fourier's law. As the duration of the flight is lengthened, the surface conduction heat flux is reduced. As expected, a higher thermal conductivity results in a higher surface conduction as shown in Figures 3.32(a) and 3.32(b). A larger material specific heat capacity of the material results in the material needing more energy to heat up so it stays at a cooler temperature longer compared to a material with a smaller specific heat capacity. This cooler surface lends itself to larger temperature gradients and thus higher in-depth surface conduction.

ETC modeling is implemented in the MOPAR-LeMANS coupling as discussed in Section 2.6 with the same conditions as above without ETC. ETC is modeled including space-charge limits and the resulting surface temperature profiles are shown in Figure 3.33. For each case, the surface temperature is noticeably reduced with ETC. Without ETC, the convective heating is balanced by radiative cooling and in-material conduction. But if ETC is included, it is the third mode of heat transfer away from the surface effectively reducing the heat load on the surface, which results in lower surface temperatures. For the hottest surface temperature case with in-depth surface conduction but without ETC (lowest specific heat capacity and thermal

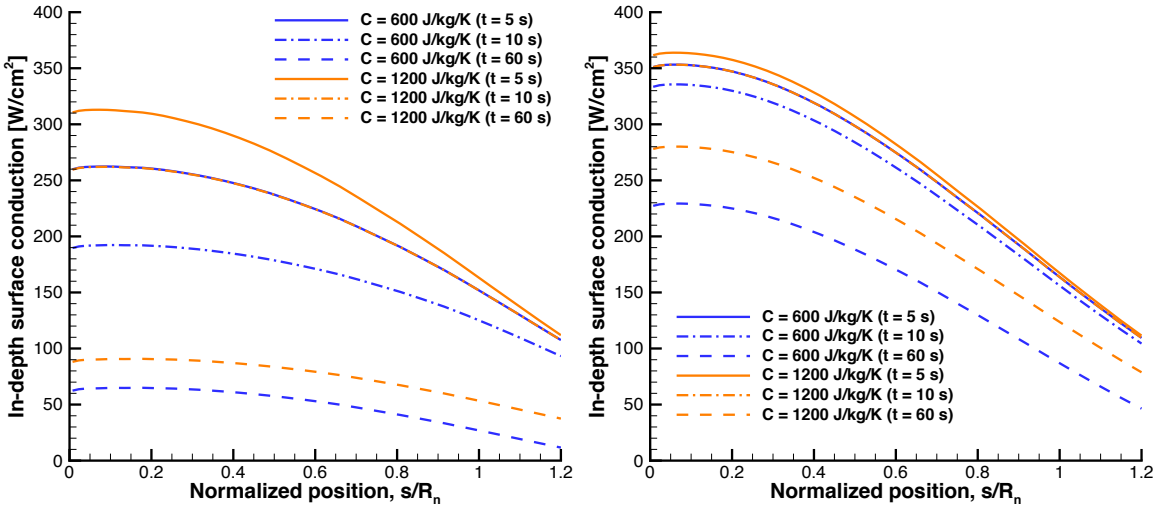

(a) Thermal conductivity = 10 W/m/K.

(b) Thermal conductivity = 80 W/m/K.

Figure 3.32: Surface temperature and heat transfer profiles for the cases with saturated ETC at 6 km/s freestream velocity.

conductivity but for longest duration), the stagnation point temperature is 2520 K. However with ETC, the stagnation point temperature is reduced by 27% to 1840 K. As shown in the results, ETC is more effective at lowering the surface temperature if the original surface is hotter, which is also the case for ETC without accounting for in-depth surface conduction. For example, for the coolest surface temperature case with in-depth surface conduction but without ETC (higher specific heat capacity and thermal conductivity but for the shortest duration), the reduction in the surface temperature is noticeable but still small as seen in Figure 3.33(b).

Figure 3.34 presents the contribution to heat flux away from the surface for the 1-minute duration cases. Since these three modes of heat transfer balance with the convective heat transfer, this figure shows which modes contribute the most to the heat flux away from the surface. For the low thermal conductivity case shown in Figure 3.34(a) and near the leading edge, radiative cooling is the dominant mode of heat transfer. This is verification that the emission is space-charge limited because Figure 2.1 shows that ETC should be more effective at this temperature range if saturated emission levels are reached. The heat transfer rate into the material is

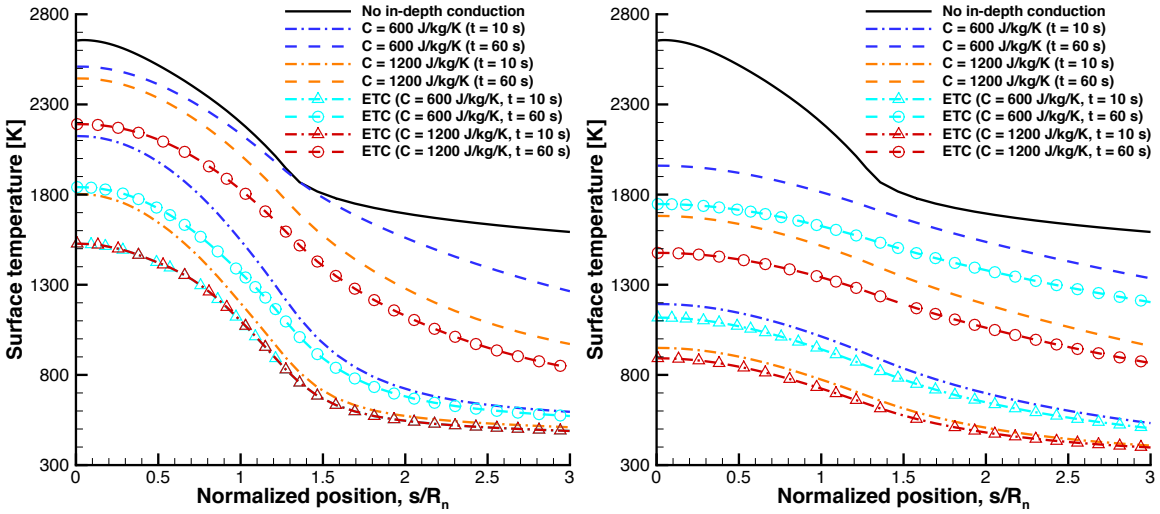

(a) Thermal conductivity = 10 W/m/K. (b) Thermal conductivity = 80 W/m/K.

Figure 3.33: Surface temperature profiles with in-depth surface conduction and with ETC.

similar to the rate of heat transfer into the flow provided by ETC. For the case with a high thermal conductivity shown in Figure 3.34(b), the heat transfer away from the surface is dominated by the heat transfer into the material. This is because the surface temperature is lower for these cases as shown in Figure 3.33(b), which result in ETC and radiative cooling being less effective since they are both strongly dependent on surface temperature. Nonetheless, at the stagnation point, ETC still contributes more to cooling the surface than radiative cooling.

The goal of modeling the in-material surface conduction was to assess the effect it has on ETC benefits. For the limited test cases investigated, ETC still provides similar cooling benefits as seen without accounting for in-material surface conduction and once again proves to be more effective at cooling hotter surfaces. Although this investigation is limited in scope, it still provides insight into how in-depth surface conduction affects ETC. Establishing this modeling framework will prove to be useful as ETC materials are continued to be developed and investigated. It will allow for exact ETC material properties to be included in the investigation, once characterized, and comparisons to future experiments to be more representative. Finally, it will also

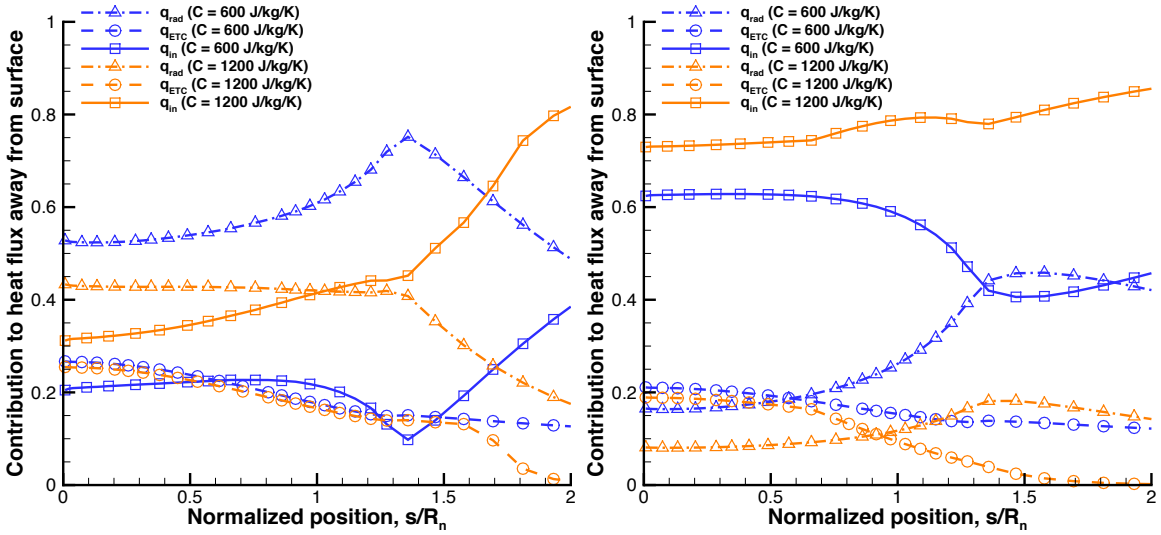

(a) Thermal conductivity = 10 W/m/K.

(b) Thermal conductivity = 80 W/m/K.

Figure 3.34: Contribution to heat flux away from the surface for the case with in-depth surface conduction, ETC, and 1 minute duration.

allow ETC to be investigated for certain flight envelopes instead of only one trajectory point at a time.

3.9 Assessment of Analytical Sheath Models

As mentioned in Section 3.6.2 analytical sheath models for negatively biased surfaces have been recently developed. The cold emission theory developed by Takamura et al. has been compared to a 1-D PIC simulation and a qualitative agreement is shown [136]. However, as discussed in Section 3.6.2, the warm emission model is more applicable to ETC on the leading edges of hypersonic vehicles and has not been assessed previously to this work and therefore an assessment is performed in this section using a DK solver.

A test case is evaluated using the DK solver with the parameters given in Table 3.11. The potential difference between the wall and the plasma boundary condition is prescribed as Φ_w and $\Gamma_{desired}$ is the prescribed ratio of electron emission current to injected ion current. Helium (4 amu) is chosen for the ion and γ is chosen

Table 3.11: Plasma sheath test case conditions.

Φ_w	$\Gamma_{desired}$	m_i [amu]	$\frac{T_e}{T_i}$	$\gamma = \frac{T_{e,w}}{T_e}$
-0.95	50	4	10	0.1

as 0.1 for consistency with the analytical model [136]. It is to be noted that the emission is ion mass independent as shown in Equations 2.56 and 2.62. The ratio of electron emission current relative to the ion current will be referred to as Γ. $\Gamma_{desired}$ is the amount of emission that would result if the emission is not space-charge limited and only limited by the surface temperature (i.e. saturated or Richardson emission). $\Gamma_{actual} < \Gamma_{desired}$ indicates that some of the emitted electrons from the surface return back to the surface before reaching the sheath edge, resulting in a reduction in the net emitted electron current. The ratio of electron to ion temperature is typical for that of a hypersonic flow [144]. This ratio is only used in the D-K simulations since the theory assumes cold ions.

The sheath potential structure is shown in Figure 3.35, where the potential is normalized by the electron temperature and the distance from the wall is normalized by the Debye length (x/λ_D). Figure 3.35 shows that the emission is space-charge limited because of the virtual cathode shown near the wall (at x = 0). The potential then increases before reaching a plateau (approximately $x/\lambda_D = 15$), which we define as the sheath edge in the present CFD simulations. The direct kinetic solver solves for the pre-sheath region where the ions are accelerated into the sheath as shown in Figure 3.35(a). However, as mentioned, the plateau region is used as the boundary condition in the CFD simulations so the structure is modified as shown in Figure 3.35(b). The Γ_{actual} for this case is 21.7, which is smaller than $\Gamma_{desired}$ since the emission is space-charge limited. Figure 3.36 shows the resulting velocity distribution function (VDF) for each species (ion, primary electron, and emitted electron) where

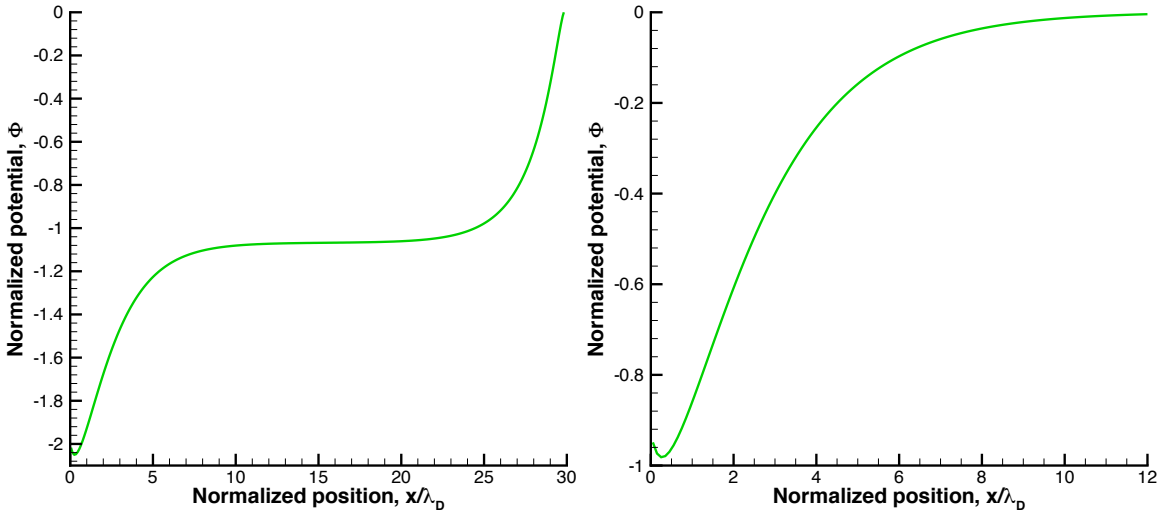

(a) Including pre-sheath.

(b) Without pre-sheath and adjusted so sheath edge is at zero potential.

Figure 3.35: Sheath potential structure.

the velocity is normalized by the ion acoustic speed. The theory assumes that the normalized velocity for ions equals unity where Fig. 3.36(a) shows that the normal velocity is closer to 1.5 for the D-K simulations. This motivated an extension of the theory to account for ion velocities greater than sonic as derived in Appendix B in order for a fair comparison to be made.

3.9.1 Comparison of theory and direct kinetic solver

The theory is evaluated using results obtained from the direct kinetic solver. Figure 3.37 shows a comparison between finite temperature theory (lines) and results from the direct kinetic solver (symbols). The different theory lines correspond to different ion speeds at the sheath edge (χ). The values of χ are chosen based on the D-K results (Fig. 3.36(a)). The values are typically between unity (Bohm criterion) and up to 2.5 in the present collisionless sheath simulation setup. The various symbols denote different electron to ion temperature ratios. For each D-K simulation at low amount of wall bias, the theory with ion speeds 1.75 times the acoustic speed agrees well. As the wall bias is increased in magnitude, the theory with larger ion speeds

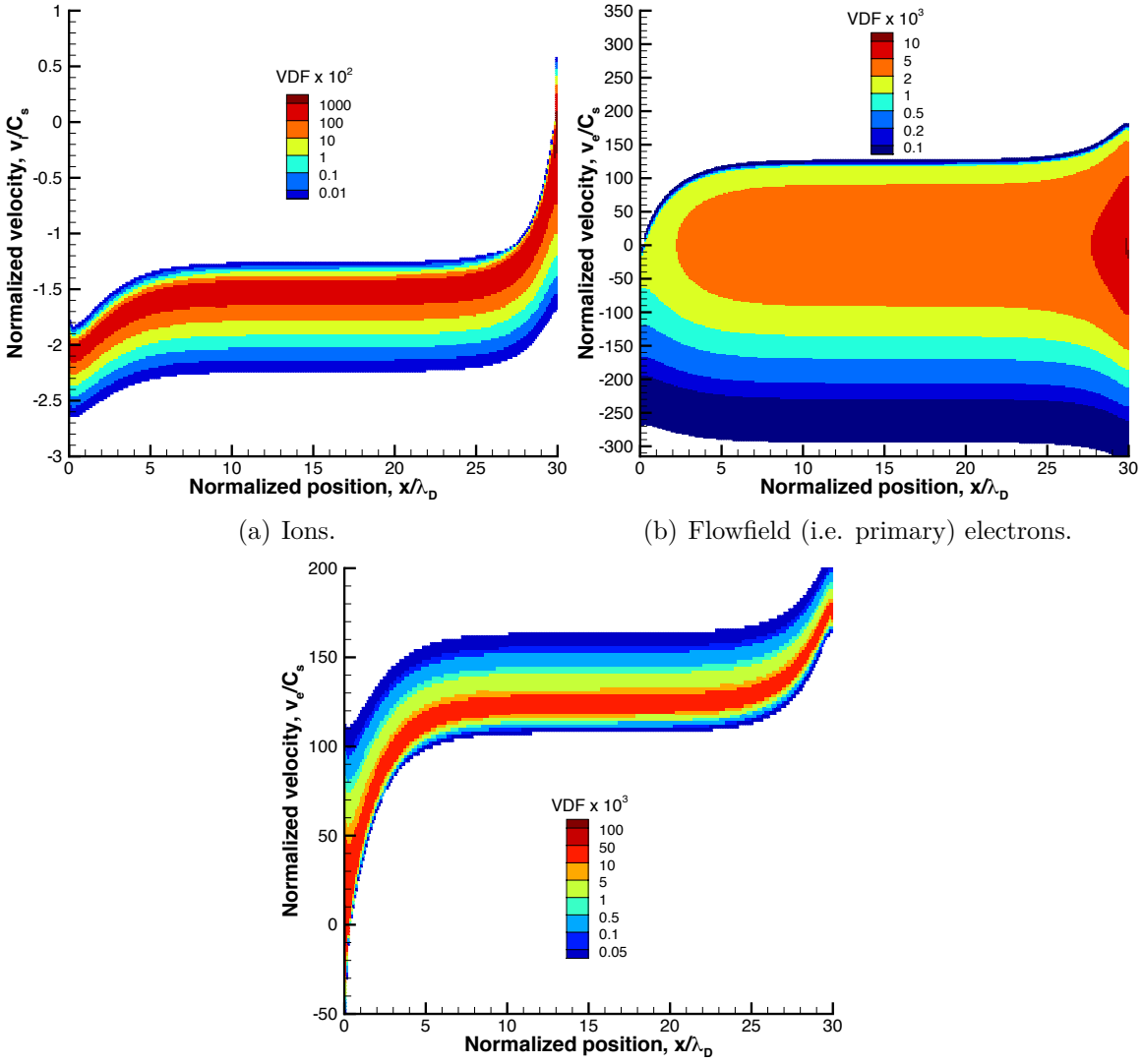

(a) Ions.

(b) Flowfield (i.e. primary) electrons.

(c) Emitted electrons.

Figure 3.36: Velocity distribution functions: x = 0 is the wall, $x/\lambda_D = 30$ is the plasma, and the sheath edge is at the plateau (i.e., $x/\lambda_D \approx 15$).

(2.5 times the acoustic speed) agrees well. This is expected because larger wall biases result in higher ion speeds at the plateau in the simulation domain, which is assumed to be the sheath edge. It is to be noted that for larger wall biases ($|\Phi_{vc}| \geq 4$) oscillations are present due to instabilities such as the two-stream instability caused by the high energy electrons accelerated by the large sheath potential. This phenomenon is also mentioned in Ref. [135]. For the cases with oscillations, the resulting emission is time-averaged. It is to be noted that the theory originally proposed by Takamura et al. does not take in to account any instabilities and unsteady phenomena, so the lowering of the Γ might be attributed to the unsteadiness. However, the results obtained from the D-K simulation do not exhibit any statistical noise, which inherently occurs in particle methods, and therefore, a more careful assessment of the theory is performed. If the ion speed is assumed to equal the ion acoustic speed ($\chi = 1$), the theory slightly underpredicts the amount of space-charge limited emission compared to the D-K simulations. As the wall bias is increased in magnitude, the theory overpredicts the space-charge limited emission given by the D-K simulations. This is a similar trend as the one seen in the 1D PIC comparison [136]. For the higher electron to ion temperature ratios (50 and 10), the theory matches the simulations better than those when the electron temperature equals the ion temperature. This is expected since the theory assumes cold ions ($T_i = 0$).

The goal of this work was to assess the accuracy of the sheath models implemented into LeMANS to model ETC using plasma sheath solver. The simulations agreed well with the warm emission theory of Takamura et al. for a low amount of wall bias. However, as the wall bias was increased, instabilities occurred in the simulations and they underpredicted the theory. The extended theory that includes supersonic ion velocities at the sheath edge agrees well with the simulations even for higher wall biases due to the direct-kinetic solver allowing for supersonic ion velocities, which justifies the use of Takamura's theory to be used in the CFD code.

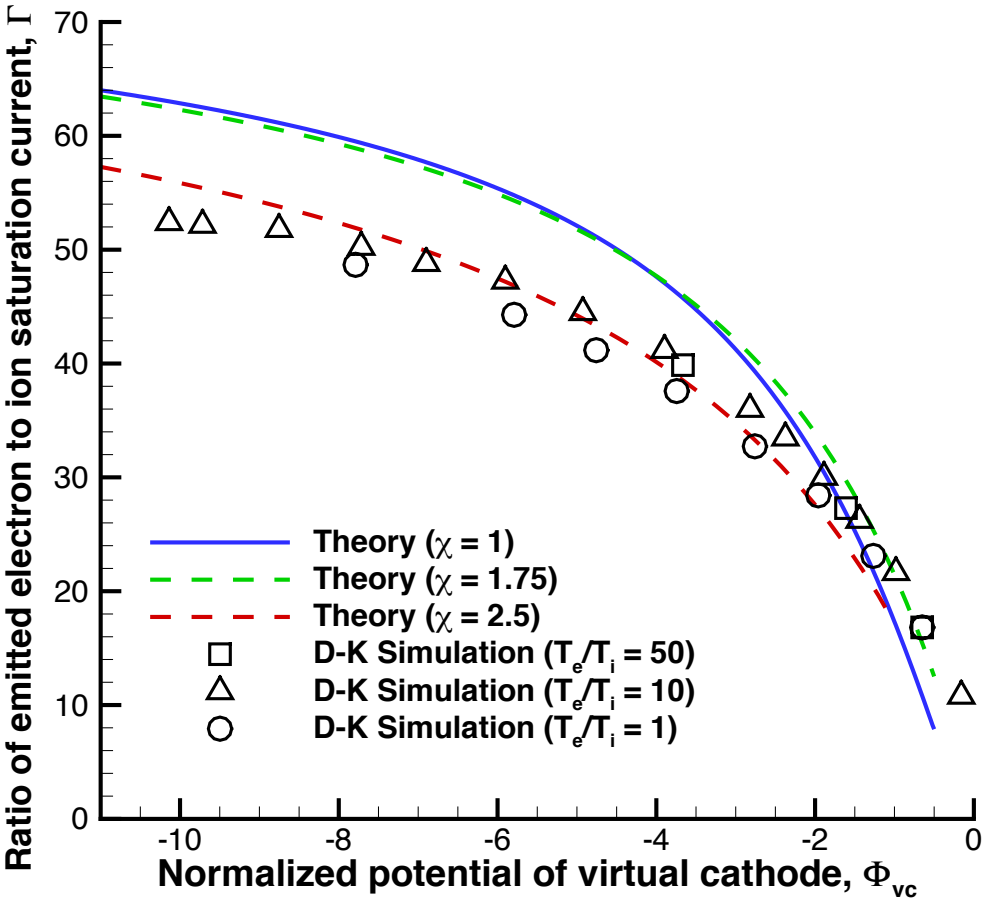

Figure 3.37: Comparison of the space-charge limited theory to Direct-Kinetic simulations ($\gamma = 0.1$).

3.10 Desired material properties for ETC

This chapter investigated an array of material properties that could impact how ETC performs. As mentioned in Section 3.5, the sharp leading edges of hypersonic vehicles will inherently be interacting with high-temperature flows. Since the aerodynamic heating of the vehicle is primarily driven by the temperature gradients between the flow and vehicle surface (i.e. convective heat transfer) as discussed in Section 2.1.1, lowering the surface temperature *and* lowering the convective heating rate is unattainable. Lowering the surface temperature will result in higher temperature gradients increasing the convective heat transfer (Fourier's law). Lower convective heating rates can be achieved by increasing the surface temperature but can lead to material degradation. High convective heating rates are tolerable as long as these rates are matched by proportionate ETC and radiative cooling rates, and the amount of heat allowed to conduct into the vehicle is minimized. This leads to two goals that an ideal ETC material would provide:

1. Maintain the surface temperature at operable conditions (i.e. minimize the surface temperature below the melting point of the material).

2. Limit the amount of heat that is conducted into the vehicle (i.e. minimize the in-depth material surface conduction).

Given that ETC materials are currently being developed, as discussed in Section 3.2.3, one purpose of this work is to help guide that development in determining how certain material properties affect ETC. This section will summarize how the material property affects ETC and suggest to what degree (i.e. low, high) it is desired to create an *ideal* ETC material for a sharp leading edge of a hypersonic vehicle.

3.10.1 Emissivity

The material emissivity (ϵ) determines how effective the material is at cooling the surface via radiative cooling as discussed in Section 2.1.1. Although Table 3.3 showed that ETC is more predominant for lower emissivities with saturated ETC, these large levels of electron emission are greatly reduced by space-charge limited ETC. However, even if these saturated levels of electron emission could be realized, cooling the surface more via emitting photons (i.e. radiation) than emitting electrons (i.e. ETC), presents less challenges due to the lack of charge neutrality introduced by ETC. Nonetheless, since radiative cooling and ETC complement each other, it is desired for radiative cooling to be as effective as possible, which means the surface should be as close to blackbody ($\epsilon = 1$) as possible.

3.10.2 Work function

The work function (W_F) determines how effective the material is at cooling the surface via ETC as discussed in Section 2.1.1. This is an important material property as it is used directly in the electron emission current density equation (Eq. 2.4). If the electron emission is assumed to equal saturation levels of emission as in Section 3.5, a low work function (e.g. 2 eV) is desired. However, if space-charge effects are accounted for as in Section 3.6, the desired work function becomes strongly dependent on the plasma conditions of the emissive surface (e.g. floating, biased) and vehicle operating conditions (e.g. freestream velocity, freestream density, leading edge shape). If space-charge limits are reached, ETC is most effective if the work function is small enough to exactly reach the space-charge limited current but large enough to retain a large potential barrier in the material for electrons to overcome to maximize the cooling benefits of the limited current (Eq. 3.1). In essence, the work function should be minimized until space-charge limits are reached.

3.10.3 Thermal conductivity

The thermal conductivity is essentially the rate at which heat passes through the material. The desired thermal conductivity depends on the objective on how to manage the heat that reaches the leading edge. A low thermal conductivity results in the heat staying near the leading edge for a longer duration, which results in the surface temperature being higher compared to a material with a high thermal conductivity as discussed in Section 3.8. This would be desired if the resulting surface temperature does not degrade the leading edge material and less heat would conduct into the vehicle. However, if this surface temperature degrades the leading edge material, it would be appropriate for the material to have a higher thermal conductivity that would conduct the heat away from the surface and into the vehicle at a higher rate. This would result in lower surface temperatures but the heat conducted into the vehicle would have to be managed.

3.10.4 Specific heat capacity

The specific heat capacity is the heat required to result in a temperature change of the material. A material with a high specific heat capacity would be desired as it would require more energy for the material to heat up. For example, it would take a longer flight duration for aerodynamic heating to be transferred into the vehicle compared to a material with a lower specific heat capacity. It is to be noted that if the flight duration is long enough, a steady-state will be reached where the material emissivity and work function will be the material properties affecting the surface properties.

3.11 Conclusions

This chapter presented the numerical results of a detailed investigation of ETC. First, test cases applicable to a leading edge of a hypersonic vehicle were presented, which included different geometries, freestream conditions, and material properties. The flowfield and surface features without ETC were then presented, which highlighted the thermally intense environment where ETC is possible to be applied. Then ETC was investigated assuming saturation levels of emission, which showed ETC can be very effective at cooling the surface, especially for a surface prone to high temperatures (high velocity, sharp leading edge, low altitude). This investigation, however, neglected plasma sheath effects, which were then investigated for two different types of emissive surfaces. If the emissive surface is electrically floating, ETC can be greatly limited to space-charge limits. Biasing the surface can alleviate the restriction of space-charge limits depending on the number of charged species in the flowfield. This resulted in ETC being more effective at higher velocities due to higher ionization of the flowfield but the lower velocities remained prone to space-charge limits. A highlight of this study was that ETC could decrease the stagnation point temperature by nearly 50% for a leading edge radius of 1 cm flying at orbital velocity at an altitude of 60 km. The effect of the electric field was studied in this chapter and although ETC induces a small electric field, it has negligible effects on the surface temperature. This chapter also included an investigation of the effects in-depth surface conduction has on ETC, which showed ETC is still effective at cooling the surface even if heat is allowed to travel into the surface. Finally, this chapter concluded with an assessment of the plasma sheath models utilized in the CFD code, which validated their use.

CHAPTER IV

Comparison with Experimental Data

4.1 Introduction

Chapter II introduced a modeling framework to investigate ETC using CFD and Chapter III presented numerical results using this method for conditions typical of hypersonic flight. However, as discussed in Section 1.1.2, while theory and numerical simulation are important to understanding how ETC will perform, in order to truly understand ETC, experiments must be performed to assess and validate both the theory and simulations. As motivated in Section 1.1.2, however, computer simulation is the starting point to investigating ETC and the modeling results will help design future experiments that both assess the modeling approach and help understand more of the underlying physics involved with ETC. Interesting trends introduced by the numerical results in Chapter III, such as if the emission is space-charge limited, having a larger work function can result in ETC being more effective at cooling, can be evaluated using experiments. Currently, there are no completed experiments to specifically investigate ETC but some are expected to occur in the near future.

Although using thermoelectric materials as a mechanism to reduce the thermal load on hypersonic vehicles is a recent approach, employing thermionic emission in high-speed flight is not a novel concept. In the 1960s there was a push to use thermoelectric materials on the nose of re-entry vehicles and collect the emitted electrons as

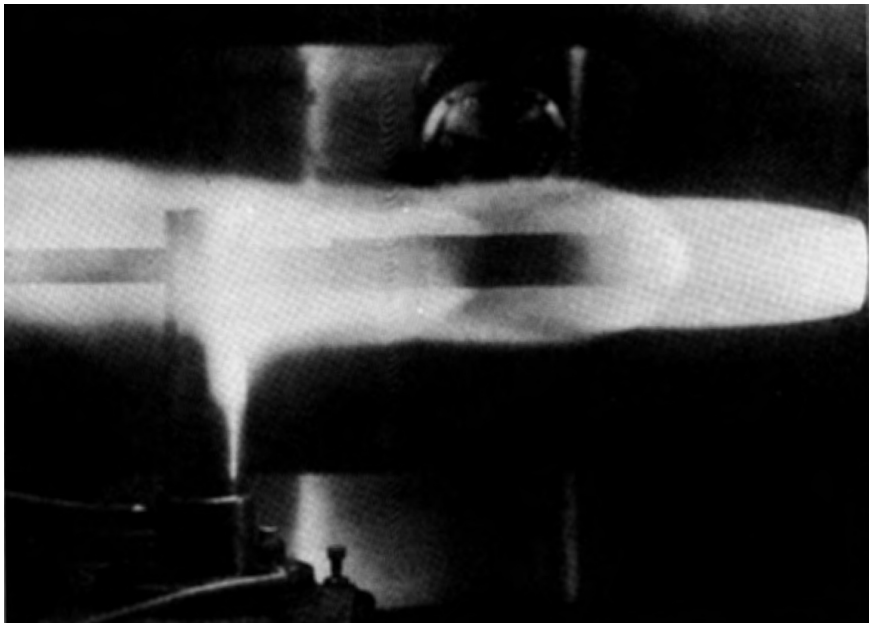

Figure 4.1: A hypersonic plasma converter tested in plasma arc tunnel. Figure from Sandia Corporation.

a source of power generation [69, 70]. Experiments were performed using the plasma arc tunnel at the Sandia Corporation using a range of different flow conditions, emissive materials, and geometries [71]. An image of the hypersonic plasma generator tested in the plasma arc tunnel is shown in Figure 4.1. Although the conditions of the experiments do not precisely duplicate the conditions investigated in Chapter III, comparing the modeling approach to them can still provide valuable conclusions. This study aims to assess the CFD modeling approach using these experiments.

4.2 Test case description

The experiments of Touryan were performed in Sandia Corporation's plasma arc tunnels in the 1960s. A detailed description of the experiments is given in Refs. [69, 71]. The experiments investigated the effect of different geometries, freestream conditions, and emissive materials on thermionic emission and the resulting power generation.

4.2.1 Geometry

The experiments investigated a diverse range of plasma generator shapes as shown in Figure 4.2. However, results for only two of the geometries were reported, denoted S-6 and S-30. The S-30 geometry has a sharper nose radius but a larger emitter area. The S-6 geometry is an axisymmetric cone with a 0.73 cm leading nose radius, followed by a 10-degree-angle wedge, a cylinder region, and a 6-degree-angle wedge as shown in Figure 4.3. The geometry is split into two regions, the emitter and collector region. The emitter region usually consists of a material with a lower work function than the collector region in order to promote the collecting surface to being more susceptible to electron recombination. This concept of electrons recombining on a collecting surface on the aft-body of the geometry is also a concept that will be investigated for ETC as shown in the schematic in Figure 2.10, although modeling it is reserved for future work. The emitter region surface area is 8.4 cm^2 consisting of the leading nose radius and the 10-degree-angle conical body. For this work, the emitter and collector regions are made of the same material (graphite). The S-30 geometry is an axisymmetric cone with a 1.0 mm leading nose radius, followed by a 13.5-degree-angle conical body as shown in Figure 4.4. The whole geometry is considered the emitter region and has a surface area of 16 cm^2. The material used for this geometry is tungsten. Both of these geometries are comparable to the geometries investigated in Chapter III.

Meshes are generated for both geometries, and a grid convergence study revealed that the solution is grid-independent for these meshes using a similar approach as discussed in Chapter III. The computational grid used for the S-6 geometry is axisymmetric and composed of approximately 21,000 cells, with 130 cells in the axial direction and 160 cells in the radial direction. The computational grid used for the S-30 geometry is also axisymmetric and composed of approximately 28,000 cells, with 154 cells in the axial direction and 180 in the radial direction.

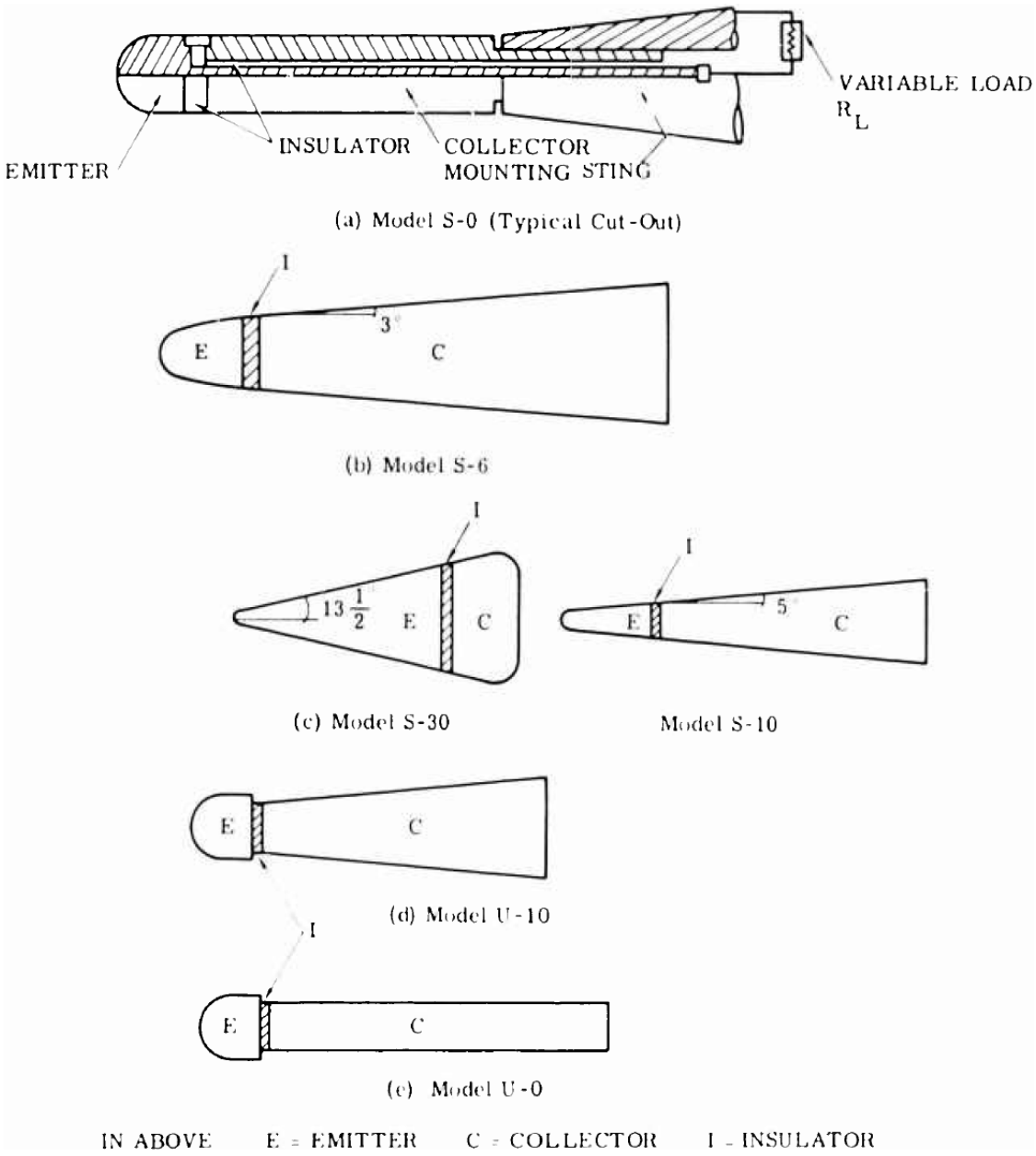

Figure 4.2: Sketches of plasma generator models. Figure from Sandia Corporation.

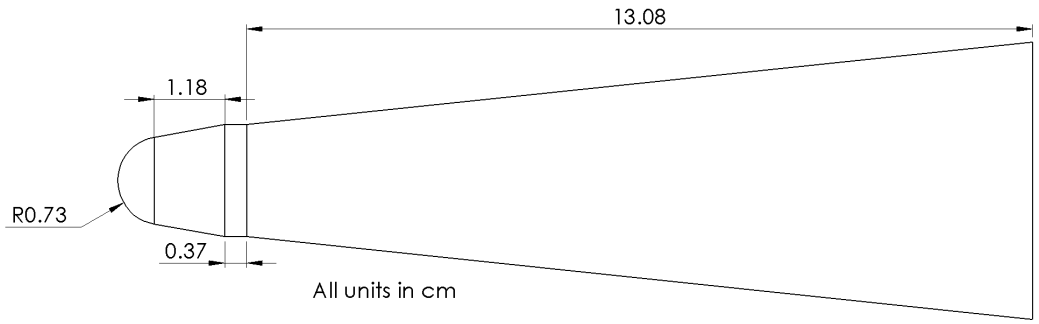

Figure 4.3: S-6 geometry.

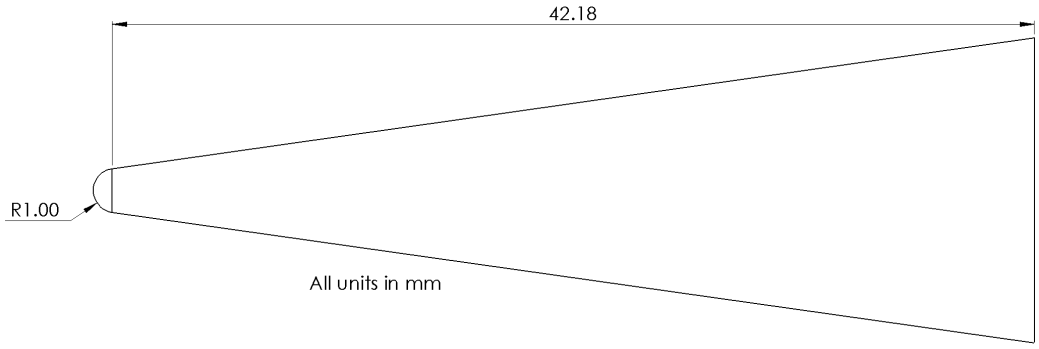

Figure 4.4: S-30 geometry.

4.2.2 Emissive material

The experiments investigated the effect of using different emissive materials on thermionic emission and the resulting power generation. The two materials used for the S-6 and S-30 geometries were graphite and tungsten. The experiments did not cite the material work function or emissivity, so a range of these properties is determined from the literature and are given in Table 4.1. The work functions are significantly higher than those studied in Chapter III (2 - 3 eV). Graphite has a higher emissivity than tungsten, and both vary significantly at the surface temperature range of interest (2000 - 5000 K). Since both the material work function and emissivity have a wide range of possible values, this introduces a large uncertainty in the experiments, especially given how important these two parameters are to the cooling power of the material and resulting emission as will be shown. The material-specific correction factor for the Richardson constant is assumed to equal unity for each material.

Table 4.1: Emissive material properties

Material	W_F [eV]			Refs.	ϵ			Ref.
Graphite	4.65	4.8	5.0	[168, 169, 170]	0.75	0.80	0.85	[171]
Tungsten	4.32	4.48	4.65	[168, 172]	0.30	0.35	0.40	

Table 4.2: Freestream properties of Touryan experiments[69]

Fluid	h_t [MJ/kg]	M	p [Pa]
Air	27.9	2.5 - 3	1010
Argon	11.6		

4.2.3 Freestream Conditions

The experiments also examined the effect of different enthalpies and working fluids on thermionic emission and the resulting power generation. The freestream properties cited in the Touryan experiments are given in Table 4.2. The enthalpies in the experiment's freestream are comparable to the cases investigated in Chapter III; as the enthalpies were 8, 18, and 32 MJ/kg for the 4, 6, and 8 km/s cases at an altitude of 60 km,[1] respectively. However, the computational solver employed requires that the freestream properties are described in terms of temperature, velocity, and density. The following section explains how these properties are determined from Mach number, pressure, and total enthalpy for both air and argon.

4.2.3.1 Air

In order to determine the freestream properties for air, NASA's Chemical Equilibrium with Applications (CEA) computer program is utilized [36]. This approach accounts for both dissociation and ionization of air. However, this approach also assumes the freestream flow is in equilibrium, which is not necessarily the case. The

[1]Specific enthalpy for hypersonic flow is largely independent of altitude and strongly dependent on freestream velocity.

Table 4.3: Converted freestream properties for air

h_t [MJ/kg]	M	T [K]	u [km/s]	ρ [kg/m^3]	$\mu[kg/m/s]$	λ [m]
	2.5	5330	3.99	4.41×10^{-4}	1.60×10^{-4}	1.88×10^{-4}
27.9	2.75	5260	4.31	4.58×10^{-4}	1.58×10^{-4}	1.86×10^{-4}
	3	5180	4.61	4.77×10^{-4}	1.56×10^{-4}	1.84×10^{-4}

Table 4.4: Air mass fractions of the freestream

	Y_s				
M	N_2	O_2	N	O	NO
2.5	4.78×10^{-1}	1.25×10^{-5}	2.86×10^{-1}	2.34×10^{-1}	1.38×10^{-3}
2.75	5.13×10^{-1}	1.50×10^{-5}	2.52×10^{-1}	2.34×10^{-1}	1.53×10^{-3}
3	5.48×10^{-1}	1.84×10^{-5}	2.16×10^{-1}	2.34×10^{-1}	1.70×10^{-3}
	N_2^+	O_2^+	N^+	O^+	NO^+
2.5	1.58×10^{-6}	2.75×10^{-8}	7.51×10^{-6}	9.30×10^{-6}	2.88×10^{-4}
2.75	1.14×10^{-6}	2.49×10^{-8}	4.61×10^{-6}	6.67×10^{-6}	2.60×10^{-4}
3	7.71×10^{-7}	2.21×10^{-8}	2.62×10^{-6}	4.57×10^{-6}	2.30×10^{-4}

converted freestream properties are given in Tables 4.3 and 4.4. The three different Mach numbers are used to cover the range of uncertainty in Mach number, with each value giving different freestream conditions. For the higher Mach numbers, a larger portion of the freestream enthalpy is kinetic energy (i.e. freestream velocity). For the lower Mach numbers, in order for the enthalpy to be the same as the faster moving flows of the high Mach numbers, the freestream temperature is higher, which results in the flow being more ionized at equilibrium as shown in Table 4.4. The mean free path and Knudsen number are calculated using the same approach as in Chapter II. The largest resulting freestream Knudsen number for the air test cases is 0.188. At this Knudsen number, the continuum assumption is less accurate and slip effects can be present but the effects are expected to be small [82].

Table 4.5: Converted freestream properties for argon without ionization

h_t [MJ/kg]	M	T [K]	u [km/s]	ρ [kg/m^3]	$\mu[kg/m/s]$	λ [m]
	2.5	7250	3.96	6.69×10^{-4}	2.13×10^{-4}	3.03×10^{-4}
11.6	2.75	6350	4.08	7.64×10^{-4}	1.94×10^{-4}	2.60×10^{-4}
	3	5590	4.18	8.68×10^{-4}	1.78×10^{-4}	2.23×10^{-4}

4.2.3.2 Argon

A different approach is used to determine the freestream properties for argon. The CEA computer program currently does not have the capability to account for ionization of argon so an approach is developed to convert the freestream properties of argon as follows. First, treating argon as an ideal gas, the enthalpy and Mach number can be converted to a temperature and velocity using the following relations:

$$h_t = C_{p,Ar}T + \frac{M^2\tilde{\gamma}R_uT}{2M_{Ar}}, \tag{4.1}$$

$$u = M\sqrt{\tilde{\gamma}R_uM_{Ar}T}, \tag{4.2}$$

$$p = \rho R_uM_{Ar}T, \tag{4.3}$$

where h_t is the total enthalpy, $C_{p,Ar}$ is the constant pressure specific heat of argon, M is the Mach number, u is the freestream velocity, $\tilde{\gamma}$ is the ratio of specific heats, and p is the freestream pressure. The specific heats for argon are assumed to be constant. The resulting freestream properties without ionization are given in Table 4.5. The largest resulting freestream Knudsen number is 0.303 for the Mach 2.5 S-30 test case. At this Knudsen number, the continuum assumption is less accurate and slip effects can be present but the effects are expected to be small [82].

This approach, however, does not account for ionization in the flowfield. The ionization should be accounted for because the freestream is a high-temperature flow, which is susceptible to ionization, and ionization can greatly impact ETC as shown in Chapter III. The equilibrium level of ionization for argon can be calculated using Saha's equation [79],

$$\frac{\alpha^2}{1-\alpha^2} = \frac{1}{p}\left(\frac{2\pi m_e}{\hbar^2}\right)^{3/2}(k_B T)^{5/2}\frac{2Q_{int}^{Ar^+}}{Q_{int}^{Ar}}\exp\left(\frac{-\theta_i}{T}\right) \tag{4.4}$$

$$Q_{int} \approx g_0 + g_1\exp\left(\frac{-\theta_1}{T}\right) + g_2\exp\left(\frac{-\theta_2}{T}\right) \tag{4.5}$$

where Q_{int} is the internal partition function, which is equal to the electronic partition function in the case of argon, g_j are the degeneracy factors, θ_j are the characteristic temperatures for electronic excitation of energy level j, and θ_i is the characteristic temperature for ionization. Table 4.6 lists the constants used to calculate the electronic partition function and equilibrium level of ionization from Ref. [173].

Equation (4.1) can be modified to account for enthalpy of ionization assuming that the specific heat of argon ions and neutrals are equal [174],

$$h_t = C_{p,Ar}T + \frac{M^2\tilde{\gamma}R_u M_{Ar}T}{2} + \alpha\Delta h_i, \tag{4.6}$$

where Δh_i is the enthalpy of ionization for argon.

Table 4.6: Constants used to calculate equilibrium level of ionization for argon

	Ar	Ar^+
θ_i, K	183,000	
θ_1, K	134,061	2,061
θ_2, K	134,934	156,478
g_0	1	4
g_1	5	2
g_2	3	2

Table 4.7: Converted freestream properties for argon with ionization

h_t [MJ/kg]	M	T [K]	u [km/s]	ρ [kg/m^3]	α
	2.5	7170	3.94	6.80×10^{-4}	3.59×10^{-3}
11.6	2.75	6340	4.08	7.68×10^{-4}	5.78×10^{-4}
	3	5590	4.18	8.71×10^{-4}	7.08×10^{-5}

The resulting freestream properties accounting for ionization are given in Table 4.7. Accounting for ionization results in slightly lower freestream temperatures and velocities, especially for the Mach 2.5 case. It is to be remembered that this approach assumes that the flow is in equilibrium, which is not necessarily the case. Although the level of ionization is low, it is still useful to include charged particles in the freestream for the stability of the numerical method and also more importantly for the effect ionization has on ETC when accounting for plasma sheath effects.

4.3 Modifications to the modeling approach

Given the importance of ionization in the flow to ETC, a finite-rate chemistry model is implemented into the modeling approach to model the electron-impact ionization reactions for argon. The forward reaction rate coefficient is given by [175],

$$k_f(T) = 2.3 \times 10^{34} T^{-3.60} \exp\left(\frac{-182,890}{T}\right) \quad \left[\mathrm{cm}^3/\mathrm{mol/s}\right]. \tag{4.7}$$

The backward reaction rate coefficient is then calculated from the equilibrium constant,

$$K_e(T) = \frac{k_f(T)}{k_b(T)}\,. \tag{4.8}$$

The equilibrium constant for the electron-impact ionization reaction of argon is given in Ref. [176]. When the chemistry only has an electron-impact ionization reaction, such as with argon, the convergence of the CFD calculation is very sensitive to *avalanche ionization* [34, 177]. This avalanche process, or chain reaction, occurs when the ionization equation becomes active at high flow temperatures, such as experienced in this work. The high thermal speed of the electrons results in intrinsically high forward rate coefficients, causing the electron density to increase exponentially. A previous study has shown that the electron number density at the threshold of instigating avalanche ionization is on the order of 10^{-19} m^{-3} [178]. This numerical explosion may lead to numerical divergence of the solution. It was observed that this phenomenon is less likely to occur when there are other possible reactions within the flowfield such as electron impact dissociation (e.g. $N_2 + e \Leftrightarrow N + N + e$) or dissociative recombination (e.g. $N + N \Leftrightarrow N_2^+ + e$). These reactions have much smaller forward rates of reaction compared to electron impact ionization, which corresponds to higher backward (i.e. recombination) rates. For example, here are the forward reaction rates for nitrogen for these types of reactions where T is provided in Kelvin:

Electron impact dissociation

$$k_f(T) = 3.0 \times 10^{24} T^{-1.60} \exp\left(\frac{-113,200}{T}\right) \quad \left[\mathrm{cm}^3/\mathrm{mol/s}\right] \tag{4.9a}$$

Electron impact ionization

$$k_f(T) = 2.5 \times 10^{34} T^{-3.82} \exp\left(\frac{-168,600}{T}\right) \quad \left[\mathrm{cm}^3/\mathrm{mol/s}\right] \tag{4.9b}$$

Dissociative recombination

$$k_f(T) = 4.4 \times 10^{7} T^{-1.50} \exp\left(\frac{-67,500}{T}\right) \quad \left[\mathrm{cm}^3/\mathrm{mol/s}\right] \tag{4.9c}$$

Equations 4.9a to 4.9c are plotted in Figure 4.5 for a wide range of possible flow temperature. As can be seen at high temperatures, the electron impact ionization and electron impact dissociation reactions have much higher forward reaction rates

compared to dissociative recombination. A slower forward rate generally corresponds to a higher backward reaction rate (Eq. 4.8), so dissociative recombination acts as a *sink* to the electrons generated by electron impact reactions reducing the severity of avalanche ionization. However, if argon is the only species in the flow, electron impact ionization is the only reaction present, so the flow will be inevitably prone to avalanche ionization at high temperatures. Implementing this significantly high forward reaction rate into a CFD code can be difficult due to numerical *stiffness*.[2] In a real system, there is also a high recombination rate reducing the severity of avalanche ionization. The challenge for CFD is to resolve the net change without becoming numerically unstable (i.e. crashing). An approach to negate the probability of numerical explosion is to significantly decrease the timestep in the simulations (i.e. the CFL number), which makes the entire calculation slower. Another approach to increasing the numerical stability is to slowly introduce the electron-impact ionization reaction, which in this study is achieved by linearly ramping up the forward reaction rate constant.

4.4 Numerical results

The goal of this study is to compare the ETC modeling approach developed in Chapter II to previous experiments using a range of different freestream conditions, emissive material properties, and geometries.

4.4.1 Flowfield features

The flowfield features for the conditions investigated in this study are shown in Figure 4.6, which presents the flowfield temperature contours for the Mach 2.75 cases for air without and with ETC for both geometries. The intermediate material emissivity and work function are used for each case (e.g. $\epsilon = 0.8$ and $W_F = 4.8$ eV for the

[2]Certain differential equations in the numerical approach become numerically unstable.

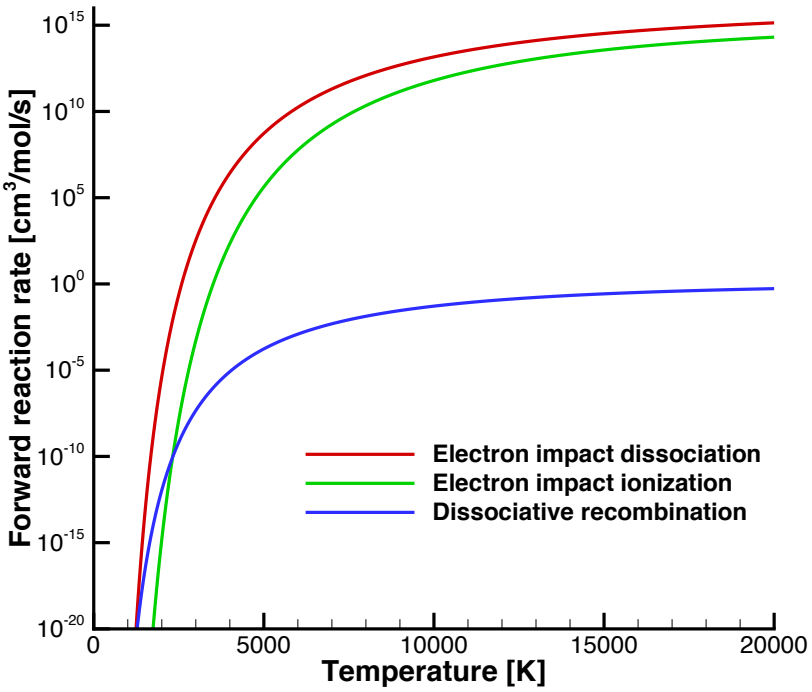

Figure 4.5: Forward reaction rates for nitrogen reactions involving electrons.

S-6 case). For the S-6 case, the fluid temperature rises to above 12,000 K for the S-6 geometry and to nearly 11,000 K for the S-30 geometry across the bow shock, before decreasing in the shock layer. The S-6 bow-shock temperature is higher due to the blunter leading edge of the S-6 geometry compared to the S-30. The small effect ETC has on the flowfield features is similar to that shown in Section 3.3. Similar trends are seen for argon in Figure 4.7. However, the fluid temperature for argon, reaches 21,000 K for the S-6 geometry and nearly 19,000 K for the S-30 geometry across the bow shock, before decreasing in the shock layer. This is expected due to the much higher freestream temperature of the argon cases. The air cases also dissipate energy through dissociation, which lowers the temperature, whereas argon cannot.[3]

Figure 4.8 presents the distribution of translational and vibrational temperatures along the stagnation streamline for the air cases for each Mach number. Although the lower Mach numbers have a slightly higher freestream temperature, the higher Mach numbers still result in higher post shock temperatures. The level of thermal

[3]However, argon can dissipate energy through ionization.

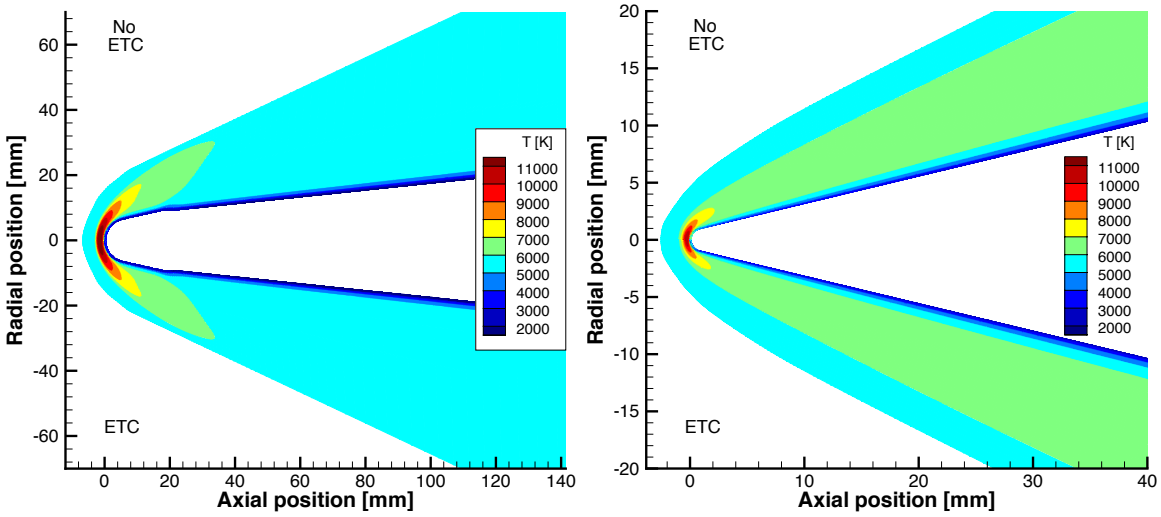

(a) S-6 ($\epsilon = 0.8$, $W_F = 4.8$ eV for ETC). (b) S-30 ($\epsilon = 0.3$, $W_F = 4.48$ eV for ETC).

Figure 4.6: Temperature contours for Mach 2.75 air cases without (top) and with ETC (bottom).

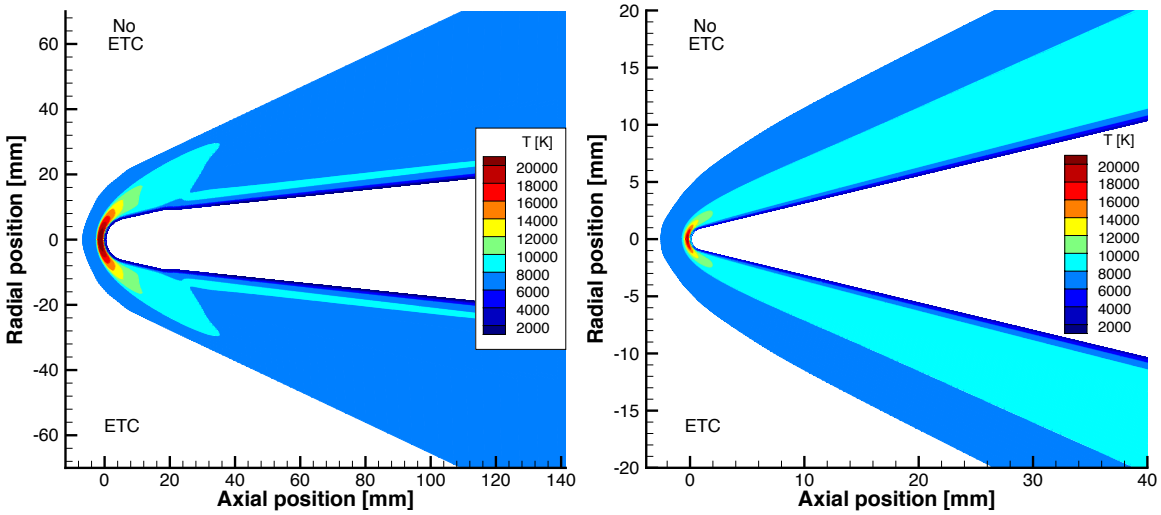

(a) S-6 ($\epsilon = 0.8$, $W_F = 4.8$ eV for ETC). (b) S-30 ($\epsilon = 0.35$, $W_F = 4.48$ eV for ETC).

Figure 4.7: Temperature contours for Mach 2.75 argon cases without (top) and with ETC (bottom).

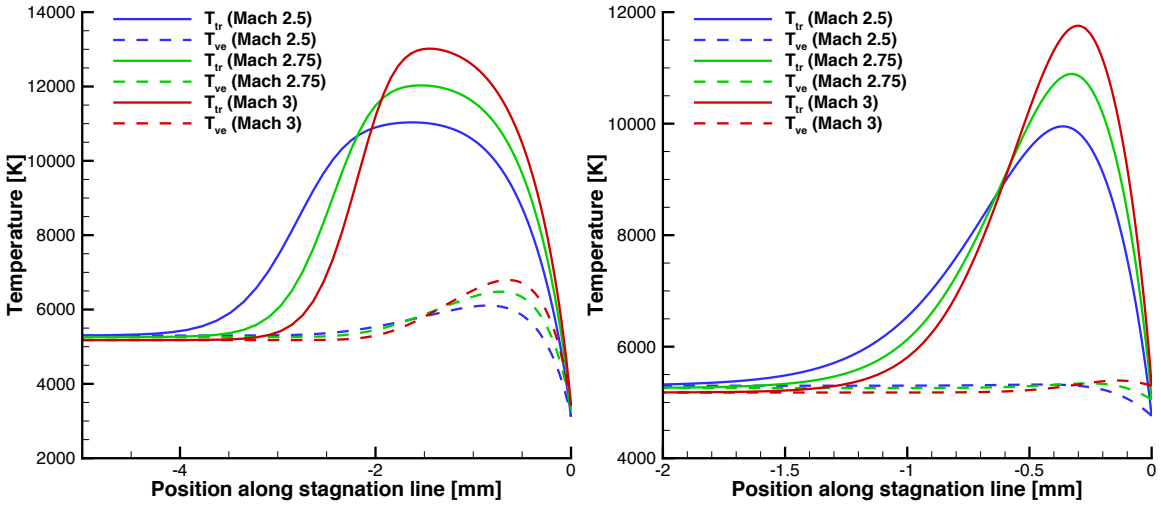

(a) S-6 ($\epsilon = 0.8$). (b) S-30 ($\epsilon = 0.35$).

Figure 4.8: Temperature profiles along stagnation streamline for air for different Mach numbers without ETC.

nonequilbrium is different for each geometry. Since the S-6 has a larger shock standoff distance, it allows for more collisions to occur along the stagnation streamline before reaching the stagnation point, which transfers energy to the vibrational energy mode. However, for the S-30 geometry, the shock standoff distance is much smaller limiting the number of collisions that occur along the stagnation streamline, which leads to the vibrational temperature remaining largely unchanged along the stagnation streamline. The post-shock temperatures are similar to the test cases considered in Chapter III (Fig. 3.9). The distribution of translational temperature along the stagnation streamline for the argon cases is shown in Figure 4.11. Although the lower Mach numbers have a noticeably higher freestream temperature, the higher Mach numbers still result in slightly higher post-shock temperatures. Similar to the air cases, cases with a higher Mach number and sharper leading edge radius result in a smaller shock standoff distance.

Figure 4.10 presents the level of ionization (α) along the stagnation streamline for the air cases. It is to be remembered that the level of ionization is defined as the moles of ions divided by moles of neutral particles. The lower Mach numbers start with a

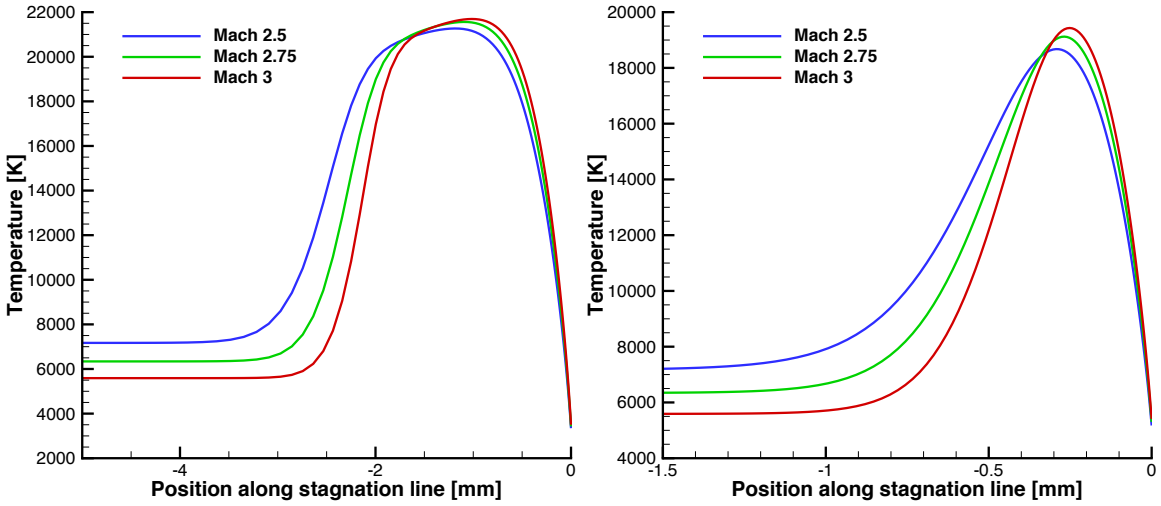

(a) S-6 ($\epsilon = 0.8$). (b) S-30 ($\epsilon = 0.35$).

Figure 4.9: Temperature profiles along stagnation streamline for argon for different Mach numbers without ETC.

slightly higher level of ionization in the freestream but the higher Mach numbers result in higher levels of ionization post-shock and at the stagnation point, largely due to the higher Mach number cases also having larger post-shock temperatures. The level of ionization reaches a maximum after the shock before decreasing in the shock layer. It is to be noted that although the S-6 geometry results in larger post-shock ionization levels, the S-30 geometry results in higher ionization levels at the stagnation point. This is due to the shorter time (shown as distance in Fig. 4.8), the flow has to chemically react (e.g. ions to recombine) for the S-30 case due to its thinner shock layer. Since the level of ionization at the surface is important to ETC as shown in Chapter III, this is a favorable trend for ETC. This trend shows that although a blunter leading edge typically results in a higher post-shock temperature and level of ionization, the level of ionization can actually still be higher at the surface where it is needed to neutralize space-charge effects for a sharp leading edge. This highlights the importance of nonequilibrium modeling for both the flowfield temperature and chemistry. The level of ionization along the stagnation streamline for the argon cases are shown in Figure 4.11. Similar trends are shown as the air

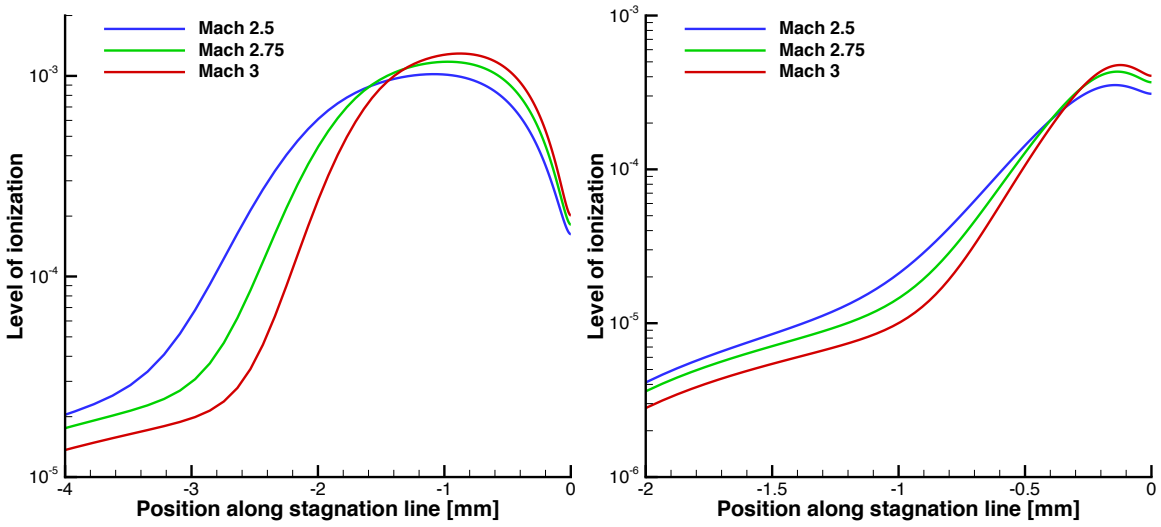

(a) S-6 ($\epsilon = 0.8$). (b) S-30 ($\epsilon = 0.35$).

Figure 4.10: Level of ionization along stagnation streamline for air for different Mach numbers without ETC.

cases but some differences arise that are largely due to the variation is freestream properties (e.g. level of ionization, temperature) as presented in Table 4.7. For the S-6 geometry, the level of ionization is much higher in the freestream for the lower Mach numbers but each case reaches similar peak ionization values post-shock and at the stagnation point. For the S-30 velocity, the Mach 2.5 case has a much higher freestream level of ionization but has a noticeably lower ionization level post-shock. Nonetheless, for all the air and argon cases, the flow can still be considered weakly ionized.

4.4.2 Surface features

As shown in Chapter III, the plasma sheath can greatly affect ETC. The models for representing the plasma sheath discussed in Chapter II are only applicable for a collisionless sheath. For that reason, the collisionality of the sheath for each case is shown in Figure 4.12 for the air cases and Figure 4.13 for the argon cases. Note that the distance along the leading edge is normalized by the leading edge radius. The collisionality is determined using the approach of Section 2.5. The collisional

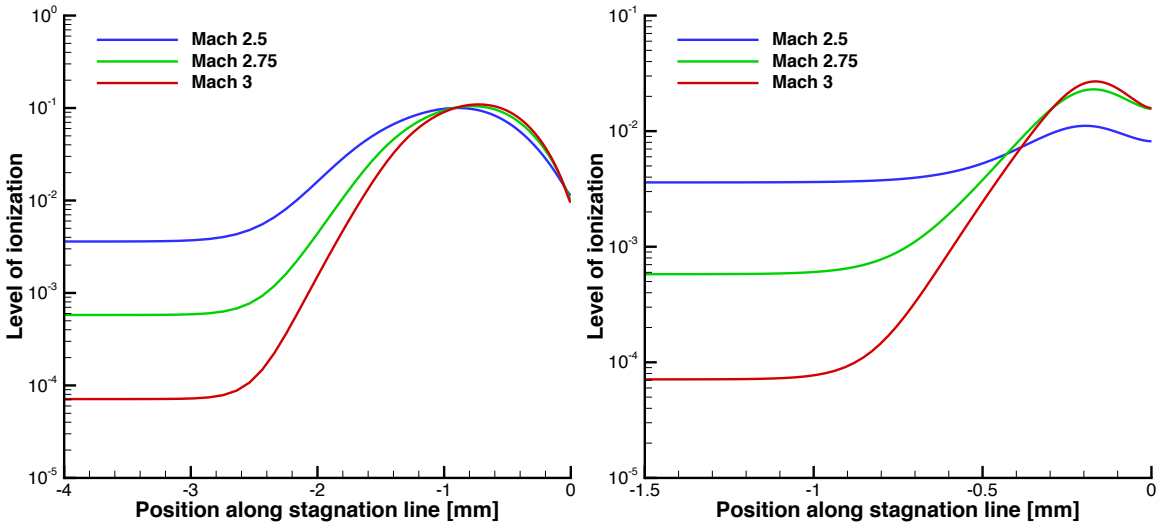

(a) S-6 ($\epsilon = 0.8$). (b) S-30 ($\epsilon = 0.35$).

Figure 4.11: Level of ionization along stagnation streamline for argon for different Mach numbers without ETC.

cross sections for the argon cases are determined using Ref. [179]. Given that the collisionality of each case is less that 0.1, it is appropriate to assume a collisionless sheath for the cases in this study.

The surface temperature profiles along the vehicle with and without ETC for the air cases are shown in Figure 4.14. ETC is modeled both as assuming saturated emission and also accounting for plasma sheath effects. Since the experiments noted that the emissive surface was electrically insulated, the emissive surface is modeled as electrically floating as discussed in Section 2.5.2.1. The case shown in the figure is for the intermediate conditions (i.e. Mach = 2.75, $\epsilon = 0.8$, $W_F = 4.8$ eV), so the specific trends for this case do not necessarily apply to all the other conditions as will be shown in Section 4.4.3. For the S-6 case and without ETC, the stagnation point temperature is at 3280 K, which corresponds closest to the 8 km/s with 1 cm leading edge radius at 60 km altitude from the results of Chapter III. For the case with ETC, the stagnation point temperature is reduced by 6% to 3090 K for both the saturated ETC and ETC with plasma sheath effects modeled cases, which shows that the emission does not reach space charge limits for this case. This surface

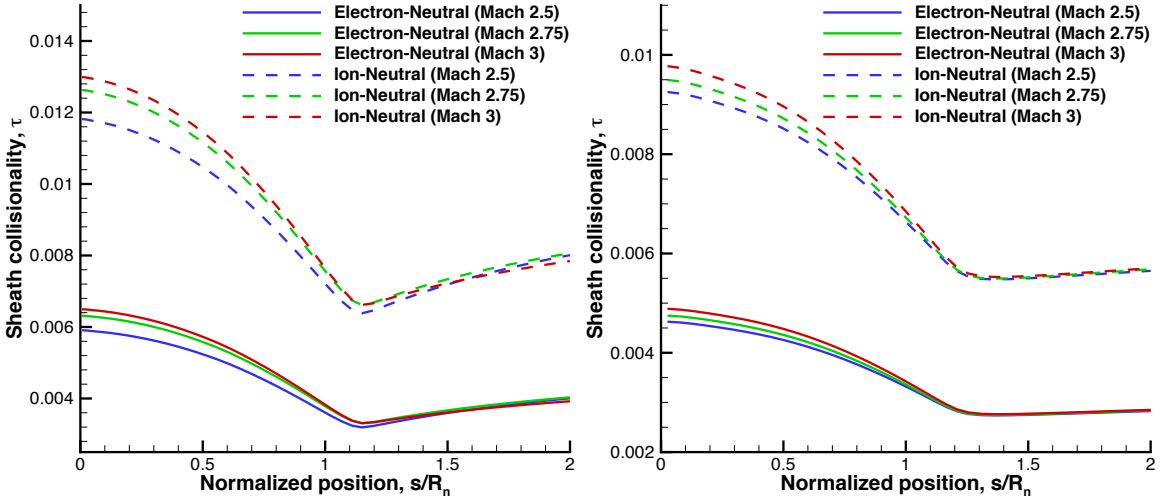

(a) S-6 ($\epsilon = 0.8$). (b) S-30 ($\epsilon = 0.35$).

Figure 4.12: Sheath collisionality profiles along surface for air for different Mach numbers without ETC.

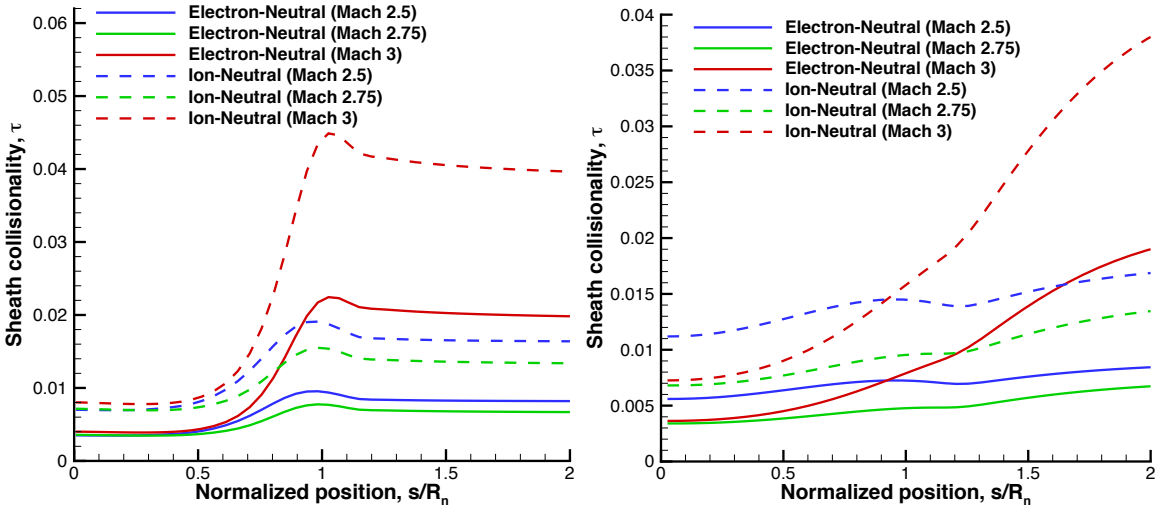

(a) S-6 ($\epsilon = 0.8$, $W_F = 4.8$ eV for ETC). (b) S-30 ($\epsilon = 0.35$, $W_F = 4.48$ eV for ETC).

Figure 4.13: Sheath collisionality profiles along surface for argon for different Mach numbers without ETC.

reduction is much smaller than the reductions shown in Chapter III for comparable cases because the material work function is much higher resulting in less emission. As shown in Figure 2.1, ETC is most effective for low work functions and hot surfaces, and while this case has a hot surface, it has a relatively high work function. It is to be remembered that these experiments were not intended for ETC so it is interesting that the surface temperature profile is noticeably changed, even for an electrically floating surface.[4] This could have far-reaching implications in that ETC could be a meaningful mode of heat transfer present in hot surfaces in ionized atmospheres, even if not specifically designed for ETC (e.g. low work function materials, biased surfaces). For the S-30 case shown in Figure 4.14(b) and without ETC modeling, the stagnation point temperature is 5070 K, which is significantly hotter than the S-6 case. This is due to leading edge radius being sharper and the material emissivity for the S-30 case ($\epsilon = 0.35$) being much smaller than the S-6 case ($\epsilon = 0.8$). This lower emissivity results in radiative cooling being less effective (Eq. 2.2). When ETC is accounted for and assuming saturated emission, the surface temperature is significantly reduced, most notably a 34% reduction of the stagnation point temperature. However, if ETC is modeled with sheath effects, this surface reduction is not realized due to space-charge limits and the stagnation point temperature is only reduced by 5%, which is still a noticeable reduction nonetheless. Figure 4.14(b) shows that even with a work function over 4 eV, saturated ETC can provide significant *ideal* cooling effects but these are not realized due to space-charge limits emphasizing the importance of modeling the plasma sheath.

The surface temperature profiles along the vehicle with and without ETC for the argon cases are shown in Figure 4.15. For the S-6 case, the trends are similar to those of air. The stagnation point temperature is 3430 K without ETC accounted for and is reduced by 7% with ETC for both saturated ETC and ETC with plasma sheath

[4]Surface temperature was not reported in the experiments.

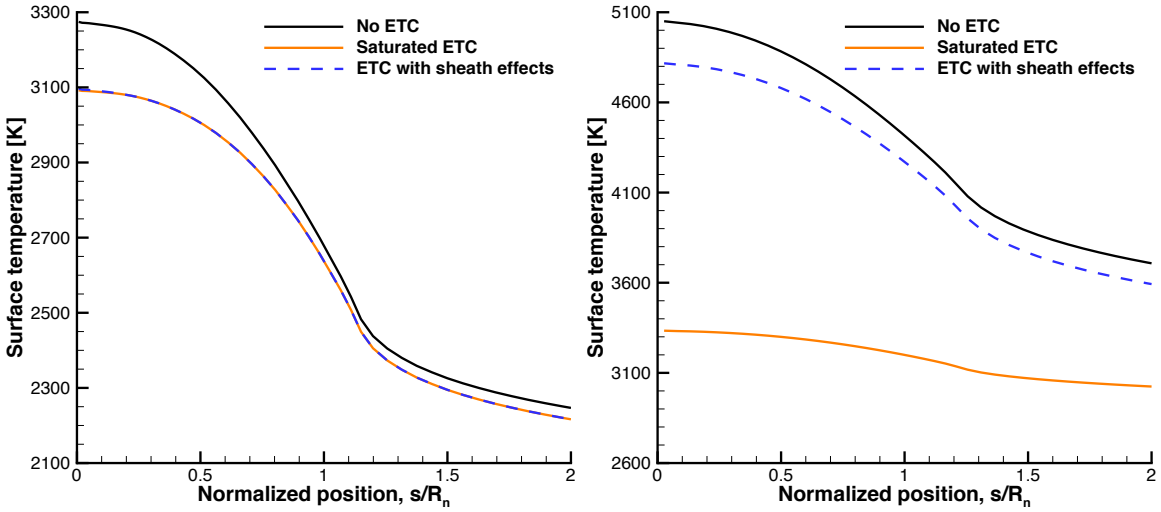

(a) S-6 ($\epsilon = 0.8$, $W_F = 4.8$ eV for ETC). (b) S-30 ($\epsilon = 0.35$, $W_F = 4.48$ eV for ETC).

Figure 4.14: Surface temperature profiles for the Mach 2.75 air cases without and with ETC.

effects. Similar to the corresponding air case, the emission does not reach space-charge limits near the leading edge. For the S-30 case, without ETC accounted for the stagnation point temperature is 5300 K and if ETC is accounted for, it is reduced by 36% to 3380 K for both saturated ETC and ETC with plasma sheath effects. Although space-charge limits are not reached near the stagnation point, farther along the leading edge the space-charge limits are reached and the temperature predicted by saturated ETC and ETC with plasma effects diverge. For this case, the stagnation point temperature is not the maximum surface temperature as has been shown in previous results.

The resulting emission current density profiles for the Mach 2.75 air and argon cases are shown in Figure 4.16. For both the S-6 air and argon cases, the levels of emission predicted by saturated ETC and ETC with plasma sheath effects are identical, reiterating that the emission does not reach space-charge limits for these cases. However, for the S-30 cases, space-charge limits are reached. For the S-30 air case, the emission is space-charge limited for this entire region of leading edge. However, for the S-30 argon case, the emission is not limited at the stagnation point

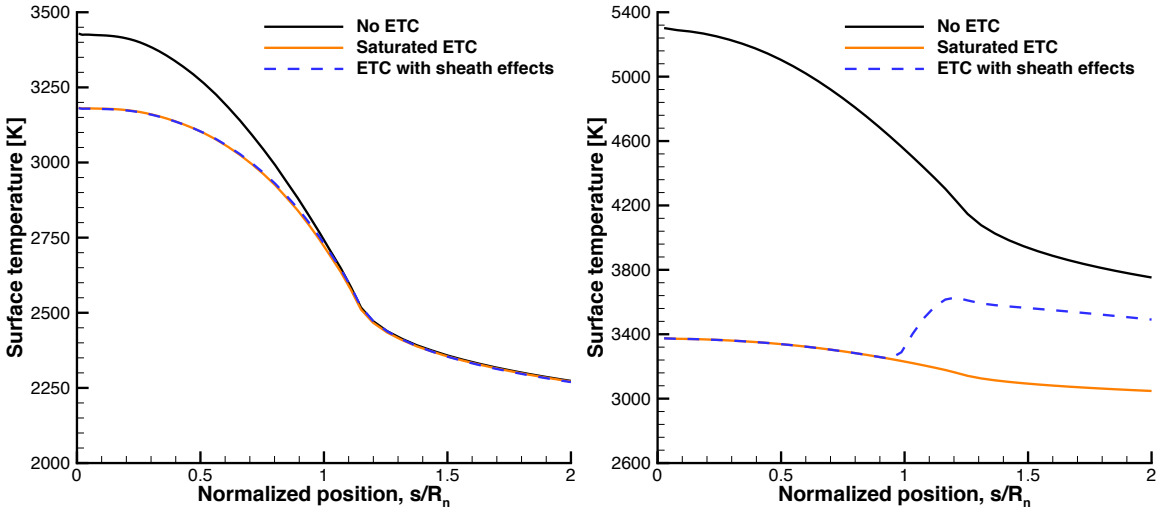

(a) S-6 ($\epsilon = 0.8$, $W_F = 4.8$ eV for ETC). (b) S-30 ($\epsilon = 0.35$, $W_F = 4.48$ eV for ETC).

Figure 4.15: Surface temperature profiles for the Mach 2.75 argon cases without and with ETC.

but eventually is space-charge limited further down the leading edge even though the emission is lower there. This suggests there is enough ionization in the flow near the stagnation point that is significant enough to overcome space-charge limits but not large enough further along the surface to overcome space-charge limits at that location. Since the space-charge limits are largely dependent on the ion number density at the sheath edge (or surface since the sheath is collisionless), as discussed in Section 2.5, the ion number density profiles are presented in Figure 4.17. For air, the higher Mach numbers result in higher ion number densities along the surface and the blunter shape (S-6) results in higher levels of ionization as well. This is similar to the trend shown in Figure 4.10, which presented the level of ionization along the stagnation line for air. The trends for the argon cases shown in Figure 4.17(b) are less discernible. For the S-6 geometry near the stagnation point, the number density of ions are similar that is also shown in Figure 4.10, which presented the level of ionization along the stagnation point. However, further along the leading edge the number density for each Mach number diverges, with lower Mach number resulting in higher ion densities at the surface. This is due to the shock being weaker further

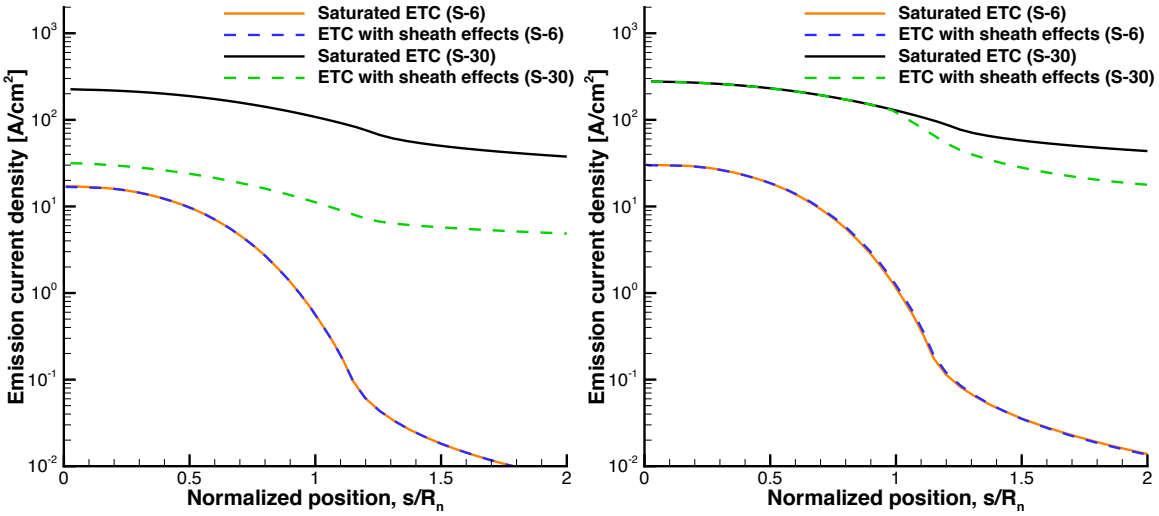

(a) Air. (b) Argon.

Figure 4.16: Emission current density profiles for the Mach 2.75 cases with saturated ETC and ETC with plasma sheath effects.

away from the stagnation point so the freestream number density of ions become more imperative.[5] A similar trend is seen for the S-30 geometry for argon. Higher Mach numbers result in higher ion number densities at the stagnation point but result in lower number densities farther along the surface. To reiterate, a higher Mach number results in a stronger shock, which makes up for the lower number density of ions in the flowfield near the stagnation point but not further along the surface. These ionization trends for the argon cases can result in the surface temperature profile being unconventional (i.e. peak temperature not at stagnation point) as seen in Figure 4.15(b). This shows the importance of accurately determining the freestream ionization and accurately modeling the chemistry in the flow, especially ionization because the plasma sheath models greatly rely on the ion number density and it can have an impact on the surface temperature profile. It is to be noted that the ion number densities for the argon case are mostly beyond the reported threshold of avalanche ionization ($\sim 10^{-19}$ m^{-3}), especially near the stagnation point.

[5]Lower Mach numbers had significantly more ions in the freestream as presented in Table 4.7.

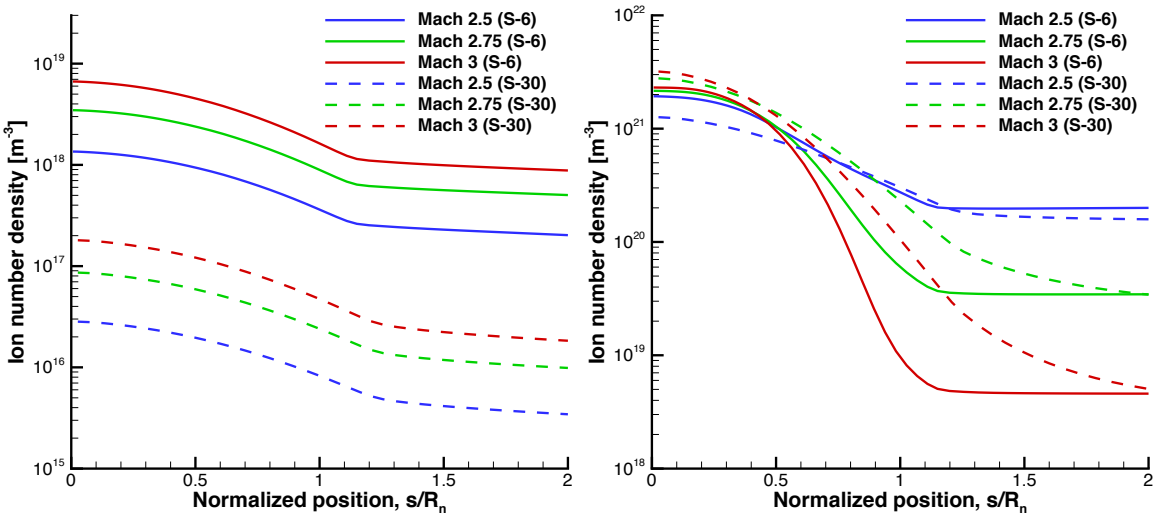

(a) Air.

(b) Argon.

Figure 4.17: Ion number density profiles for varying Mach numbers and geometry.

4.4.3 Comparison to experimental data

The experiments measured the short-circuit currents from the emitter region, which are compared to the computational results in this section. It is to be remembered that the emitter region for the S-6 geometry consists of the axisymmetric cone followed by a cylinder as shown in Figure 4.3, which corresponds to 8.4 cm^2 of emitter surface area. For the S-30 geometry, the emitter refers to the entire region shown in Figure 4.4, which corresponds to 16 cm^2 of emitter surface area. This is noted because although the S-30 geometry is a sharper cone, the emitter region is significantly larger, which is important because the current is reported as a single current per area value. For each geometry and fluid, the experiments cite a single value for the current from the emitter region. However, the experiments cited under the best conditions of control, the repeatability of the experiments varied between 10 and 25%.

The results for the air cases are presented in Tables 4.8 and 4.9. For the S-6 geometry, which used graphite as the emitter material, the results are presented in Table 4.8. The results include three possible values of Mach number, material emis-

Table 4.8: Experimental vs. computational emitter current (A/cm^2) for S-6 air cases

	ϵ								
	0.75			0.80			0.85		
	W_F [eV]								
M	4.65	4.8	5.0	4.65	4.8	5.0	4.65	4.8	5.0
	Saturated ETC								
2.5	1.05	0.702	0.389	0.863	0.561	0.300	0.707	0.449	0.232
2.75	2.03	1.45	0.885	1.72	1.21	0.713	1.46	1.00	0.574
3.0	3.13	2.34	1.52	2.72	1.99	1.26	2.37	1.70	1.05
	ETC including space-charge limits[a]								
2.5	*1.02*	0.702	0.389	0.863	0.561	0.300	0.707	0.449	0.232
2.75	*1.72*	*1.40*	0.885	*1.56*	1.21	0.713	*1.40*	1.00	0.574
3.0	*2.38*	*2.08*	1.52	*2.22*	*1.88*	1.26	*2.05*	*1.67*	1.05
Experimental	**0.62**								

[a] Value in italic denotes space-charge limits are reached.

sivity, and material work function creating a large range of possible emitter current from the surface. If the emission is modeled assuming saturated current as was done in Ref. [72], the emission ranges from 0.232 A/cm^2, for the Mach 2.5 case with a material work function of 5.0 eV and material emissivity of 0.85, to 3.13 A/cm^2 for the Mach 3 case with a material work function of 4.65 eV and material emissivity of 0.75. Higher currents are observed for higher Mach numbers, lower material emissivities, and lower work functions. The lower material emissivity means that radiative cooling is less effective, which allows ETC to contribute more to the cooling power. The computational values agree reasonably well with the experimental value of 0.62 A/cm^2. If the emission is modeled accounting for plasma sheath effects, 11 of the 27 cases are affected by space-charge limits. The cases more prone to space-charge limits are generally the cases that resulted in higher levels of emission from the surface as expected. With plasma sheath effects accounted for, the maximum emitter current is lowered by 42% to 2.38 A/cm^2 narrowing the range of possible emitter current.

For the S-30 geometry, which used tungsten as the emitter material, the results for emitter current are presented in Table 4.9. If the emission is modeled assuming

Table 4.9: Experimental vs. computational emitter current (A/cm^2) for S-30 air cases

	ϵ								
	0.30			0.35			0.40		
	W_F [eV]								
M	4.32	4.48	4.65	4.32	4.48	4.65	4.32	4.48	4.65
	Saturated ETC								
2.5	4.69	3.52	2.54	3.52	2.55	1.79	2.65	1.88	1.29
2.75	7.08	5.51	4.12	5.53	4.15	2.99	4.31	3.13	2.21
3.0	9.60	7.52	5.79	7.56	5.84	4.33	6.05	4.52	3.26
	ETC including space-charge limits[a]								
2.5	*1.66*	*1.59*	*1.30*	*1.52*	*1.26*	*0.941*	*1.26*	*0.944*	*0.675*
2.75	*2.02*	*2.02*	*1.93*	*1.94*	*1.86*	*1.54*	*1.83*	*1.54*	*1.18*
3.0	*2.29*	*2.28*	*2.28*	*2.20*	*2.19*	*2.04*	*2.12*	*2.02*	*1.64*
Experimental	**0.70**								

[a] Value in italic denotes space-charge limits are reached.

saturation current, the emission ranges from 1.29 A/cm^2, for the Mach 2.5 case with a material work function of 4.65 eV and material emissivity of 0.40, to 9.60 A/cm^2 for the Mach 3 case with a material work function of 4.32 eV and material emissivity of 0.3, creating a wide range of possible emitter currents. These computational values are higher than the measured emitter current value of 0.70 A/cm^2. However, if the emission is modeled accounting for plasma sheath effects, all of the cases are affected by space-charge limits reducing the emitter current. These cases are expected to be more prone to space-charge limits than the previous S-6 cases because the saturated current is higher and also the ion number density at the surface is significantly lower compared to the S-6 cases (Fig.4.17). The space-charge limited current density ranges from 0.675 to 2.29 A/cm^2, which agrees better with the experimental result of 0.70 A/cm^2, although still generally higher.

The measured currents from the emitter region are compared to the argon computational results in Tables 4.10 and 4.11. For the S-6 geometry, which used graphite as the emitter material, the results are presented in Table 4.10. If the emission is

Table 4.10: Experimental vs. computational emitter current (A/cm^2) for S-6 argon cases

	ϵ								
	0.75			0.80			0.85		
	W_F [eV]								
M	4.65	4.8	5.0	4.65	4.8	5.0	4.65	4.8	5.0
	Saturated ETC								
2.5	2.79	2.07	1.34	2.41	1.75	1.10	2.08	1.48	0.900
2.75	3.59	2.68	1.83	3.14	2.31	1.53	2.74	1.98	1.28
3.0	4.36	3.39	2.34	3.86	2.95	1.99	3.41	2.56	1.68
	ETC including space-charge limits[a]								
2.5	2.79	2.07	1.34	2.41	1.75	1.10	2.08	1.48	0.900
2.75	3.59	2.68	1.83	3.14	2.31	1.53	2.74	1.98	1.28
3.0	4.36	3.39	2.34	3.86	2.95	1.99	3.41	2.56	1.68
Experimental	**3.3**								

[a] Value in italic denotes space-charge limits are reached.

modeled assuming saturated current, the emission ranges from 0.900 A/cm^2, for the Mach 2.5 case with a material work function of 5.0 eV and material emissivity of 0.85, to 4.65 A/cm^2 for the Mach 3 case with a material work function of 4.65 eV and material emissivity of 0.75. These computational results agree well with the experimental value of 3.3 A/cm^2. If the emission is modeled accounting for plasma sheath effects, none of the cases are affected by space-charge limits.

For the S-30 geometry, which used tungsten as the emitter material, the results are presented in Table 4.11 for argon. If the emission is modeled assuming saturation current, the emission ranges from 2.62 A/cm^2, for the Mach 2.5 case with a material work function of 4.65 eV and material emissivity of 0.40, to 9.93 A/cm^2 for the Mach 3 case with a material work function of 4.32 eV and material emissivity of 0.3. These computational values are generally higher than the measured emitter current value of 3.3 A/cm^2. However, if the emission is modeled accounting for plasma sheath effects, all the cases are affected by space-charge limits, reducing the emitter current. The space-charge limited current density ranges from 1.8 to 7.98 A/cm^2,

Table 4.11: Experimental vs. computational emitter current (A/cm^2) for S-30 argon cases

	ϵ								
	0.30			0.35			0.40		
	W_F [eV]								
M	4.32	4.48	4.65	4.32	4.48	4.65	4.32	4.48	4.65
	Saturated ETC								
2.5	8.07	6.37	4.84	6.37	4.84	3.54	5.01	3.69	2.62
2.75	9.09	7.25	5.57	7.27	5.59	4.13	5.78	4.30	3.08
3.0	9.93	7.99	6.19	8.02	6.22	4.63	6.45	4.84	3.49
	ETC including space-charge limits[a]								
2.5	*6.09*	*4.98*	*3.87*	*4.91*	*3.83*	*2.85*	*3.90*	*2.93*	*2.11*
2.75	*7.98*	*6.49*	*5.07*	*6.45*	*5.04*	*3.79*	*5.16*	*3.91*	*2.85*
3.0	*2.41*	*2.40*	*2.37*	*2.37*	*2.35*	*2.15*	*2.33*	*2.17*	*1.80*
Experimental	**3.3**								

[a] Value in italic denotes space-charge limits are reached.

which agrees better with the experimental result of 3.3 A/cm^2. It is to be noted that the largest Mach number no longer results in the highest level of emitter current as was the trend in previous cases. The intermediate Mach number of 2.75 results in the highest levels of space-charge limited emission closely followed by the Mach 2.5 cases. The Mach 3 cases actually result in the lowest levels of emission, which is the opposite of the previous trend. This is due to the number density of ions at the surface as shown in Figure 4.17(b). Although higher Mach numbers result in slightly higher ion number density at the stagnation point, the number density farther along the surface is significantly smaller than the lower Mach numbers. This leads to higher Mach numbers having slightly higher space-charge limited emission near the stagnation point, but markedly lower space-charge limited emission on the aft-body of the emissive surface due to the low level of ionization on the aft-body, which also contributes to the reported emitter current.

The computational results for each geometry and fluid agree reasonably well with the experimental data, especially given the number of uncertainties in the exper-

iments and agree even more favorably when accounting for plasma sheath effects. Generally, the computational results with plasma sheath effects accounted for bound the experimental data point quite well. It is to be noted that the air cases are generally higher than the experimental data point and agree less favorably compared to the argon cases. A potential explanation for why the computational cases for air are high is that the emissive surface could become oxidized under the experimental conditions, which would lead to an increase in the emissivity of surface [180]. This increase in surface emissivity would lower the emitted current. The modeling approach also assumes the work function of the material is constant, whereas it may change as the material degrades under high-temperature exposure. Given the uncertainties in the freestream conditions (i.e. Mach number) and emissive surface properties (i.e. material work function and emissivity) of the experiments, the level of agreement obtained is considered satisfactory. The comparisons also provide motivation for new experiments to be performed and for further refinement of the computational models to better understand the potential benefits of ETC.

4.5 Conclusions

The goal of this chapter was to assess the ETC modeling approach using a set of experiments that occurred over 50 years before ETC was first proposed. First, the experiments were briefly described. This was followed by generating applicable test cases in order to use the experiments to assess the modeling approach, which included determining experimental geometries, materials, and freestream conditions. Modifications to the numerical approach were made in order to investigate argon as a working fluid. The numerical results were then presented that detailed the flowfield and surface features of the test cases. This showed that ETC can noticeably impact the surface temperature even for cases not specifically designed for ETC, which suggests ETC should possibly be included in other modeling approaches of

hot surfaces in an ionized atmosphere. The chapter concluded by comparing the experimentally measured emitter current for different emitter surfaces (e.g. geometry and material) and flows (e.g. air and argon). The computational results produced a wide range of emitted current due to the uncertainty in the freestream conditions and emissive material, but they still agreed well with the experiments.

CHAPTER V

Conclusion

In this final chapter, the results and conclusions that have been presented throughout this thesis are summarized and the implications of the work are discussed. The original contributions to the field as represented by this dissertation are listed and discussed. Finally, this chapter concludes with several recommendations for future research directions.

5.1 Summary

Chapter I introduced and motivated the work of this dissertation. This chapter highlighted that the development of aeronautics has been largely driven by the passion to fly faster and how recent advancements in technologies have enabled the possibility of hypersonic vehicles. However, if the increases in flight speeds are to continue, which is predicted with the growth of national and global interest in hypersonic flight, there are multiple areas where the technology needs to be advanced to forward the frontier of flight. This chapter details one of these areas currently limiting hypersonic flight, which presents itself as a contradicting aerothermodynamic design requirement. A hypersonic cruise vehicle requires sharp leading edges to decrease the drag in order to maximize the range. However, the aerodynamic performance gains obtained by having a sharp leading edge come at the cost of very high, localized heating rates.

This chapter discussed how there is currently no ideal way to manage these heating loads for sustained hypersonic flight, especially as the velocity approaches orbital. An approach to managing these heating loads has been recently proposed that involves using thermionic materials at the leading edges of hypersonic vehicles. When exposed to high convective heating rates, these materials emit a current of electrons that leads to a cooling effect of the surface of the vehicle called electron transpiration cooling (ETC). The electrons are emitted through a phenomenon known as thermionic emission that occurs when the thermal energy given to the electrons is greater than the binding potential of the surface material. This led to the purpose of this work, which is to use numerical modeling to investigate the effect ETC has on leading edges of slender hypersonic vehicles, which are prone to high heating rates. This chapter also provided the background on hypersonics, motivating the importance of nonequilibrium modeling and accounting for *real* gas effects. Finally, this chapter provided background on the underlying phenomenon, thermionic emission, which has been studied extensively since the 19th century.

Chapter II described the modeling approach utilized and developed to investigate ETC on leading edges of hypersonic vehicles. This discussion included the heat transfer theory; most notably the heat transfer provided by the emitted electrons. The cooling power of ETC with saturated emission is compared to radiative cooling in this chapter, and the cooling power of ETC showed promising trends to be a viable mode of surface cooling. The conditions of interest were also discussed in this chapter, using the flight of the X-43A as the baseline case. The flowfield modeling was discussed in detail in this chapter. This included motivation for using CFD for the numerical simulations and showed that at higher altitudes, the validity of CFD degrades. The conservation equations were detailed as well as the updated boundary conditions to account for electron emission. The electric field modeling was detailed including forced diffusion and the Schottky effect and justification was provided for

neglecting the magnetic field. Plasma sheath physics were also explored in this chapter in order to better estimate the level of emission and how space-charge limits can affect ETC. The material response solver was also described in this chapter, which models the in-depth surface conduction. Overall, this chapter demonstrated that the modeling approach discussed can be used to investigate ETC for conditions of sharp leading edges during hypersonic flight.

Chapter III presented the numerical results of a detailed investigation of ETC. First, test cases applicable to a leading edge of a hypersonic vehicle were presented, which included different geometries, freestream conditions, and material properties that were to be investigated in this chapter. The flowfield and surface features without ETC were then presented, which highlighted the thermally intense environment where ETC is possibly to be applied. Then ETC was investigated assuming saturation levels of emission, which showed ETC can be very effective at cooling the surface, especially for a surface prone to high temperatures (high velocity, sharp leading edge, low altitude). This investigation, however, neglected plasma sheath effects, which were then investigated for two different types of emissive surfaces. If the emissive surface is electrically floating, ETC can be greatly reduced by space-charge limits, at least for the test cases considered. Biasing the surface can alleviate the restriction of space-charge limits to some extent, depending on the number of charged species in the flowfield. This resulted in ETC being more effective at higher velocities due to higher ionization of the flowfield but the lower velocities remained prone to space-charge limits. A highlight of this study was that ETC could decrease the stagnation point temperature by nearly 50% for a leading edge radius of 1 cm flying at orbital velocity at an altitude of 60 km. The effect of the electric field was studied in this chapter and although ETC induces a small electric field, it has negligible effects on the surface temperature. This chapter also included an investigation of the effect of in-depth surface conduction on ETC, which showed ETC is still effective at cooling

the surface even if heat is allowed to travel into the surface. Finally, this chapter concluded with an assessment of the plasma sheath models utilized in the CFD code, which validated their use.

Chapter IV focused on assessing the ETC modeling approach using a set of experiments that occurred over 50 years before ETC was first proposed. First, the experiments were briefly described. This was followed by generating applicable test cases in order to use the experiments to assess the modeling approach, which included determining experimental geometries, materials, and freestream conditions. Modifications to the modeling approach were made in order to investigate argon as a working fluid. The numerical results were then presented which detailed the flowfield and surface features of the test cases. This showed that ETC can noticeably impact the surface temperature even for cases not specifically designed for ETC, which suggests ETC should possibly be included in other modeling approaches of hot surfaces in an ionized atmosphere. The chapter concluded by comparing the simulated results with the experimentally measured emitter current for different emitter surfaces (e.g. geometry and material) and flows (e.g. air and argon). The computational results produced a wide range of emitted current due to the uncertainty in the freestream conditions and emissive material, but they still agreed well with the measurements.

5.2 Contributions

The contributions of the research efforts detailed in this dissertation range from assessing a recently proposed technology to extending plasma sheath theory to using past experiments to assess recent modeling approaches. Many of the contributions are provided in the following peer-reviewed journal articles [72, 140] and conference papers [110, 181, 182, 183, 184]. The key contributions include:

- **Matured a modeling approach for ETC.** Since ETC is a recently proposed

approach for managing the intense heat loads at the leading edges of hypersonic vehicles, the modeling approach presented in this thesis is the first to model this behavior in a hypersonic flow. This activity included finding applicable theory from the plasma physics community to apply to the boundary conditions of the CFD code as well as determining where the modeling approach is applicable. Additionally, approaches were developed in order to more accurately model the emission such as approximating the electron temperature at the sheath edge without solving for it explicitly.

- **Extended and assessed plasma sheath theory.** A significant portion of the plasma sheath theory utilized in this thesis has not been assessed before. This theory was assessed using a grid-based direct kinetic simulation in order to determine its validity. In order to accurately assess the theory with the simulations, the warm space-charge limited emission theory was extended to account for supersonic ion velocities, whereas previously the theory assumed the ion velocity to be sonic.

- **Implemented ETC into a coupled flow-material response code.** In order to better represent the heat load at the leading edge of the hypersonic vehicle, the ETC model was also implemented in a framework that allowed for heat to conduct into the material. The results of this investigation provided insight into how in-depth surface conduction affects ETC and also allows for the exact ETC material properties, once characterized, to be included in future investigations. This implementation also allows ETC to be investigated for certain flight envelopes instead of only one trajectory point at a time.

- **Evaluated modeling approach using experimental data.** Experiments were found that occurred over 50 years before ETC was first proposed and were used to assess the modeling approach for ETC. This contribution included

interpreting dated reports in order to generate applicable test cases for the simulations. The simulations agreed reasonably well with the experimental data given the range of uncertainty. This is the first time these experiments were simulated.

- **Implemented argon with ionization into CFD approach.** Implementing argon as the only working fluid and accounting for ionization in a hypersonic solver is a unique contribution, at least for the CFD solver, LeMANS. This included implementing the finite-rate chemistry for the electron impact ionization reaction and also developing an approach to negate the probability of numerical divergence due to avalanche ionization. This contribution was needed in order to assess the modeling approach using past experimental data.

- **Investigated ETC as a viable technology.** This work investigated ETC as a viable technology for a wide range of conditions. This included different altitudes, geometries, freestream velocities, and material properties. This investigation provided insight as to when ETC is most effective, which provides guidance for ETC material development as well as designing future experiments. This work also showed that heat transfer provided by ETC can be present in hot surfaces exposed to ionized atmospheres affecting surface properties, even for cases not designed for ETC (i.e. high work function materials, electrically floating surfaces).

5.3 Future Work

This thesis provided significant insight into better understanding how ETC will perform on leading edges of hypersonic vehicles. However, continued research is needed in multiple areas in order to both understand ETC better and to develop it into a usable technology. These recommended areas of future work are described

in more detail in this section.

5.3.1 Continue to improve the modeling approach

ETC is a complex phenomenon given it involves plasma physics in an already intricate field to model, nonequilibrium hypersonic flow. So like most modeling approaches, improvements in fidelity will always be possible and sought after. These improvements include expanding the modeling approach in order to investigate ETC in different flow regimes that are possible during hypersonic flight as discussed in Section 2.2. This would include accounting for slip-effects in the high Knudsen number transitional regime or using a hybrid particle-continuum method as discussed in Ref. [40]. Improvements are also desired to investigate ETC in the continuum regime more accurately. This work used an approximate approach to model the electric field but given the importance the electric field can have on electrons, the accuracy of this approach needs to be assessed. This could be performed by coupling the Navier-Stokes equations to Maxwell's equations similar to the work in Ref. [109].

The plasma sheath models used in this work can be improved as well. This would include assessing how collisions within the sheath affect ETC as well as accounting for multidimensional processes since this work assumed a collisionless, one-dimensional sheath. Also, it is desired to use an approach to determine the sheath potential based on operating conditions instead of setting it to a discrete value as was done in this work. One of the strongest assumptions of this work assumed that emitted electrons, which are accelerated through the sheath, transfer energy to the flowfield at a significant distance away from the emitting surface. This assumption resulted in the heat transfer balance not being affected at the leading edge due to this energy increase of emitted electrons, other than estimating for the electron temperature used in the sheath models. Characterizing how this increase in emitted electron energy truly affects the heat transfer at the surface is an important area of future

work. This includes solving for the electron temperature in the flowfield explicitly similar to the approach in Ref. [144], and accounting for the electron energy in the boundary condition similar to the approach in Ref. [142]. Finally, this work focused on the effect of ETC near the leading edge. However, the proposed method of ETC involves also collecting the electrons on the aft-body of the hypersonic vehicle. This motivates future work to improve the modeling approach to track the electrons in the flowfield and allow them to recombine on the aft-body as shown in Figure 2.10. These improvements in the modeling approach will lead to a better understanding of ETC.

5.3.2 Continue to investigate ETC with different parameters

This thesis investigated many possible operational conditions that are applicable to ETC and it was shown that ETC can have distinctly different effects depending on material properties (e.g. work function, emissivity), freestream properties (e.g. altitude and velocity), leading edge shape, and emissive surface type (e.g. electronically floating surfaces). For example, as shown in Figure 1.3, the flight trajectory of hypersonic cruise vehicles will encompass a large range of velocities and altitudes. This motivates future work to include a detailed parametric study to better understand what conditions ETC is most effective at. Additionally, this work only investigated leading edges at zero angle-of-attack so future work should include investigating the effect of angle-of-attack as well.

5.3.3 Determine if ETC was present in past thermally intensive flights and experiments

It was shown in Section 4.4 that accounting for ETC can result in different surface properties (i.e. temperature) than if ETC is not accounted for, even for surfaces with relatively high work functions and that are electrically floating. This shows that ETC

can noticeably impact the surface temperature even for cases not specifically designed for ETC, and suggests that ETC should possibly be included in other modeling approaches of hot surfaces in an ionized atmosphere. For this reason, future work will include determining if ETC was present in past thermally intensive flights and experiments. This is important because if ETC is an active mode of heat transfer for these cases and it was not accounted for, it could possibly lead to errors in the simulation results of these flights and experiments, which lead to uncertainties in the modeling approach. Past flights could include atmospheric reentry missions such as Stardust and Apollo, while past experiments could include experiments performed in plasmatrons and arc-jets; all of which include thermally intense, ionized environments. This assessment could lead to a general *rule of thumb*, guiding modeling approaches for hypersonic flows for when ETC should be accounted for or not.

5.3.4 Evaluate modeling approach using updated experiments

Although past experiments can be used to assess the modeling approach to a certain degree, as was done in Chapter IV, new experiments are needed that specifically focus on ETC (e.g. low work function material, biased emissive surface) in order to truly validate the modeling approach. As shown in Chapter IV, it is imperative that the freestream and material characteristics are well-known in order to reduce the uncertainty in the simulations to clearly be able to assess how the modeling approach represents the physics of ETC. Ideally, these experiments would also lead to a better understanding of how electrons behave near the surface; most notably in the plasma sheath and boundary layer.

5.3.5 Address the challenges that could be introduced due to ETC

This thesis largely focused on the possible benefits ETC could provide to hypersonic flight. However, there are some challenges that could arise by emitting large

currents of electrons from the surface. One challenge is preventing undesirable electric arcing, or electric discharges, which could damage the hypersonic vehicle. This motivates future research to include an investigation on if ETC will induce undesired electric discharges and if so, under what conditions. Another challenge is preventing radio blackout, which refers to communication interruption during hypersonic flight due to the radio waves used for communication being affected by the ionized flow. Previous work has shown that this blackout can be mitigated by using electromagnetic manipulation of the plasma layer [117]. This could be an avenue of future work, where a similar manipulation can be used to prevent radio blackout and possibly be used to control the emitted electrons in a way where ETC is even more effective at cooling the leading edge. Nonetheless, future work should also investigate the challenges of ETC in order to truly understand if it is a viable technology.

5.3.6 Use modeling approach to investigate other hot surfaces that could benefit from ETC

This work focused on applying ETC to only leading edges of hypersonic vehicles. However, it could be extended to other thermally intense environments due to its passive operation, small footprint, and cooling benefits. There are multiple applications where ETC could be beneficial, but turbine blade cooling could be one of the most significant. Jet engine turbine blades must generally be maintained at a low enough temperature so that the material does not creep under the centrifugal force of the turbine rotation, but engine performance is improved at high-temperature operating conditions [185]. Current methods are complex and expensive to manufacture such as film cooling, which involves bleeding air from the engine's compressor and ejecting it from perforations in the precision-manufactured blade surfaces. However, if ETC was incorporated, electrons could be emitted from the blades themselves, cooling them via a transpiration effect, and then carried through an electric field to a designated

location where the electrons, and heat, could be deposited. The modeling approach in this work could be extended to investigate this concept in future work to see if it is viable.

APPENDICES

APPENDIX A

Electron Temperature Approximation

The electron temperature at the sheath edge will be based on the temperature of two different sources of electrons, emitted electrons from the surface of the vehicle and electrons from the hypersonic flowfield. The mean electron temperature the electrons can be determined from the mean energy of the electrons,

$$T_e = \frac{2E_e}{3k_B}. \tag{A.1}$$

The mean energy of the emitted electrons can be determined from taking the second moment of a biased Maxwellian velocity distribution function,

$$E_{em} = \int_{-\infty}^{\infty}\int_{-\infty}^{\infty}\int_{V_{th}}^{\infty} \frac{1}{2} m_e (V_x^2 + V_y^2 + V_z^2) \cdot \left(\frac{m_e}{2\pi k_B T}\right)^{\frac{3}{2}} \exp\left[\frac{m_e}{2k_B T}((V_x - V_{th})^2 + V_y^2 + V_z^2)\right] \cdot dV_x dV_y dV_z, \tag{A.2}$$

where the V_{th} is the threshold velocity determined by,

$$V_{th} = \sqrt{\frac{e\phi_w}{m_e}}. \tag{A.3}$$

The mean energy of the flowfield electrons is determined similarly,

$$E_{fl} = \int_{-\infty}^{\infty}\int_{-\infty}^{\infty}\int_{-\infty}^{V_{th}} \frac{1}{2} m_e (V_x^2 + V_y^2 + V_z^2) \cdot$$
$$(\frac{m_e}{2\pi k_B T})^{\frac{3}{2}} \exp\left[\frac{m_e}{2k_B T}(V_x^2 + V_y^2 + V_z^2)\right] \cdot dV_x dV_y dV_z. \tag{A.4}$$

This leads to,

$$E_{fl} = \frac{1}{2} m_e \Big(\frac{m_e}{2\pi k_B T}\Big)^{\frac{3}{2}} \cdot \left(\frac{3\pi^{\frac{3}{2}}(1 + \mathrm{erf}(\sqrt{\frac{m_e}{2k_B T}} V_{th}}{4(\frac{m_e}{2k_B T})^{\frac{5}{2}}} - \frac{\exp(-\frac{m_e}{2k_B T} V_{th}^2)\pi V_{th}}{2(\frac{m_e}{2k_B T})^2}\right) \tag{A.5}$$

$$E_{em} = \frac{1}{2} m_e \Big(\frac{m_e}{2\pi k_B T}\Big)^{\frac{3}{2}} \cdot \left(\frac{\pi(4\sqrt{\frac{m_e}{2k_B T}} V_{th} + \sqrt{\pi}(3 + \frac{m_e}{k_B T} V_{th}^2}{4(\frac{m_e}{2k_B T})^{\frac{5}{2}}}\right). \tag{A.6}$$

Using these relations and Equation 2.75, the electron temperature at the sheath edge can be approximated without solving for it explicitly.

APPENDIX B

Space-Charge Limited Emission with Supersonic Ion Velocities at Sheath Edge

Takamura et al [136] derived Equations 2.51 and 2.62 assuming that the Bohm condition is satisfied at the minimal value of sonic ion velocities at the sheath edge or presheath. This can be extended to including supersonic ion velocities at the sheath edge. Starting with a modified version of Poisson's equation for the space-charge limited condition [136],

$$\frac{\exp\left(\Phi_{vc}\right)-1}{1+AG}+\frac{FG}{1+AG}+M^2\Big(\sqrt{1-\frac{2\Phi_{vc}}{M^2}}-1\Big)=0, \tag{B.1}$$

where,

$$A=\sqrt{\frac{-\pi\Phi_{vc}}{\gamma}}\,\mathrm{erfc}\left(\sqrt{\frac{-\Phi_{vc}}{\gamma}}\right)\exp\left(\frac{-\Phi_{vc}}{\gamma}\right)$$

$$H=\frac{A-1}{\gamma}$$

$$F=-\gamma A+2\Phi_{vc}+\sqrt{-\pi\gamma\Phi_{vc}}$$

$$M = \chi\sqrt{\frac{1+AG}{1+HG}} \tag{B.2}$$

where,

$$\chi \geq 1.$$

Equation B.1 can be rearranged to give a cubic equation as a function of G, which has three real solutions and only one solution that satisfies the G is positive,

$$\beta_3 G^3 + \beta_2 G^2 + \beta_1 G + \beta_0 = 0, \tag{B.3}$$

where,

$$\beta_3 = HF^2 + 2A^3\chi^2\Phi_{vc} - 2A^2\chi^2 F$$

$$\begin{aligned}\beta_2 = \quad & F^2 + 2HF(\exp(\Phi_{vc}) - 1) + \\ & +2A^2\chi^2(3\Phi_{vc} - \exp(\Phi_{vc}) + 1) - 4AF\chi^2\end{aligned}$$

$$\begin{aligned}\beta_1 = \quad & 2F(\exp(\Phi_{vc}) - 1) + H(\exp(2\Phi_{vc}) - 2\exp(\Phi_{vc}) + 1) + \\ & +2A\chi^2(3\Phi_{vc} - 2\exp(\Phi_{vc}) + 2) - 2\chi^2 F\end{aligned}$$

$$\beta_0 = \exp(2\Phi_{vc}) - 2\exp(\Phi_{vc}) + 1 + 2\chi^2(\Phi_{vc} - \exp(\Phi_{vc}) + 1).$$

Since $\chi \approx 1$, as discussed in Section 2.5.2.2, Equation B.3 can be simplified via a curve-fit for Equation B.2 assuming the ion speed equals the ion acoustic speed for

easier implementation into a CFD code:

$$M = 1.229 + 0.02409 \log \gamma - (0.03296 + 0.01957\gamma) \log \Phi_{vc},$$

$$\beta = M^2 \left(\sqrt{1 - \frac{2\Phi_{vc}}{M^2}} - 1 \right)$$

$$G = \frac{1 - \beta - \exp(\Phi_{vc})}{A \cdot \beta + F}$$

which is valid for:

$$0.1 \leq \gamma \leq 1$$

$$-50 \leq \Phi_{vc} \leq -1$$

BIBLIOGRAPHY

BIBLIOGRAPHY

[1] H. H. Frisinger. *The Role of Mathematics and Mathematicians in the Development of Meteorology to 1800 - With a Special Emphasis on the Pressure-Height Problem*. PhD thesis, University of Michigan, Ann Arbor, MI, 1964.

[2] H. H. Frisinger. *Michigan State Highway Expenditure Policy*. PhD thesis, University of Michigan, Ann Arbor, MI, 1952.

[3] J. D. Anderson. *Introduction to Flight*. McGraw-Hill, 4th edition, 2000.

[4] E. T. Curran and S. N. B. Murthy. *Scramjet Propulsion*, volume 189 of *Progress in Astronautics and Aeronautics*. American Institute of Aeronautics and Astronautics, 2000.

[5] R. T. Voland, L. D. Huebner, and C. R. McClinton. X-43A hypersonic vehicle technology development. *Acta Astronautica*, 59:181–191, 2006.

[6] C. M. Rondeau and T. R. Jorris. X-51A scramjet demostrator program: Waverider ground and flight test. Technical report, SFTE 44th International / SETP Southwest Flight Test Symposium, 2013.

[7] Office of Chief Technologist. 2015 NASA technology roadmaps. Technical report, NASA, 2015.

[8] Office of Chief Scientist. Technology horizons: A vision for air force science and technology for 2010-30. Technical report, United States Air Force, 2010.

[9] Air Force Studies Board. A threat to america's global vigilance, reach, and power: High-speed maneuvering weapons. Technical report, The National Academies of Sciences-Engineering-Medicine, 2016.

[10] D. Sziroczak and H. Smith. A review of design issues specific to hypersonic flight vehicles. *Progress in Aerospace Sciences*, 84:1–28, 2016.

[11] J. D. Anderson. *Hypersonic and High-Temperature Gas Dynamics*. American Institute of Aeronautics and Astronautics, 2nd edition, 2006.

[12] J. J. Bertin and R. M. Cummings. Fifty years of hypersonics: where we've been, where we're going. *Progress in Aerospace Sciences*, 39:511–536, 2003.

[13] R. Wuilbercq, A. Ahmad, T. Scanlon, and R. Brown. Towards robust aerothermodynamic predictions for re-usable single-stage to orbit vehicles. *18th AIAA/3AF International Space Planes and Hypersonic Systems and Technologies Conference*, (AIAA Paper 2012-5803), 2012.

[14] S. H. Walker and F. Rodgers. Falcon hypersonic technology overview. *AIAA/CIRA 13th International Space Planes and Hypersonics Systems and Technologies*, (AIAA Paper 2005-3253), 2005.

[15] E. H. Hirschel. *Basics of Aerothermodynamics*, volume 206 of *Progress in Astronautics and Aeronautics*. American Institute of Aeronautics and Astronautics, 2005.

[16] E. H. Hirschel and C. Weiland. *Selected Aerothermodynamic Design Problems of Hypersonic Flight Vehicles*, volume 229 of *Progress in Astronautics and Aeronautics*. American Institute of Aeronautics and Astronautics, 2009.

[17] L. Lees and T. Kubota. Inviscid hypersonic flow over blunt-nosed slender bodies. *Journal of the Aeronautical Sciences*, 25:195–202, 1957.

[18] J. A. Fay and F. R. Riddell. Theory of stagnation point heat transfer in dissociated air. *Journal of the Aeronautical Sciences*, 25:73–85, 1958.

[19] W. H. Mason and Lee. J. Aerodynamically blunt and sharp bodies. *Journal of Spacecraft and Rockets*, 31(3):378–382, 1994.

[20] W. F. N. Santos. Leading-edge bluntness effects on aerodynamic heating and drag of power law body in low-density hypersonic flow. *Journal of the Brazilian Society of Mechanical Sciences*, 27(3), 2005.

[21] J. J. Bertin. *Hypersonic Aerothermodynamics*. American Institute of Aeronautics and Astronautics, 1994.

[22] L. A. Uribarri and E. H. Allen. Electron transpiration cooling for hot aerospace surfaces. *20th AIAA International Space Planes and Hypersonic Systems and Technologies Conference*, 2015.

[23] E. H. Allen and L. A. Uribarri. Cooling a target using electrons. US Patent App. 14/731,688, 2015.

[24] F. Lu and D. Marren, editors. *Advanced Hypersonic Test Facilities*, volume 198 of *Progress in Astronautics and Aeronautics*. American Institute of Aeronautics and Astronautics, 2002.

[25] J. F. Wendt, editor. *Computational Fluid Dynamics: An Introduction*. Springer, 3 edition, 2009.

[26] E. Josyula, editor. *Hypersonic Nonequilibrium Flows: Fundamentals and Recent Advances*, volume 247 of *Progress in Astronautics and Aeronautics*. American Institute of Aeronautics and Astronautics, 2015.

[27] T. K. S. Murthy, editor. *Computational Methods in Hypersonic Aerodynamics*, volume 9 of *Fluid Mechanics and Its Applications*. Computational Mechanics Publications, 1991.

[28] G. V. Candler, P. K. Subbareddy, and J. M. Brock. Advances in computational fluid dyanmics methods for hypersonic flows. *Journal of Spacecraft and Rockets*, 52:17–28, 2014.

[29] I. D. Boyd and T. E. Schwartzentruber. *Nonequilibrium Gas Dynamics and Molecular Simulation*. Cambridge Aerospace Series. Cambridge Univesity Press, 2017.

[30] S. M. Kast. *Methods for Optimal Output Prediction in Computational Fluid Dynamics*. PhD thesis, University of Michigan, Ann Arbor, MI, 2016.

[31] P. L. Roe. Lecture. In *Von Karman Institute Lecture Series*. Von Karman Institute, 1970.

[32] J. D. Anderson. A survey of modern research in hypersonic aerodynamics. *AIAA 17th Fluid Dynamics, Plasma Dynamics, and Lasers Conference*, (AIAA Paper 1984-1578), 1984.

[33] J. J. Bertin, R. Glowinksi, and J. Periaux, editors. *Hypersonics: Defining the Hypersonic Environment*, volume 1 of *Progress in Scientific Computing*. Birkhauser, 1989.

[34] C. Park. *Nonequilibrium Hypersonic Aerothermodynamics*. John Wiley & Sons, 1990.

[35] J. D. Anderson. *Modern Compressible Flow: With Historical Perspective*. McGraw-Hill, 3rd edition, 2003.

[36] B. J. McBride and S. Gordon. Computer program for calculation of complex chemical equilibrium compositions and applications. Technical Report 1311, NASA, 1996.

[37] D. Knight. Assessment of predictive capabilities for aerodynamic heating in hypersonic assessment of predictive capabilities for aerodynamic heating in hypersonic flow. *Progress in Aerospace Sciences*, 2017.

[38] J. J. Bertin, R. Glowinksi, and J. Periaux, editors. *Hypersonics: Computation and Measurement of Hypersonic Flow*. Progress in Scientific Computing. Birkhauser, 1989.

[39] T. E. Schwartzentruber and I. D. Boyd. Progress and future prospects for particle-based simulation of hypersonic flow. *Progress in Aerospace Sciences*, 72:66–79, 2015.

[40] A. M. Verfhoff. *Numerical Simulation of Transitional, Hypersonic Flows using a Hybrid Particle-Continuum Method*. PhD thesis, University of Michigan, Ann Arbor, MI, 2015.

[41] P. J. Waltrup. Upper bounds on the flight speed of hydrocarbon-fueled scramjet-powered vehicles. *Journal of Propulsion and Power*, 17(6):1199–1204, 2001.

[42] D. E. Glass. Ceramic matrix composite (CMC) thermal protection systems (TPS) and hot structures for hypersonic vehicles. *15th AIAA International Spaces Planes and Hypersonic Systems and Technologies Conference*, (AIAA Paper 2008-2682), 2008.

[43] E. Thorton, editor. *Aerospace Thermal Structures and Materials for a New Era*, volume 168 of *Progress in Astronautics and Aeronautics*. American Institute of Aeronautics and Astronautics, 2000.

[44] H. G. McComb, H. N. Murrow, and M. F. Card. Structures and materials technology for hypersonic aerospacecraft. Technical Report 102583, NASA, 1990.

[45] A. K. Hyder, R. L. Wiley, G. Halpert, D. J. Flood, and S. Sabripour. *Spacecraft Power Technologies*, volume 1. Imperial College Press, 2000.

[46] D. E. Glass. Physical challenges and limitations confronting the use of UHTCs on hypersonic vehicles. *17th AIAA International Space Planes and Hypersonic Systems and Technologies Conference*, (AIAA Paper 2011-2304), 2011.

[47] G. Duffa. *Ablative Thermal Protection Systems Modeling*. American Institute of Aeronautics and Astronautics, 2013.

[48] H. K. Tran, C. E. Johnson, D. J. Rasky, F. C. L. Hui, M. Hsu, and Y. K. Chen. Phenolic impregnated carbon ablators (PICA) for discovery class missions. *31st AIAA Thermophysics Conference*, (AIAA Paper 1996-1911), 1996.

[49] J. Lachaud, T. E. Magin, I. Cozmuta, and N. N. Mansour. A short review of ablative-material response models and simulation tools. *7th Aerothermodynamics Symposium*, 2011.

[50] D. Tavella and L. Roberts. Transpiration cooling in hypersonic flight. Technical report, NASA, 1989.

[51] C. Herring and M. H. Nichols. Thermionic emission. *Reviews of Modern Physics*, 21(2):185–269, 1949.

[52] E. L. Murphy and R. H. Good. Thermionic emission, field emission, and the transition region. *Physical Review*, 102(6):1464–1473, 1956.

[53] T. J. Jones. *Thermionic Emission*. Methuen & Co., 1936.

[54] D. M. Rowe, editor. *Thermoelectrics Handbook*. Taylor & Francis, 2006.

[55] S. Dushman. Thermionic emission. *Reviews of Modern Physics*, 2(4), 1930.

[56] G. W. Sutton, editor. *Direct Energy Conversion*, volume 3. McGraw-Hill, 1966.

[57] G. N. Hatsopoulos and E. P. Gyftopoulos. *Thermionic Energy Conversion: Processes and Devices*, volume 1. MIT Press, 1973.

[58] G. N. Hatsopoulos and E. P. Gyftopoulos. *Thermionic Energy Conversion: Theory, Technology, and Application*, volume 2. MIT Press, 1979.

[59] L. K. Hansen, editor. *Thermionic Converters and Low-Temperature Plasma*. U.S. Department of Energy, 1978.

[60] J. J. Thomson. XL. cathode rays. *Philosophical Magazine*, 44(269):293–316, 1897.

[61] E. A. Davis and I. J. Falconer. *J. J. Thomson and the Discovery of the Electron*. Taylor & Francis, 1997.

[62] F. Guthrie. On a new relation between heat and electricity. *Proceedings of the Royal Society of London*, 21, 1873.

[63] M. Josephson. *Edison: A Biography*. John Wiley & Sons, 1992.

[64] T. A. Edison. Electrical indicator. U.S. Patent No. 307,031, 1884.

[65] W. H. Preece. On a peculiar behaviour of glow lamps when raised to high incandescence. *Proceedings of the Royal Society of London*, 38:219–230, 1884.

[66] O. W. Richardson. On the negative radiation from hot platinum. *Philsophical of the Cambridge Philsophical Society*, 11:286–295, 1901.

[67] O. W. Richardson. The electrical conductivity imparted to a vacuum by hot conductors. *Philosophical Transactions of the Royal Society of London*, 201:497–549, 1903.

[68] O. W. Richardson. *Emission of Electricty from Hot Bodies*. Longmans, Green, and Co., 1921.

[69] K. J. Touryan. A hypersonic plasma power generator. *AIAA Journal*, 3(4):652–659, 1965.

[70] A. R. LeBlanc and W. W. Grannemann. Thermionic generator for re-entry vehicles. *Proceedings of the IEEE*, 52(11):1302–1310, 1964.

[71] K. J. Touryan. The hypersonic plasma converter: II. Technical Report SC-RR-4960, Sandia Laboratories, 1964.

[72] K. M. Hanquist, H. Alkandry, and I. D. Boyd. Evaluation of computational modeling of electron transpiration cooling at high enthalpies. *Journal of Thermophysics and Heat Transfer*, 2016.

[73] J. J. Martin. *Atmospheric Re-entry, An Introduction to Its Science and Engineering*. Prentice-Hall, 1966.

[74] P. D. Thomas. Transparency assumption in hypsonic radiative gas dynamics. *AIAA Journal*, 3(8):1401–1407, 1965.

[75] C. R. Crowell. The richardson constant for thermionic emission in schottky barrier diodes. *Solid-State Electronics*, 8(4):395–399, 1965.

[76] B. Wolf, editor. *Handbook of Ion Sources*. CRC Press, 1995.

[77] C. J. Smithells. *Metals Reference Book*. Plenum Press, 4th edition, 1967.

[78] P. T. Harsha, L. C. Keel, and A. Castrogiovanni. X-43A vehicle design and manufacture. *13th International Space Planes and Hypersonics Systems and Technologies Conference*, (AIAA Paper 2005-3334), 2005.

[79] W. G. Vincenti and C. H. Kruger. *Introduction to Physical Gas Dynamics*. Krieger, 2002.

[80] W. Sutherland. The viscosity of gases and molecular forces. *Philosophical Magazine*, 5:507–531, 1893.

[81] M. Picone, A. E. Hedin, and D. Drob. NRLMSISE-00 model 2001. *US Naval Research Laboratory*, 2008.

[82] A. J. Lofthouse, L. C. Scalabrin, and I. D. Boyd. Velocity slip and temperature jump in hypersonic aerothermodynamics. *Journal of Thermophysics and Heat Transfer*, 22(1):38–49, 2008.

[83] G. A. Bird. Breakdown of translational and rotational equilibrium in gaseous expansions. *AIAA Journal*, 8(11), 1970.

[84] V. DiCristina. Three-dimensional laminar boundary-layer transition on a sharp 8 deg. cone at mach 10. *AIAA Journal*, 8(5):852–856, 1970.

[85] C. J. Roy and F. G. Blottner. Review and assessment of turbulence models for hypersonic flows. *Progress in Aerospace Sciences*, 42(7-8):469–530, 2006.

[86] L. C. Scalabrin. *Numerical Simulation of Weakly Ionized Hypersonic Flow over Reentry Capsules*. PhD thesis, University of Michigan, Ann Arbor, MI, 2007.

[87] A. Martin, L. C. Scalabrin, and I. D. Boyd. High performance modeling of atmospheric re-entry vehicles. *Journal of Physics: Conference Series*, 341, 2011.

[88] J. H. Lee. Basic governing equations for the flight regimes of aeroassisted orbital transfer vehicles. *AIAA 19th Thermophysics Conference*, (AIAA Paper 1984-1729), 1984.

[89] F. M. White. *Viscous Fluid Flow*. McGraw-Hill, 2006.

[90] H. Alkandry. *Aerodynamic Interactions of Propulsive Deceleration and Reaction Control System Jets on Mars-Entry Aeroshells*. PhD thesis, University of Michigan, Ann Arbor, MI, 2012.

[91] K. Sutton and P. A. Gnoffo. Multi-component diffusion with applications to computational aerothermodynamics. *7th AIAA/ASME Joint Thermophysics and Heat Transfer Conference*, (AIAA Paper 1998-2575), 1998.

[92] C. R. Wilke. A viscosity equation for gas mixtures. *Journal of Chemical Physics*, 18(4):517–519, 1950.

[93] F. G. Blottner, M. Johnson, and M. Ellis. Chemically reacting viscous flow program for multi-component gas mixtures. Technical Report SC-RR-70-754, Sandia Laboratories, 1971.

[94] G. E. Palmer and M. J. Wright. Comparison of methods to compute high-temperature gas viscosity. *Journal of Thermophysics and Heat Transfer*, 17(2):232–239, 2003.

[95] R. N. Gupta, J. M. Yos, R. A. Thompson, and K. P. Lee. A review of reaction rates and thermodynamic and transport properties for an 11-species air model for chemical and thermal nonequilibrium calculations to 30000 k. Technical Report NASA-RP-1232, NASA, 1990.

[96] M. J. Wright, H. H. Hwang, and D. W. Schwenke. Recommended collision integrals for transport property computations part 2: Mars and Venus entries. *AIAA Journal*, 45(1):281–288, 2007.

[97] R. W. MacCormack and G. V. Candler. The solution of the navier-stokes equations using gauss-seidel line relaxation. *Computers & Fluids*, 17(1):135–150, 1989.

[98] N. J. Bisek. *Numerical Study of Plasma-Assisted Aerodynamic Control for Hypersonic Vehicles*. PhD thesis, University of Michigan, Ann Arbor, MI, 2010.

[99] T. D. Holman. *Numerical Investigation of the Effects of Continuum Breakdown on Hypersonic Vehicle Surface Properties*. PhD thesis, University of Michigan, Ann Arbor, MI, 2010.

[100] T. R. Deschenes. *Extension of a Modular Particle-Continuum Method for Nonequilibrium, Hypersonic Flows*. PhD thesis, University of Michigan, Ann Arbor, MI, 2010.

[101] C. D. Scott. *Advances in Hypersonics: Modeling Hypersonic Flows*, volume 2, chapter Wall Catalytic Recombination and Boundary Conditions in Nonequilibrium Hypersonic Flows - With Applications, pages 175–250. Birkhauser, 1992.

[102] M. A. Lieberman and A. J. Lichtenberg. *Principles of Plasma Discharges and Materials Processing*. John Wiley & Sons, 1994.

[103] A. G. Cambel. *Plasma Physics and Magnetofluid-Mechanics*. McGraw-Hill, 1963.

[104] S. Chapman and T. G. Cowling. *The Mathematical Theory of Non-Uniform Gases*. Cambridge Univesity Press, 1970.

[105] Y. Weng and M. J. Kushner. Method for including electron-electron collisions in monte carlo simulations of electron swarms in partially ionized gases. *Physical Review A*, 42(10):6192–6200, 1990.

[106] M. S. Benilov and A. Marotta. A model of the cathode region of atmospheric pressure arcs. *Journal of Physics D: Applied Physics*, 28(9):1869–1882, 1995.

[107] N. J. Bisek, I. D. Boyd, and J. Poggie. Three dimensional simulations of hypersonic mhd flow control. *40th AIAA Plasmadynamics and Lasers Conference*, (AIAA Paper 2009-3731), 2009.

[108] M. Kim and I. D. Boyd. Effectiveness of magnetohyrdodynamics system for mars entry. *Journal of Spacecraft and Rockets*, 49(6):1141–1149, 2012.

[109] R. W. MacCormack. Solution of the equations of magneto-fluid dynamics with chemical reaction. *41st Plasmadynamics and Lasers Conference*, (AIAA 2010-4636), 2010.

[110] H. Alkandry, K. M. Hanquist, and I. D. Boyd. Conceptual analysis of electron transpiration cooling for leading edges of hypersonic vehicles. *11th AIAA/ASME Joint Thermophysics and Heat Transfer Conference*, (AIAA Paper 2014-2674), 2014.

[111] Baeva. M., R. Kozakov, S. Gorchakov, and D. Uhrlandt. Two-temperature chemically non-equilibrium modelling of transferred arcs. *Plasma Sources Science and Technology*, 21(5), 2012.

[112] A. Fridman and L. A. Kennedy. *Plasma Physics and Engineering*. Taylor & Francis, 2004.

[113] G. A. Eiceman and Z. Zarpas. *Ion Mobility Spectrometry*. Taylor & Francis, 2 edition, 2005.

[114] E. W. McDaniel and E. A. Mason. *The Mobility and Diffusion of Ions in Gases*. John Wiley & Sons, 1973.

[115] Z. Karpas, Z. Berant, and O. Shahal. Effect of temperature on the mobility of ions. *Journal of American Chemical Society*, 111(16):6015–6018, 1989.

[116] E. W. McDaniel. *Collision Phenomena in Ionized Gases*. John Wiley & Sons, 1964.

[117] M. K. Kim. *Electromagnetic Manipulation of Plasma Layer for Re-Entry Blackout Mitigation*. PhD thesis, University of Michigan, Ann Arbor, MI, 2009.

[118] V. A. Bityurin, J. T. Lineberry, V. Potebnia, V. I. Alferov, A. L. Kuranov, and E. G. Sheikin. Assessment of hypersonic mhd concepts. *28th Plasmadynamics and Lasers Conference*, (AIAA Paper 1997-2393), 1997.

[119] W. B. Bush. Magnetohyrdodynamic-hypersonic flow past a blunt body. *Journal of the Aerospace Sciences*, 25(11):685–690, 1958.

[120] H. M. Damevin, K. A. Hoffmann, and J. F. Dietiker. Numerical simulation of hypersonic mhd applications. *30th AIAA Plasmadynamics and Lasers Conference*, (1999-3611), 1999.

[121] Y. Nagata, K. Yamada, and T. Abe. Hypersonic double-cone flow with applied magnetic field. *Journal of Spacecraft and Rockets*, 50(5):981–991, 2013.

[122] J. C. Maxwell. *A Treatise on Electricity and Magnetisim*. Oxford, 1873.

[123] J. A. Stratton. *Electronmagetic Theory*. McGraw-Hill, 1941.

[124] Y. P. Raizer. *Gas Discharge Physics*. Springer-Verlag, 1991.

[125] Y. Itakawa. Cross sections for electron collisions with nitrogen molecules. *Journal of Physical and Chemical Reference Data*, 35(1), 2006.

[126] M. J. Wright, D. Bose, G. E. Palmer, and E. Levin. Recommended collision integrals for transport property computations part 1: Air species. *AIAA Journal*, 43(12):2558–2564, 2005.

[127] T. E. Sheridan and J. Goree. Collisional plasma sheath model. *Physics of Fluids B: Plasma Physics*, 3:2796–2804, 1991.

[128] K. Hara. *Development of Grid-Based Direct Kinetic Method and Hybrid Kinetic Continuum Modeling of Hall Thruster Discharge Plasma*. PhD thesis, University of Michigan, Ann Arbor, MI, 2015.

[129] T. E. Sheridan and M. J. Goeckner. Collisional sheath dynamics. *Journal of Applied Physics*, 77(10):4967–4972, 1995.

[130] L. Pekker. A sheath collision model with thermionic electron emission and the schottky correction factor for work function of wall material. *Plasma Chemistry and Plasma Processing*, 2016.

[131] I. Langmuir and K. T. Compton. Electrical discharges in gases: Part II. fundamental phenomena in electrical discharges. *Reviews of Modern Physics*, 3(2):191–257, 1931.

[132] J. A. Becker. Thermionic electron emission and adsoption. *Reviews of Modern Physics*, 7(2):95–128, 1935.

[133] J. P. Sheehan and N. Hershkowitz. Emissive probes. *Plasma Sources Science and Technology*, 20(6):1–22, 2011.

[134] G. D. Hobbs and J. A. Wesson. Heat flow through a langmuir sheath in the presence of electron emission. *Plasma Physics*, 7(8):85–87, 1967.

[135] M. Y. Ye and S. Takamura. Effect of space-charge limited emission on measurements of plasma potential using emissive probes. *Physics of Plasmas*, 7(8):3457–3463, 2000.

[136] S. Takamura, N. Ohno, M. Y. Ye, and T. Kuwabara. Space-charge limited current from plasma-facing material surface. *Contributions to Plasma Physics*, 44(1-3):126–137, 2004.

[137] D. Bohm. *The Characteristics of Electrical Discharges in Magnetic Fields*, chapter Minimum ionic kinetic energy for a stable sheath. McGraw-Hill, 1949.

[138] V. A. Godyak. Modified bohm criterion for a collisional plasma. *Physical Review A*, 89(2):80–81, 1982.

[139] V. A. Godyak and N. Sternberg. Smooth plasma-sheath transition in a hydrodynamic model. *IEEE Transactions on Plasma Science*, 18(1):159–168, 1990.

[140] K. M. Hanquist, K. Hara, and I. D. Boyd. Detailed modeling of electron emission for transpiration cooling of hypersonic vehicles. *Journal of Applied Physics*, 121(5), 2017.

[141] L. Pekker and N. Hussary. Effect of boundary conditions on the heat flux to the wall in two-temperature modeling of 'thermal' plasmas. *Journal of Physics D: Applied Physics*, 47:1–8, 2014.

[142] L. Pekker and N. Hussary. Boundary conditions at the walls with thermionic electron emission in two temperature modeling of "thermal" plasmas. *Physics of Plasmas*, 22, 2015.

[143] M. Mitchner and C. H. Kruger. *Partially Ionized Gas*. John Wiley & Sons, 1973.

[144] E. Farbar, I. D. Boyd, and A. Martin. Numerical prediction of hypersonic flowfields including effects of electron translational nonequilibrium. *Journal of Thermophysics and Heat Transfer*, 27(4):593–606, 2013.

[145] L. Oksuz and N. Hershkowitz. First experimental measurements of the plasma potential throughout the presheath and sheath at a boundary in a weakly collisional plasma. *Physical Review Letters*, 89(14), 2002.

[146] J. E. Wiebenga. *High-Fidelity Material Response Modeling as Part of an Aerothermoelastic Framework for Hypersonic Flows*. PhD thesis, University of Michigan, Ann Arbor, MI, 2014.

[147] J. E. Wiebenga and I. D. Boyd. Computation of multi-dimensional material response coupled to hypersonic flow. *43rd AIAA Thermophysics Conference*, (AIAA Paper 2012-2873), 2012.

[148] A. Martin and I. D. Boyd. Strongly coupled computation of material response and nonequilibrium flow for hypersonic ablation. *Journal of Spacecraft and Rockets*, 52(1):89–104, 2015.

[149] N. J. Bisek, I. D. Boyd, and J. Poggie. Numerical study of energy deposition requirements for aerodynamic control of hypersonic vehicles. *46th AIAA Aerospace Sciences Meeting and Exhibit*, (AIAA 2008-1109), 2008.

[150] S. W. Kim, T. Shimoyama, and H. Hosono. Solvated electrons in high-temperature melts and glasses of the room-temperature stable electride $[Ca_{24}Al_{28}O_{64}]^{4+}$ 4 e^-. *Science*, 333(6038):71–74, 2011.

[151] L. P. Rand and J. D. Williams. A calcium aluminate electride hollow cathode. *IEEE Transactions on Plasma Science*, 43(1):190–194, 2015.

[152] Y. Toda, S. W. Kim, K. Hayashi, M. Hirano, T. Kamiya, H. Hosono, T. Haraguchi, and H. Yasuda. Intense thermal field electron emission from room-temperature stable electride. *Applied Physics Letters*, 87(25), 2005.

[153] L. P. Rand. *A Calcium Aluminate Electride Hollow Cathode*. PhD thesis, Colorado State University, Fort Collins, CO, 2014.

[154] T. Yoshizumi and K. Hayashi. Thermionic electron emission from a mayenite electride-metallic titanium composite cathode. *Applied Physics Express*, 6(1), 2013.

[155] A. Sindona, M. Pisarra, P. Riccardi, and G. Falcone. Cluster and periodic density functional study of auger electron emission from conducting carbon nanotubes. *Nanoscience and Nanotechnology Letters*, 4(11):1050, 1055 2012.

[156] J. W. Zimmermann, G. E. Hilmas, and W. G. Fahrenholtz. Thermal shock resistance of ZrB_2 and ZrB_2-30% SiC. *Materials Chemistry and Physics*, 112:140–145, 2008.

[157] M. M. Opeka, I. G. Talmy, E. J. Wuchina, J. A. Zaykoski, and S. J. Causey. Mechanical, thermal, and oxidation properties of refractory hafnium and zirconium compounds. *Journal of the European Ceramic Society*, 19(13-14):2405–2414, 1999.

[158] M. Patel, V. V. B. Prasad, and V. Jayaram. Heat conduction mechanisms in hot pressed ZrB_2 and ZrB_2-SiC composites. *Journal of the European Ceramic Society*, 33:1615–1624, 2013.

[159] R. Stadelmann. *ZrB2-SiC Based Ultra High Temperature Ceramic Composites: Mechanical Performance and Measurement and Design of Thermal Residual Stresses for Hypersonic Vehicle Applications*. PhD thesis, University of Central Florida, Orlando, FL, 2015.

[160] S. W. Kim, Y. Toda, K. Hayashi, M. Hirano, and H. Hosono. Synthesis of a room temperature stable 12cao-7al_2o_3 electride from the melt and its application as an electron field emitter. *Chemistry of Materials*, 18(7):1938–1944, 2006.

[161] F. P. Incropera, D. P. DeWitt, T. L. Bergman, and A. S. Lavine. *Fundamentals of Heat and Mass Transfer*. John Wiley & Sons, 6th edition, 2007.

[162] R. G. Munro. Material properties of titanium diboride. *Journal of Research of the National Institute of Standards and Technology*, 105(5):709–720, 2000.

[163] U. C. Paek and Schroeder. A new design of zirconia induction furnace for production of high-strength fiber. *Journal of Lightwave Technology*, 4(8):1061–1066, 1986.

[164] J. D. Whitfield and B. J. Griffith. Hypersonic viscous drag effects on blunt slender cones. *AIAA Journal*, 2(10):1714–1722, 1964.

[165] Y. K. Chen and F. S. Milos. Ablation and thermal response program for spacecraft heatshield analysis. *Journal of Spacecraft and Rockets*, 36(3):475–483, 1999.

[166] E. N. Carabateas, S. D. Pezaris, and G. N. Hatsopoulos. Interpretation of experimental characteristics of cesium thermionic converters. *Journal of Applied Physics*, 32(3):352–358, 1961.

[167] D. W. Kuntz, B. Hassan, and D. L. Potter. Predictions of ablating hypersonic vehicles using an iterative coupled fluid/thermal approach. *Journal of Thermophysics and Heat Transfer*, 15(2):129–139, 2001.

[168] W. M. Haynes. *CRC Handbook of Chemistry and Physics*. CRC Press, 94th edition, 2013.

[169] K. S. Krishnan and S. C. Jain. Thermionic constants of graphite. *Nature*, 169(4304):702–703, 1952.

[170] A. L. Reiman. Thermionic emission from carbon. *Proceedings of the Physical Society*, 50(4):496–500, 1938.

[171] Y. S. Touloukian. *Thermophysical Properties of Matter, the TPRC Data Series: A Comprehensive Compilation of Data*, volume 7-8. IFI-Plenum, 1970.

[172] M. H. Nichols. The thermionic constants of tungsten as a function of crystallographic direction. *Physical Review Letters*, 57(4):297–306, 1940.

[173] C. E. Moore. Atomic energy levels as derived from the analysis of optical spectra, volume 1. *Circular of the Bureau of Standards*, 1(467):211–215, 1949.

[174] M. I. Boulos, P. Fauchais, and E. Pfender. *Thermal Plasma: Fundamentals and Applications*, volume 1. Springer Science and Business Media, 1994.

[175] C. Park and S. H. Lee. Validation of multi-temperature nozzle flow code. *Journal of Thermophysics and Heat Transfer*, 9(1):9–16, 1995.

[176] C. George, G. V. Candler, and E. Pfender. An implicit algorithm to simulate reaction chemistry in a plasma. *Journal of Physics D: Applied Physics*, 31(18):2269–2280, 1998.

[177] R. B. Greendyke, P. A. Gnoffo, and R. W. Lawrence. Calculated electron number density profiles for the aeroassist flight experiment. *Journal of Spacecraft and Rockets*, 29(5):621–626, 1992.

[178] M. Furudate, I. S. Jeung, and S. Matsuyama. Nonequilibrium calculation of flowfield over galileo probe. *44th AIAA Aerospace Sciences Meeting and Exhibit*, (AIAA Paper 2006-383), 2006.

[179] M. J. Wright and E. Levin. Collision integrals for ion-neutral interactions of air and argon. *Journal of Thermophysics and Heat Transfer*, 19(1):127–128, 2005.

[180] J. R. Howell, R. Siegal, and M. P. Menguc. *Thermal Radiation Heat Transfer*. CRC Press, 5th edition, 2011.

[181] K. M. Hanquist and I. D. Boyd. Comparisons of computations with experiments for electron transpiration cooling at high enthalpies. *45th AIAA Thermophysics Confernce*, (AIAA Paper 2015-2351), 2015.

[182] K. M. Hanquist and I. D. Boyd. Limits for thermionic emission from leading edges of hypersonic vehicles. *54th AIAA Aerospace Sciences Meeting*, (AIAA Paper 2016-0507), 2016.

[183] K. M. Hanquist, K. Hara, and I. D. Boyd. Modeling of electron transpiration cooling for hypersonic vehicles. *46th AIAA Thermophysics Conference*, (AIAA Paper 2016-4433), 2016.

[184] K. M. Hanquist and I. D. Boyd. Computational analysis of electron transpiration cooling for hypersonic vehicles. *55th AIAA Aerospace Sciences Meeting*, (AIAA Paper 2017-0900), 2017.

[185] J. H. Perepezko. The hotter the engine, the better. *Science*, 326(5956):1068–1069, 2009.